UNIVERSITY of CALIFORNIA
Santa Barbara

Advanced optical characterization of complex oxide thin films grown by molecular beam epitaxy

A dissertation submitted in partial satisfaction of the
requirements for the degree of

Doctor of Philosophy

in

Materials

by

Ryan Shigeo Russell

Committee in charge:

Professor John Harter, Chair

Professor Bolin Liao

Professor Susanne Stemmer

Professor Stephen Wilson

September 2023

The dissertation of Ryan Shigeo Russell is approved:

Professor Bolin Liao

Professor Susanne Stemmer

Professor Stephen Wilson

Professor John Harter, Chair

September 2023

For Granddad.

ばばへ捧ぐ。

Acknowledgements

First and foremost, I would like to extend my most sincere gratitude to my advisor, John Harter, for his unwavering support and considerable patience in guiding me toward a PhD. Through unexpected – and at times unprecedented – circumstances, John mentored me with a kindness and capability that one could only hope for in their PhD advisor. I am also extremely grateful to my committee members, Professors Bolin Liao, Susanne Stemmer, and Stephen Wilson, for their exceptional guidance on technical matters and for their encouragement and generosity with their time.

I am indebted to my collaborators, without whom none of this work would have been possible. Many thanks to Nicholas Combs and Hanbyeol Jeong for their persistence in growing excellent films of $SrTiO_3$. A special thanks to both Kaveh Ahadi and Salva Salmani-Rezaie, not only for their pivotal roles in the $SrTiO_3$ project, but also for serving as mentors to me throughout my career as a graduate student. I am also grateful for my collaborators from Cornell Univeristy; thank you to Hari Nair for providing the Sr_2RuO_4 films that constitute a major topic of this thesis, and thank you to Professors Kyle Shen and Darrell Schlom for their scientific insight and commitment to a prolonged project. Many thanks to Anita Verma and Professor Andrej Singer for spearheading the work on the Ca_2RuO_4 project and for many fruitful discussions.

My experience at UCSB would not have been the same were it not for my wonderful labmates. Alex, Art, Jack, Nick, and Ruben, thank you all for your support, your commiseration, and your friendship. I will very much miss sitting in an office with you all, not to mention the mountain biking, rock climbing, and nights out on the town. I am lucky to have met such excellent and caring people.

Thank you to the wonderful friends I've made since I arrived at UCSB – Santa Barbara would not be the same without you. Becca, Colton, Keith, and Vince, I am eternally stoked on the time we spent climbing and adventuring together. Dan, Emily, Justin, Kevin, and Zach, thank you for adopting me into your friend group in the second half of my PhD; I never expected to watch so much of The Bachelor. Andy, thanks for making the most of a surreal lockdown experience in San Clemente and for numerous quality spots. To Angela, Avi, Dale, and Kierstin: thank you for your continued friendship even as life scatters us across the far corners of the country. I still reminisce fondly about afternoons at Krishna lunch.

I would be remiss not to mention the enormous role that my family has played throughout my PhD and my whole life leading up to it. Thank you Granddad, for laying the foundation upon which I have built everything that I've accomplished. Thank you Baba, for supporting me in every pursuit I ever dreamed of, from piano lessons to a PhD, despite the ocean between us. Thank you Mom, for the countless hours you have spent supporting me, transporting me, and generally keeping me alive and well. Words do not exist to express how much I appreciate you. Thank you Dad, for your guidance, your belief in me, and your dedicated insistence on the importance of education. Thank you Kyle, for your sense of humor, and for the daily COVID phone calls that kept us both sane. Thank you Sasha, for always being a bright spot in my day.

And, of course, thank you to my incomparable partner, Isabel, for everything. You're the best part of it all.

Curriculum Vitæ

Ryan Shigeo Russell

Education

2023 Ph.D., Materials, University of California, Santa Barbara

2018 B.S., Materials Science and Engineering, University of Florida, Gainesville, Florida

Publications

"Electronic nematic order in the normal state of strontium ruthenate" Ryan S. Russell, Hari P. Nair, Kyle M. Shen, Darrell G. Schlom, and John W. Harter. *Physical Review B* 8 108 (2023): L081105.

"Picosecond volume expansion drives a later-time insulator-metal transition in a nano-textured Mott Insulator" Anita Verma, Denis Golež, Oleg Yu. Gorobtsov, Kelson Kaj, Ryan Russell *et al. Submitted.*

"Ferroelectricity and superconductivity in strained $Eu_xSr_{1-x}TiO_3$ films" Nicholas G. Combs, Hanbyeol Jeong, Ryan Russell, Linus Kautzsch, Tyler N. Pardue, Thomas E Mates, Stephen D Wilson, John W Harter, and Susanne Stemmer. *Physical Review B* 107 (2023): 094504.

"Similarity in the critical thicknesses for superconductivity and ferroelectricity in strained $SrTiO_3$ films" Hanbyeol Jeong, Ryan Russell, Nicholas G. Combs, Tyler N. Pardue, John W. Harter, and Susanne Stemmer. *Applied Physics Letters* 121 (2022): 012601.

"Role of locally polar regions in the superconductivity of $SrTiO_3$" Salva Salmani-Rezaie, Hanbyeol Jeong, Ryan Russell, John W. Harter, and Susanne Stemmer. *Physical Review Materials* 5 (2021): 104801.

"Superconductivity in magnetically doped $SrTiO_3$" Salva Salmani-Rezaie, Luca Galletti, Timo Schumann, Ryan Russell, Hanbyeol Jeong, Yuntian Li, John W. Harter, and Susanne Stemmer. *Applied Physics Letters* 118 (2021): 202602.

"Ferroelectric enhancement of superconductivity in compressively strained $SrTiO_3$ films" Ryan Russell, Noah Ratcliff, Kaveh Ahadi, Lianyang Dong, Susanne Stemmer, and John W. Harter. *Physical Review Materials* 3 (2019): 091401.

Abstract

Advanced optical characterization of complex oxide thin films grown by molecular beam epitaxy

by

Ryan Shigeo Russell

Light-matter interactions are one of the primary methods by which scientists study structure-property relationships in materials. Optical characterization – a set of techniques that use wavelengths of light visible to the human eye – has proven to be a powerful class of methods to reveal the structure and symmetry of materials. Here, we use second harmonic generation (SHG) and time-resolved optical pump probe spectroscopy to study phase transitions in complex oxide thin films with perovskite-like structure.

A primary focus of this work is the study of electronic symmetry breaking in thin films of epitaxially-strained Sr_2RuO_4. Once thought to be a candidate solid-state analogue of the A phase of superfluid helium-3, Sr_2RuO_4 has been the subject of renewed research interest after the hypothesis of its spin-triplet superconductivity was struck down. Ostensibly a textbook example of a Fermi liquid, Sr_2RuO_4 has one of the most well studied normal states of any material, and its crystal growth has been refined to achieve mean free paths of over a micrometer. With an extraordinarily well-studied fermiology, Sr_2RuO_4 is well poised as a testing ground for theories of correlated electrons. Here, we study

epitaxially strained Sr_2RuO_4 with time-resolved optical pump probe spectroscopy and reveal the presence of an electronic nematic phase in the normal state. The temperature dependence of both a static optical dichroism and a transient reflectivity anisotropy are modeled well by an Ising-like order parameter. A microscopic explanation of the electronic symmetry breaking is offered through the Emery model, which explains nematic ordering through a redistribution of electron density. Our evidence of electronic nematicity in the normal state of Sr_2RuO_4 may have important consequences for a successful theory of the as-yet unexplained superconducting phase.

Separately, a discussion is presented of strained, doped films of $SrTiO_3$ grown by molecular beam epitaxy. As the first known semiconducting (and unconventional) superconductor, bulk $SrTiO_3$ is known to be an incipient ferroelectric that avoids a polar transition at low temperatures. SHG is used to reveal the presence of a polar phase in strained, doped films of $SrTiO_3$, and moreover links the ferroelectric phase with enhanced superconductivity exhibited in this system. Films are doped across various carrier densities to find the polar phase boundary, which is shown to coincide with aborted superconductivity, clarifying the role of polar fluctuations as a pairing mechanism. The effect of magnetic dopants is also studied, where Eu is used to introduce localized, unpaired f-electrons. It is found that both the polar and superconducting phases are insensitive to magnetic dopants up to a few percent and are surprisingly robust to even higher levels of magnetic doping. The paradigm of local polar order is also discussed in the context of superconducting pairing. Although enhanced superconductivity in $SrTiO_3$ is intricately

linked with broken inversion symmetry, it appears that a global polar phase is not required to mediate electron pairing; rather, polar nanodomains are sufficient to support the superconducting phase.

Finally, a brief chapter is included that presents preliminary measurements of Ca_2RuO_4 thin films. Optical pump probe measurements support the discovery of a photoinduced picosecond volume expansion which results in a later-time insulator-metal transition. The effects of temperature and optical pump fluence on the transient response are also explored; a nontrivial dependence on pump fluence is discovered at low temperature, as well as coherent oscillations, which motivate future investigation of the system.

Contents

Chapter 1

Introduction

1.1 Studying quantum materials with light

Light-matter interactions provide a wealth of information for scientists who wish to understand the symmetries and structure of materials. Indeed, optical characterization – the measurement of quantities such as reflectivity, transmission, and refraction – allows one to deduce the dielectric function and optical conductivity of a material, which are directly related to quantities such as carrier densities, relaxation times, and electronic band gaps. Ultrafast optical methods open further avenues of study, whereby one can readily measure nonlinear optical effects which occur under very high electric field strengths, as well as phenomena which occur at ultrafast timescales down to the femtosecond regime. These techniques have been used with great success in the study of so-called quantum materials, where complex interactions between degrees of freedom such as orbital, charge, spin, and lattice result in the manifestation of quantum effects at length and energy

scales much larger than those where the effects are typically encountered [1]. Ultrafast techniques have been used to disentangle the effects of coupled degrees of freedom, reveal hidden order, and induce long-lived nonequilibrium states via nonthermal pathways which have no equilibrium analogue. [2]. The continued study of such systems using ultrafast light sources offers an increased understanding of the fundamental character and behavior of electrons and other degrees of freedom in condensed matter systems, which promises to unlock new functionalities for future technologies [3, 4].

1.1.1 Fermi liquid theory

To have any hope of studying a large ($N \sim 10^{23}$) interacting many-body system, one needs to make drastic simplifications. In many materials, the independent electron approximation, alongside Bloch's theorem, is sufficient to arrive at a successful description of electrons in a periodic potential. However, if the electrons are found to have significant interactions, the independent electron approximation is no longer valid. Thankfully, we have recourse in Fermi liquid theory, a natural extension of the theory of the non-interacting Fermi gas. To construct the Fermi liquid, one starts with the usual picture of free fermions occupying the lowest-energy single-particle states (a Fermi gas) and slowly "turns on" interactions. Landau argued that when interactions are turned on sufficiently slowly, the ground states of the Fermi gas and Fermi liquid are connected adiabatically. The physically intuitive picture of a quasiparticle is that of a "dressed" fermion that interacts with its environment as it propagates, altering its dynamical properties such as

its mass and magnetic moment. However, a one-to-one correspondence remains between the quasiparticle and the excitations of the original fermion, which have identical spin, charge, and momentum.

A key feature of the Fermi gas is the Fermi surface, which delineates occupied states from empty ones in momentum space. This follows from the Pauli exclusion principle, which forbids the double occupancy of a single state. Electrons fill momentum states $p < p_F$ (with p_F the Fermi momentum), leaving all higher momentum states unoccupied. In a Fermi liquid, the low-energy excitations are quasiparticles which are electron-like outside the surface and hole-like within. For excitations of electrons near the Fermi energy, the Pauli exclusion principle has another important consequence. Considering an excited electron with energy ϵ_1, its lifetime τ will satisfy $\frac{\hbar}{\tau} \ll \epsilon_1$ where $\hbar$ is Planck's constant and k_B is the Boltzmann constant. This electron can only scatter with another electron with energy ϵ_2, which must lie below the Fermi level (in an occupied state). These two electrons then must scatter into unoccupied states above the Fermi level, which by energy conservation must be given as

$$\epsilon_1 + \epsilon_2 = \epsilon_3 + \epsilon_4 \tag{1.1}$$

At zero temperature, an electron which lies at the Fermi level will never scatter due to the absence of available final states. At non-zero temperature, the electron may occupy thermal states within an energy difference $\Delta \sim k_B T$ above E_F. This results in a phase space restriction of the other three energies, which must lie within an energy shell of thickness Δ about the Fermi surface. For the case of two-particle scattering, this results

in a scattering rate of order Δ^2, and therefore a lifetime which varies as

$$\frac{\hbar}{\tau} \sim (k_B T)^2 \tag{1.2}$$

In this picture, one can arbitrarily reduce the scattering rate near the Fermi surface in a Fermi liquid by sufficiently reducing the temperature of the system. This feature results in a robust description of the low-temperature physics of interacting fermions, and indeed the Fermi liquid is a good model for the low-temperature state of most metals.

1.2 Phase transitions in condensed matter systems

When studying the emergence of phases in materials systems, one needs a quantitative framework for understanding how its constituents organize. To this end, an order parameter is defined as some quantity that is non-zero in its corresponding phase and zero otherwise.

1.2.1 Order parameters in Ginzburg-Landau theory

In Ginzburg-Landau theory, an order parameter is associated with a set of symmetries which are broken when traversing the transition from the parent structure to the resulting low-symmetry phase. For simplicity, we can consider a scalar order parameter ϕ and write down the lowest order terms in the corresponding Ginzburg-Landau free energy function as an expansion in ϕ[1]:

$$F_{GL} = F_0 + c_0|\phi|^2 + c_1|\phi|^4 + \cdots \tag{1.3}$$

[1]In general, order parameters can be functions of space and time, resulting in a free energy functional.

where c_n are real coefficients that are functions of a set of parameters (e.g. temperature, electric and magnetic fields, doping) which can be tuned to drive the system through a phase transition. This expansion is valid in the limit that the order parameter is small, i.e. near the phase transition.

1.2.2 The Ising model

The Ising model is a phenomenological model which describes phase transitions in the presence of interacting degrees of freedom on neighboring lattice sites. As is seen in 5 and 6, the Ising model plays a crucial role in the interpretation of the phase transitions studied in this thesis.

It is instructive to introduce the Ising model in the context of a familiar physical system: the ferromagnet in an external magnetic field, H. To simplify the model, we replace a quantum-mechanical spin operator with a value of $s_i = +1$ (spin up) or $s_i = -1$ (spin down) on lattice sites N, and the energy of the system is written as:

$$E = -J \sum_{\langle i,j \rangle} s_i \, s_j - \mu \, H \sum_{i=1}^{N} s_i. \tag{1.4}$$

where brackets indicate a sum over nearest neighbor lattice sites, μ is the atomic magnetic moment, and J is the exchange energy. As written, the energy is minimized for large positive J[2], i.e. spins aligned in the same direction.

[2]While the energy of magnetic dipole interactions between neighboring spins is usually $\sim 10^{-4}$ eV, the exchange interaction can be considerably larger (~ 1 eV). This is because the exchange energy arises from electrostatic interactions which are determined by the spatial separation of electrons, and by the Pauli exclusion principle (two electrons with the same spin cannot occupy the same site).

1.2.3 The mean-field approximation

To make progress in solving this model, one can employ the mean-field approximation in which each spin is considered to interact with a field which is the average of all neighboring spins:

$$e_i = -\frac{J}{2}\sum_{k=1}^{z} s_k\, s_i - \mu\, H\, s_i, \tag{1.5}$$

where the factor of $1/2$ corrects for double counting of nearest-neighbor pairs and z is the coordination number. We can write down a term for the effective magnetic field

$$H_{\text{eff}} = H + \frac{J}{2\,\mu}\sum_{k=1,z} s_k. \tag{1.6}$$

which lumps the external field H and the internal field created by the sum over neighboring atoms. If we then assume that all atoms (sites) have identical spins, the effective field becomes

$$H_{\text{eff}} = H + \frac{zJ\bar{s}}{2\mu}. \tag{1.7}$$

From statistical mechanics, the mean spin s of an atom in thermal equilibrium is given by the Boltzmann distribution as

$$s = \frac{\mathrm{e}^{\beta\,\mu\,H_{\text{eff}}} - \mathrm{e}^{-\beta\,\mu\,H_{\text{eff}}}}{\mathrm{e}^{\beta\,\mu\,H_{\text{eff}}} + \mathrm{e}^{-\beta\,\mu\,H_{\text{eff}}}}, \tag{1.8}$$

where $\beta = 1/k_B T$, and k_B is the Boltzmann constant. The above expression can be simplified as

$$\bar{s} = \tanh\left\{\beta\,\mu\,H + \beta\,z\,J\,\bar{s}/2\right\}, \tag{1.9}$$

where we have used the definition of H_{eff} from Equation 1.7 above. One can extract

a critical temperature for the phase transition,

$$T_c = \frac{z\,J}{2\,k_B}, \tag{1.10}$$

as well as a critical field

$$H_c = \frac{k_B\,T_c}{\mu} = \frac{z\,J}{2\,\mu}. \tag{1.11}$$

The model above can be generalized to describe the physics of other systems, including the polar and electronic nematic phases studied in this thesis. Despite its simplicity, the Ising model can capture the essence of highly complex materials systems, irrespective of their microscopic physical details.

Chapter 2

Nonlinear optical phenomena in materials

Nonlinear optical phenomena are those in which the optical properties of a material are meaningfully modified by the presence of light itself. These phenomena are "nonlinear" in the sense that the polarization density of the material depends nonlinearly on the electric field of the incident light. Typically, only laser light is sufficiently intense to induce these effects. With typical light sources, the magnitude of these effects tends to be much smaller than conventional (linear) optical phenomena. However, encoded in these responses is a plethora of information about the underlying structure of the material.

2.1 The nonlinear optical susceptibility

The nonlinear optical susceptibility is a tensor which provides rich details about the symmetry properties of a material. The discussion below will introduce some of the mathematical properties of the tensor, as well as a semi-classical and quantum-mechanical description of its physical origin.

To understand nonlinear optical phenomena, it is instructive to revisit the definition of the linear optical susceptibility. For linear processes, the dipole per unit volume (polarization) $\tilde{P}(t)$, depends linearly on the applied electric field $\tilde{E}(t)$ via the susceptibility χ^1 (a tilde indicates that a quantity varies quickly in time):

$$\tilde{P}(t) = \epsilon_0 \chi^{(1)} \tilde{E}(t), \tag{2.1}$$

where ϵ_0 is the permittivity of free space.

In nonlinear optics, the optical response can be expressed as a power series expansion of the polarization $\tilde{P}(t)$ in the field strength $\tilde{E}(t)$ as

$$\tilde{P}(t) = \epsilon_0 \left[\chi^{(1)} \tilde{E}(t) + \chi^{(2)} \tilde{E}^2(t) + \chi^{(3)} \tilde{E}^3(t) + \cdots \right] \tag{2.2}$$

where $\chi^{(2)}$ and $\chi^{(3)}$ represent second- and third-order nonlinear optical susceptibilities, respectively.

Electromagnetic waves from an incident light beam will induce a time-varying polarization in the medium through which it propagates. In turn, this polarization can act as a source of new components of the electromagnetic field. This source term $\boldsymbol{S}$ is in general composed of three terms corresponding to contributions from the electric dipole $\tilde{\boldsymbol{P}}$, the magnetic dipole $\tilde{\boldsymbol{M}}$ and the electric quadrupole $\tilde{\boldsymbol{Q}}$:

$$S = \mu_0 \frac{\partial^2 \tilde{P}}{\partial t^2} + \mu_0 \nabla \times \frac{\partial \tilde{M}}{\partial t} - \mu_0 \nabla \frac{\partial^2 \tilde{Q}}{\partial t^2} \tag{2.3}$$

The induced multipolar moments can be expressed as an expansion in the incident electric $\tilde{\boldsymbol{E}}$ and magnetic $\tilde{\boldsymbol{H}}$ fields (where tildes have been dropped for clarity):

$$\begin{aligned} P(\omega, 2\omega, \dots) \propto\ & \chi^{PE} E(\omega) + \chi^{PH} H(\omega) \\ & + \chi^{PEE} E(\omega) E(\omega) + \chi^{PEH} E(\omega) H(\omega) \\ & + \chi^{PHH} H(\omega) H(\omega) + O[(E(\omega), H(\omega))^3], \end{aligned} \tag{2.4}$$

$$\begin{aligned} M(\omega, 2\omega, \dots) \propto\ & \chi^{ME} E(\omega) + \chi^{MH} H(\omega) \\ & + \chi^{MEE} E(\omega) E(\omega) + \chi^{MEH} E(\omega) H(\omega) \\ & + \chi^{MHH} H(\omega) H(\omega) + O[(E(\omega), H(\omega))^3], \end{aligned} \tag{2.5}$$

$$\begin{aligned} Q(\omega, 2\omega, \dots) \propto\ & \chi^{QE} E(\omega) + \chi^{QH} H(\omega) \\ & + \chi^{QEE} E(\omega) E(\omega) + \chi^{QEH} E(\omega) H(\omega) \\ & + \chi^{QHH} H(\omega) H(\omega) + O[(E(\omega), H(\omega))^3]. \end{aligned} \tag{2.6}$$

The superscripts of the χ terms above indicate the nature of the incoming and outgoing fields. The magnitude of the higher-order susceptibilities χ^n decreases in n by approximately $1/E_{at}$, where E_{at} is the characteristic atomic field strength ($\sim 10^{11}$ V/m). Accordingly, very intense light is necessary to observe nonlinear optical signals.

2.1.1 Determination of point group symmetry via Second Harmonic Generation - Rotational Anisotropy

The leading-order response of the optical phenomena which generate light at 2ω is that of electric-dipole SHG, given by:

$$P_i(2\omega) = \chi_{ijk}^{PEE} E_j(\omega) E_k(\omega). \tag{2.7}$$

In the above, we have used the Einstein notation, where summation over repeated indices is implied. While nonlinear responses with higher-rank susceptibility tensors contain even more information about higher-order interactions, these effects are increasingly difficult to detect in measurement. The leading-order term P is typically $\lambda/a \sim 10^3$ times stronger than the magnetic dipole M and the electric quadrupole Q SHG term. In practice, the electric-dipole SHG is the most readily measured SHG signal and is therefore a powerful tool for symmetry determination.

SHG has a particularly useful property as a probe of crystalline and electronic symmetry: it vanishes identically in systems which have inversion symmetry. All crystals belong to one of 32 crystal classes and are uniquely determined by the set of symmetry operations which leave the crystal unchanged, known as the point group symmetry. Neumann's principle states that material property tensors such as χ must be invariant under the symmetry operations of the point group of the system. In systems which are centrosymmetric, the inversion operator flips the direction of the polar vectors P and E without changing the sign of χ. This maps the equation $P = \chi EE$ to $-P = \chi EE$ under inversion. The only solution that satisfies both equations simultaneously is that

Crystal System	$\boldsymbol{\chi^{(1)}}$ **Matrix**
Triclinic	$\begin{pmatrix} xx & xy & xz \\ yx & yy & yz \\ zx & zy & zz \end{pmatrix}$
Monoclinic	$\begin{pmatrix} xx & 0 & xz \\ 0 & yy & 0 \\ zx & 0 & zz \end{pmatrix}$
Orthorhombic	$\begin{pmatrix} xx & 0 & 0 \\ 0 & yy & 0 \\ 0 & 0 & zz \end{pmatrix}$
Tetragonal, Trigonal, Hexagonal	$\begin{pmatrix} xx & 0 & 0 \\ 0 & xx & 0 \\ 0 & 0 & zz \end{pmatrix}$
Cubic, Isotropic	$\begin{pmatrix} xx & 0 & 0 \\ 0 & xx & 0 \\ 0 & 0 & xx \end{pmatrix}$

Table 2.1: Linear susceptibility tensor $\chi^{(1)}$ for each of the seven crystal systems. The linear response contains much less information about the crystal symmetry. For example, it cannot distinguish between tetragonal, trigonal, and hexagonal crystals.

all elements of χ are equal to zero. Of the 32 crystal classes, 11 posses inversion symmetry, meaning crystals can be categorized as either centrosymmetric or not based on the absence or presence of bulk electric dipole SHG, respectively. This additionally makes electric-dipole SHG an exceptional probe of inversion-symmetry breaking transitions, such as the paraelectric-to-ferroelectric phase transition described in $SrTiO_3$ as discussed in 6.

The description above pertains to multiphoton processes which occur strictly at the resonant frequency of an electronic transition. This picture can be extended to excitation with light at nonresonant energies using quantum mechanic and second-order perturbation theory [5]:

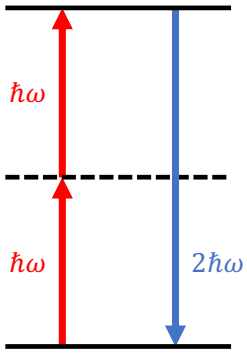

Figure 2.1: Schematic depiction of the SHG process. Two photons with energy $\bar{h}\omega$ are absorbed, and a single photon is emitted with energy $2\bar{h}\omega$.

$$\chi_{ijk}^{PEE} \propto \sum_{k} \sum_{mf} \frac{\langle g|P_i|f\rangle\langle f|P_j|m\rangle\langle m|P_k|g\rangle}{(E_f - E_g - 2\hbar\omega - i\gamma_{fg})(E_m - E_g - \hbar\omega - i\gamma_{mg})} + \dots \tag{2.8}$$

The above describes two instantaneous electric-dipole transitions at energy $\hbar\omega$ from initial state g to a virtual state m and then to the final state f. This two-photon absorption occurs simultaneously with a single-photon emission in a coherent quantum process at energy $2\hbar\omega$ – the second harmonic. Here the transitions between levels occur in accordance with Fermi's golden rule, with damping rates $\gamma_{mg,fg}$ governing the efficiency of the multi-photon process.

2.2 Experimental setup

2.2.1 Sample preparation

Samples are mounted on custom-made copper posts which are annealed to maximize thermal conductivity. A minimal amount of silver epoxy is used to attach the sample

to the post to ensure mechanical contact and heat transfer away from the sample during cooling. For thin film samples, particularly films grown by molecular beam epitaxy, minimal pre-treatment is performed to maintain the sample quality (i.e. no mechanical polishing, etching, etc.). For exfoliable crystalline samples, a fresh surface layer is generally exposed before mounting the sample in the cryostat. In many cases, scotch tape or duct tape is sufficient to remove a few layers. For samples which are difficult to cleave, a small alumina post is attached perpendicular to the sample surface using Torr Seal epoxy. The post is then knocked off, taking with it a layer of material and thus exposing a fresh surface. For crystals which are 1 mm or less in length, special methods are sometimes needed to mount the sample. Often, an eyelash taped to the end of a toothpick can serve as a manipulation tool to move and pick up the sample. For both silver epoxy and Torr Seal, curing occurs on a hot plate set to 80-100°C for at least 2 hours. A moderate temperature is used to minimize sample oxidation. Before mounting the sample in the optics setup, we inspect the sample surface for any damage (e.g. surface cracks, scratches from other measurements) and note which areas of the sample are best for measurement. We then move the sample to the optical sample aligner.

The sample aligner ensures that the surfaces of interest are oriented normal to the scattering plane of the optical setup. The working principle of the aligner is that a laser pointer is pointed through an aperture, passes through a beam splitter (Thorlabs CCM1-BS013), and is focused onto the sample at normal incidence. The sample is mounted on a dovetail translation stage (Thorlabs DTS25), which is in turn mounted on a rotation

stage. This allows the sample to move in the two in-plane directions as well as rotate about an axis perpendicular to the surface. After the beam is aligned to the center of the sample using positional adjustments, the incident laser light is reflected back onto the beam splitter, which reflects into a CMOS camera (Thorlabs DCC1545M-GL). The position of the beam on the camera detector is a function of the angle of incidence of the laser light on the sample. By bending the copper sample post, we align our sample surface such that we achieve normal incidence. The sample is then ready to be moved into the optical cryostat.

2.2.2 Laser light source and optical setup

The source laser for our SHG experiments is a 1040 nm ultrafast Yb-fiber laser operating at 500 kHz repetition rate (Spectra-Physics Spirit HE 1040-30). The pulses are linearly polarized with a beam average power of approximately 30 W, 10 W of which is directed into the non-collinear optical parametric amplifier (NOPA). We use a Spirit-NOPA-VISIR as an optical parametric amplifier to convert the 1040 nm source beam into a 800 nm signal and 1515 nm idler beam. The Spirit-NOPA-VISIR is comprised of two amplification stages. The first amplification stage is non-collinear and generates broadband white light, and the second amplification stage is collinear, which enables a broad tuning range. In practice, we fix the signal wavelength at 800 nm to generate a 400 nm SHG signal in our experiments. With the external prism-based compressor unit, the signal laser pulses can be compressed to $<$70 fs. A continuously variable metallic neutral

density filter is used to control the total average power of the beam. The beam diameter is reduced with a telescope consisting of a 2 plano-convex lenses with focal length 125 mm and -25 mm (Thorlabs LA1986-B, Thorlabs LC1054-B). A quarter wave plate (Thorlabs WPQSM05-808) converts the linearly-polarized light produced by the NOPA into circularly polarized light. This light then passes through a nanoparticle linear film polarizer (Thorlabs LPNIR050) which can be rotated between 0 and 90 degrees to select for S- or P-polarized light. We use a achromatic doublet (Thorlabs AC254-030-AB) to focus the laser beam to a spot size of approximately 30 μm in diameter. The output polarizer is a Glan-Thompson polarizer, which directs the desired polarization (S or P) onto the active area of the detector, which is a CMOS camera (ZWO ASI178MM). A bandpass filter (Thorlabs FBH400-40) removes the fundamental frequency from the measured SHG signal.

We use a reflection geometry with an oblique incidence at angle θ which allows us to probe both the in- and out-of-plane components of the polarization with respect to an incident beam with either in- or out-of-plane linearly polarized light. During a rotational-anisotropy experiment, we rotate the sample with respect to a fixed scattering plane through an angle ϕ. Using S and P polarized light, unit vectors describing the field in each channel are:

$$\begin{aligned}
&\mathrm{S_{in}}\text{ Polarization: } \hat{\epsilon} = \sin(\phi)\hat{x} - \cos(\phi)\hat{y} \\
&\mathrm{P_{in}}\text{ Polarization: } \hat{\epsilon} = -\cos(\theta)\cos(\phi)\hat{x} - \cos(\theta)\sin(\phi)\hat{y} + \sin(\theta)\hat{z} \\
&\mathrm{S_{out}}\text{ Polarization: } \hat{\epsilon} = \sin(\phi)\hat{x} - \cos(\phi)\hat{y} \\
&\mathrm{P_{out}}\text{ Polarization: } \hat{\epsilon} = \cos(\theta)\cos(\phi)\hat{x} + \cos(\theta)\sin(\phi)\hat{y} + \sin(\theta)\hat{z}.
\end{aligned} \tag{2.9}$$

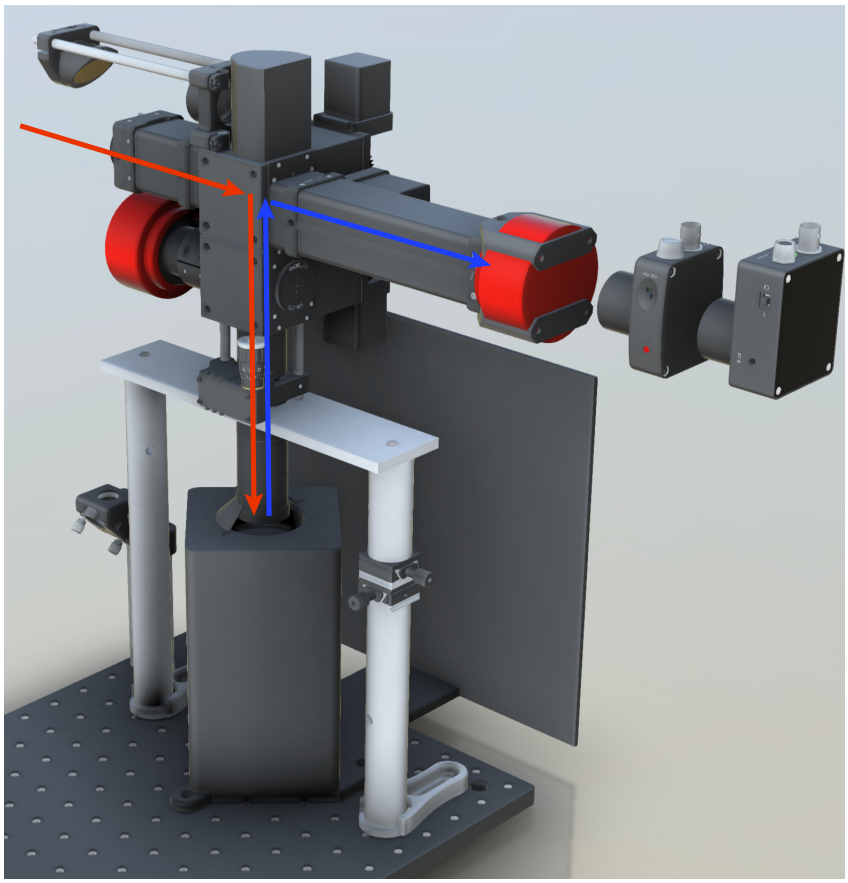

Figure 2.2: Schematic of the optical SHG-RA experimental setup. The 800 nm probe beam is linearly polarized and directed into the optical cryostat, where it interacts with the sample. SHG light is reflected back into the setup and steered toward a chosen detector, usually a CMOS camera.

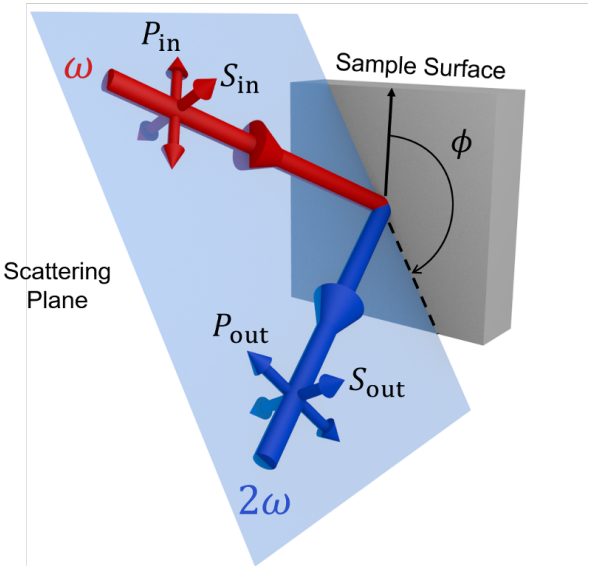

Figure 2.3: Experimental geometry of an SHG Rotational-Anisotropy measurement. Incoming and outgoing light can be either S- or P-polarized. The scattering plane (or equivalently the sample) is rotated about an axis normal to the sample surface which intersects the scattering plane at the point of specular reflection. Rotating the scattering plane allows measurement of the full nonlinear susceptibility tensor and determination of point group symmetry in non-centrosymmetric materials.

The measured intensity is then proportional to the square of the tensor element corresponding to the direction that is ϕ degrees away from the defined x-axis:

$$I(\phi) \propto |\chi_{ijk}\hat{\epsilon}_i\hat{\epsilon}_j\hat{\epsilon}_k|^2 \tag{2.10}$$

2.3 Data analysis

The output of our measurements is a column of numbers representing the SHG intensity at each orientation $\phi = 360°/N$, where N is the number of steps used to complete a full rotation. This yields a polar plot of SHG intensity versus the azimuthal angle ϕ, which we then fit to the anticipated form of the intensity for a given point group. We start with the expected point group symmetry based on crystallographic considerations and move to subgroups of the parent group if there is an additional broken symmetry. The non-zero elements of the $\chi^{(2)}$ tensor are referenced from [6].

To find the expected SHG intensity $I(\phi)$, we first define a $3 \times 3 \times 3$ rank-2 optical susceptibility tensor, $\chi^{(2)}$, with elements χ_{ijk}, where $i, j, k = x, y, z$ in the crystal frame. We apply the symmetry constraints for a crystal with a given point group symmetry to $\chi^{(2)}$, which results in a new tensor, χ^{crystal}. This transformation sets various elements of the tensor to either 0 or χ_{ijk}=$\chi_{\alpha\beta\gamma}$, where α, β, γ represent the x, y, z indices of symmetry-equivalent terms. We then define vectors that project the field from the incoming and outgoing beams for various polarization combinations, defined above in 2.9.The susceptibility tensor χ^{crystal} is then multiplied by the coordinate vectors for each combination of incoming and outgoing polarization, yielding the polarization in each of the four chan-

nels. In effect, the inner product of χ^{crystal} with each coordinate vector is calculated. For each pair of indices, the corresponding tensor elements are multiplied and then summed over the range of the index. The result of these operations is an expression for the polarization in each channel, respectively, that evaluates to a scalar for explicit values of θ and ϕ. We finally square the polarization expressions, resulting in four new expressions representing the squared magnitudes for each polarization combination (SS, SP, PS, and PP), a quantity which is proportional to the intensity. Details of the Mathematica code used to carry out these operations can be found in the appendix A.

In our setup, the angle of incidence $\theta = 10^{\circ}$, and the tensor elements are used as free parameters when fitting the SHG polar plots. Given that we measure intensity indirectly through a CMOS camera, we do not attempt to quantitatively assign values to the susceptibility tensor elements. However, a comparison between the polarization channels can often suggest which component of susceptibility dominates the response, as seen in the study of $SrTiO_3$ in 6.

Chapter 3

Pump-probe measurements with ultrafast lasers

The advent of reliable ultrafast lasers that deliver coherent and tunable light pulses has remarkably broadened the horizons of spectroscopy. With pulses spanning from a few to several hundred femtoseconds in duration, these laser sources can create non-equilibrium conditions in materials of interest on timescales faster than the energy exchange with lattice vibrations, magnetic excitations, and other degrees of freedom. This enables measurement of nonequilibrium phenomena which unveil information about a system which is hidden to time-averaged measurements. Further, it is possible to employ ultrashort light pulses as a mechanism to control the physical properties of transient electronic states on sub-picosecond timescales.

In traditional experiments, external stimuli are relatively weak and/or their dura-

tion is much longer than the characteristic interaction time among the system's internal degrees of freedom. As a result, a steady-state regime is reached much faster than the timescale of the measurement, providing only quasi-equilibrium information which may or may not map directly to the ground state of interest.

The primary advantage of ultrafast optical pump-probe spectroscopy is that both the external perturbation and the optical pulse which measures the resulting excitation take place on timescales much faster than the typical relaxation times. This allows for the observation of different thermalization processes, each with their own characteristic timescale. Via analysis of these relaxation dynamics, contributions from electronic, phononic, spin, and other degrees of freedom can be observed. The ability to resolve these relaxation dynamics opens a unique window into vital interactions within a material.

3.1 Pump-probe experimental setup

The recent successes of ultrafast optical methods are enabled by the reliable generation of ultrafast laser pulses. Modern pulsed laser sources consist of a mode-locked oscillator and a saturable absorber, the output of which is typically amplified in energy via chirped pulse amplification [7]. Pump-probe spectroscopy utilizes trains of these ultrafast pulses. An initial pulse – the pump pulse – excites the sample by creating oscillating dipoles and promoting electrons across energy band gaps. Excitation results in a highly non-thermal electron distribution, which subsequently seeks equilibrium through electron-electron and electron-phonon scattering, as well as through interactions with other degrees of freedom

(e.g. magnons). Optical pumps supply high-energy photons, which are much higher in energy than the low-lying excitations of condensed matter systems; however, THz radiation can be tuned on-resonance to excite collective modes.

Typically, a source laser is split into two beams which have the same pulse width and repetition rate. Optical parametric amplifiers are sometimes used to perform frequency conversion of the source laser when two-color spectroscopy is desired. A mechanical delay stage is introduced in one of the optical beam paths and systematically varies the time delay Δt between the pump and probe pulses through a differential path length. By incrementally increasing the time delay between the pump and probe pulses, one can readily obtain a discrete-time description of the dynamics of a material over a window of several hundred picoseconds (and in principle much longer with a sufficiently long delay line). With delay stages which can modulate mirror positions with micrometer precision, one can achieve time resolution on the order of tens of femtoseconds.

In addition to time domain resolution, pump-probe experimental setups need a high degree of sensitivity to detect small changes to the optical response. Typically, the pump beam is periodically switched on and off by an optical chopper with a frequency of several hundred Hz to kHz. Pump modulation, in tandem with lock-in detection, enables averaging over low-frequency noise such as laser power fluctuations, resulting in an excellent signal-to-noise ratio.

3.1.1 Excitation in the weak-perturbation regime

When one is concerned with studying the ground state properties of a material, it is desirable to use a pump fluence which is relatively weak such that the free-energy landscape of the underlying system remains mostly unmodified after optical perturbation. In the so-called weak-perturbation regime, relaxation from the excited state is governed by the same scattering processes which occur at equilibrium, and these processes result in a return to the true ground state rather than a local free-energy minimum. Additionally, sufficiently short pump pulses can induce coherent oscillations of collective modes which can manifest as a sine-type modulation of the measured optical signal, e.g. the transient reflectivity. Through this sensitivity to decay processes, pump-probe spectroscopy is a powerful tool for probing and disentangling interacting degrees of freedom in condensed matter [8].

For pump-probe experiments performed in a reflection geometry, the transient reflectivity $\Delta R/R$ is given by

$$\Delta R/R = A_1 \exp(-t/\tau_1) + A_2 \exp(-t/\tau_2) + \ldots + A_n \exp(-t/\tau_n), \tag{3.1}$$

where A_n and τ_n are the amplitude and lifetime of a given relaxation process, respectively. A typical reflectivity transient is characterized by a sharp increase or decrease at $t = 0$ (referred to as "time-zero"), which is the time at which the pump and probe pulses overlap. If the material has fully reached equilibrium between sequential pump pulses, the pre-time-zero signal will be zero. Otherwise, the magnitude of this signal carries information about a long-lived metastable state, which can be studied by varying

the pump fluence. After the sharp change in reflectivity, the non-thermal electrons will begin transferring their energy to other degrees of freedom. The strength of this scattering process is captured by A, and its timescale by τ. Often, the electronic subsystem will equilibrate quickly within the first several hundred femtoseconds to single picoseconds, followed by a longer lattice relaxation that lasts several to tens of picoseconds or longer. When the electron-electron scattering takes place much faster than the electron-phonon scattering, an effective two-temperature model is often used to describe equilibration.

The Two-Temperature Model and its limitations

The two-temperature model (TTM) is a fundamental phenomenological model for describing the equilibration of optically pumped systems, typically where magnetic degrees of freedom are not present (though multi-temperature extensions of the model exist).

In the TTM, one assumes that the electron-electron relaxation is much faster than that of the electron-phonon. Electron-electron scattering eventually reestablishes a Fermi-Dirac distribution of electrons with temperature T_e, typically with a characteristic timescale of tens to hundreds of femtoseconds. The subsequent equilibration is due to the transfer of energy to strongly coupled phonons at an effective temperature T_p. The relationship between the electron-phonon coupling strength λ and the relaxation time τ in this model is known [9] and given by

$$\lambda\langle\omega^2\rangle = \frac{\pi}{3}\frac{k_B T_e}{\hbar\tau} \tag{3.2}$$

Often, when a two-temperature model is employed to interpret ultrafast data, the

two temperatures are taken to be purely those of the electrons and the phonons, and it is assumed that electron-electron thermalization is much faster than electron-phonon thermalization. However, this limit is only reached for high excitation densities, where the Pauli blocking constraint is relaxed. In the weak-perturbation regime, high excitation densities are likely not reached, which undercuts the validity of the TTM. In this scenario, it is not necessarily the case that electron-electron scattering is much faster than phonon scattering, i.e. hot phonons may scatter with electrons on a similar (fast) timescale as typical electron-electron scattering. However, it has been shown that the phonon component of the initial fast excitation simply results in a constant scaling of the predicted temperature increase [10], meaning that the TTM can often still capture the qualitative behavior of systems under optical pumping at low fluence.

3.2 Coherent phonon spectroscopy

Coherent phonon spectroscopy is a powerful way to study the response of a material to incident radiation. Much of the recent work in this area focuses on so-called non-linear phononics, whereby selective modifications of the lattice can be achieved by resonantly pumping an infrared active phonon with terahertz frequency radiation [11].

With frequencies much higher than the resonant frequencies of phonons and other modes, optical perturbation can still induce coherent oscillations. Two primary modes of excitation exist: impulsive stimulated Raman scattering (ISRS) and displacive excitation of coherent phonons (DECP). In both processes, phonons interact with electrons that

occupy intermediate electronic states. The lifetime of these states influences the details of the driving force $F(t)$, which takes the form of a driven harmonic oscillator along the normal coordinates Q of an optical phonon [12]:

$$\frac{d^2Q}{dt^2} + 2\gamma\frac{dQ}{dt} + \frac{dV(Q)}{dt} = F(t) \tag{3.3}$$

Here, γ and $V(Q)$ are the damping rate and lattice potential of optical phonon, respectively. In the harmonic approximation, the bare lattice potential is given as $V(Q) = \frac{1}{2}\omega_0^2 Q^2$, where ω_0 is the phonon frequency.

Impulsive and displace mechanisms result in oscillations of collective modes with different phases with respect to the optical pump. While an ultrashort pulse is interacting with a non-absorbing material, the driving force can be expressed as [8]

$$\chi \propto \frac{\partial^2 F(t)}{\partial Q^2} E(t)^2 \tag{3.4}$$

with χ the linear dielectric susceptibility. In this case, the $\chi\frac{\partial}{\partial Q}$ term, the Raman tensor, hints at a Raman-type mode with sine-like oscillations (non-zero derivative at time-zero). In the case of an absorbing material (metal or narrow band-gap semiconductor), the pulse can interact with phonons via a long-lived real electronic state. In this case, a displace driving force occurs:

$$F(t) \propto \int E(t')dt' \tag{3.5}$$

In this case, the ions are displaced toward new lattice coordinates in the excited state, resulting in cosine-type oscillations. This phase difference of $\pi/2$ of the coherent oscillations allows one to distinguish between different mechanisms of excitation, especially

when both are simultaneously active.[13]. Oscillations driven by DECP retain the full symmetry of the crystal, i.e., they transform like A_1 [14]. A powerful application of coherent phonon spectroscopy is to detect changes in lattice symmetry, which can be inferred from phonons which appear or disappear at a given temperature/critical point (e.g. doping, pressure, strain) [15]. These changes in symmetry are accompanied by new active phonon modes, which signal a phase transition. In general, phonons with different symmetries will couple differently to the electronic and lattice order, and are therefore capable of disentangling intertwined degrees of freedom [16].

3.3 Practical considerations

To achieve an improved signal-to-noise ratio and to keep experimental runs as short in time as possible, it is often tempting to increase the average power of the incident laser. While this approach will undoubtedly provide a greater number of measurable photons, one must be careful not to inadvertently enter the strong-perturbation regime. In general, one can check for the absence of nonlinear pump-induced effects by taking repeated measurements at higher and lower values of fluence, controlled through the average power and repetition rate of the laser. If increasing the pump fluence results in a response that is not proportional to the response at lower fluence, care must be taken to account for the fluence dependence of the observed phenomenon.

Additionally, laser fluence should be kept sufficiently low to avoid optical damage, which is an undesirable outcome of nearly any measurement. When ultrafast pulsed

lasers are used, the dominant damage mechanism is typically avalanche breakdown [6]. In this mechanism, a small number of free electrons are accelerated to high energies by the laser field and then impact-ionize other atoms in the material. Electrons from these impacted atoms are then free to accelerate in the laser field, impact-ionizing other atoms and so on. These electrons heat the sample locally and can lead to melting or cracking, usually at the sample surface.

Another key experimental consideration is that of spatial overlap between the pump and probe beams, particularly if the two are not collinear. For example, for a pump at normal incidence and a probe at oblique incidence, one must ensure that the two beams are focused onto the same plane and are located at the same position on the sample surface. Although this is fairly straightforward to do at a single temperature, thermal expansion of instruments and samples can lead to positional drift of the two beams when measuring over a wide range of temperature. Generally, a beam at normal incidence will have minimal deviations from its initial position, whereas the beam spot from the probe at oblique incidence will move out of alignment. Careful measures should be taken to ensure that the signal is not artificially low due to misalignment and that measurements across different temperatures are consistent.

Chapter 4

Growth of thin film oxides via molecular beam epitaxy

Advancement in film growth methodology has been essential for the progress of fundamental materials physics. Atomic-scale precision is often required for the most interesting phenomena to emerge, as even the presence of a tiny number of defects can obscure the true ground state of a system. Molecular beam epitaxy (MBE) was first demonstrated by Cho and Arthur at Bell Labs [17], and has since become the premier method by which to grow virtually perfect crystals to explore and discover new physics. The method works by evaporating atoms (or molecules) onto a heated substrate, which then crystallize into the desired compound. By adjusting the stoichiometry and temperature, MBE achieves control over single atomic layers. Breakthroughs employing metal-organic and reactive oxygen sources have extended the reach of MBE methods from simple III-V semiconduc-

tors to ABO_3 perovskites and other complex oxides.

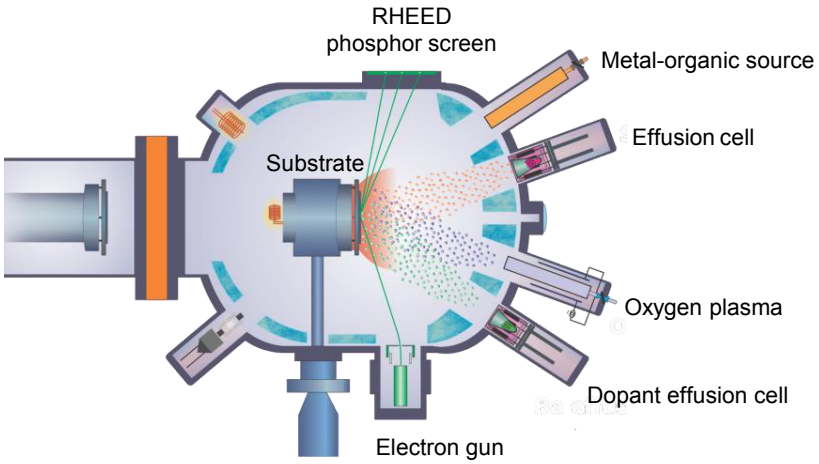

Figure 4.1: Schematic of the molecular beam epitaxy chamber used to grow the $SrTiO_3$ films discussed in this thesis. Figure provided by the Stemmer group at UCSB.

4.1 Growth parameters

With complex oxide materials sensitive to minute defect densities (e.g. as low as 10^{-18} cm^{-3} cation nonstoichemetry in $SrTiO_3$ [18]), it is preferable to eliminate as many unintentional defects as possible. In MBE, atomic and molecular species arrive at the growth front with a small kinetic energy. This is preferable because beams of high kinetic energy particles, even at low fluence, can introduce undesired point defects such as interstitials, antisite defects, and oxygen vacancies [19]. This puts the method at an advantage compared to physical vapor deposition techniques such as PLD or sputtering; while it is less than ideal for high-volume manufacturing, this allows for a significant reduction of unwanted intermixing of atomic species and phases.

Another important growth parameter is the mean free path inside the growth chamber, given as

$$\lambda = \frac{k_B T}{\sqrt{2}\pi d^2 P} \tag{4.1}$$

where k_B is the Boltzmann constant, T is the temperature, d is the diameter of the atom or molecule, and P is the chamber pressure. Importantly, by sufficiently decreasing the pressure, one can ensure that λ is much greater than the distance between the molecular beam source and the substrate, limiting the contact of species that do not arrive in a straight line from the chemical source. This eliminates any parasitic chemical reactions that occur before the species reach the growth front, which plague low-pressure techniques such as chemical vapor deposition. Additionally, the high mean free path allows for near instantaneous on/off switching of depositions via beam shutters without the need to pump out precusor species [20]. The low deposition rate ($\sim$Å per minute) and the high mean free path also allow *in situ* monitoring of growth by reflection high-energy electron diffraction (RHEED) [21], XPS[22], and other methods.

4.1.1 Challenges for complex oxide MBE

An adsorption-controlled growth window enabled great results in early efforts with binary semiconductors, for example GaAs. By using a heated substrate, there exists an accessible region in which the As vapor pressure is too low to form solid As on the substrate while simultaneously being high enough to prevent decomposition of GaAs. This window at a temperature of around 600°C is roughly nine to ten orders of magnitude larger than the As

vapor pressure [23]. This affords facile growth of GaAs: So long as As is supplied in excess, every Ga atom will find a partner As atom while excess As desorbs. Unfortunately, the adsorption-controlled method falls short for many complex oxides, for which the growth window is often much narrower, if it exists at all.

A prominent example, $SrTiO_3$, is one such material with no adsorption-controlled growth window. Both Sr and Ti form stable binary oxides in an oxygen environment (SrO and TiO_2, respectively), resulting in extremely high and experimentally inaccessible temperatures for the formation of SrO(g) and TiO_2(g). Without unrealistically precise control over flux ratios, these binary oxide phases will be incorporated into the film during growth. Even for compounds with extant (if narrow) growth windows, sometimes control of molecular beams is simply insufficient: at present, there is no characterization method that can provide control of stoichiometry with an accuracy better than 1%.

The epitaxial growth of transition metal oxide thin films (TMOs) faces several challenges, including significantly higher defect concentrations compared to those of conventional semiconductors. These defects are mostly attributed to variations in the ratio of oxygen and cations, as well as the presence of mixed-valence cations. Oxygen vacancies can form more readily in TMOs, which can trigger changes in the electron concentration, average transition metal valence, or both. Furthermore, overly oxidizing conditions can lead to cation defects and the formation of unwanted secondary phases, especially binary oxides. Electron doping is particularly deleterious to the growth of TMOs which require very low carrier concentrations. In other semiconducting systems, post-growth

annealing is a viable strategy to remove cation vacancies via recrystallization; however, these processes are typically performed at some large fraction of the melting temperature ($\sim 0.7T_m$). For complex oxides with melting temperatures exceeding 1500°C, this is experimentally impractical. High melting temperatures are also associated with slow kinetics, which limits the formation of strain-relieving misfit dislocations at film-substrate interfaces.

4.2 MBE for materials of interest

4.2.1 $SrTiO_3$ and hybrid MBE

In addition to the challenges surrounding growth windows, complex oxides of scientific interest often contain transition-metal elements with extremely low vapor pressures. With conventional MBE growth, this limitation would typically require a chemical source such as electron beam evaporation, which results in flux with undesirably high kinetic energy. Hybrid MBE circumvents this issue by instead using an elemental source in a solid phase, a metal-organic source, and oxygen in the gas phases. An advantage of this technique for the growth of complex TMOs is that the supply of gaseous metal-organic (MO) is low energy and very stable [24].

The use of hybrid MBE has resulted in highly successful growth of epitaxial films of $SrTiO_3$ [25, 26]. The MO precursor of choice for the growth of $SrTiO_3$ is titanium tetra-isopropoxide (TTIP) (chemical formula $Ti(OCH(CH_3)_2)_4$). In TTIP, a central $Ti_4{}^+$

is bonded to four oxygen atoms that help reduce oxygen vacancies compared to growth using elemental Ti sources. When TTIP adsorbs at the growth front, it decomposes at high temperature into TiO_2 and volatile organic byproducts which do not incorporate into the film. At temperatures exceeding 700°C, a *desorption* limited growth window opens, limited by the TTIP desorption rate from the surface. Using this technique, $SrTiO_3$ films have been grown which have low-temperature mobility which exceeds that of even bulk crystals [27, 28].

4.2.2 Sr_2RuO_4

Although incredibly pure crystals of Sr_2RuO_4 are now routinely grown with a mean free path of more than 1 μm [29], superconducting thin films grown by MBE are a more recent development [30]. Importantly, for Sr_2RuO_4 to remain superconducting, the presence of point defects or out-of-phase boundaries must be avoided, as these imperfections can suppress the fragile superconductivity in Sr_2RuO_4 thin films. Recently, an adsorption-controlled growth window has been reported for films of Sr_2RuO_4, in which Sr_2RuO_4(s) is in equilibrium with RuO_x(g) ($x = 2$ or 3). The growth window, calculated for an incident excess ruthenium flux of 1.3×10^{13} $cm^{-2}s^{-1}$, is rather narrow, highlighting the difficulty of growing superconducting Sr_2RuO_4 thin films. This narrow window arises from the small difference in Gibbs formation energies between Sr_2RuO_4 and $Sr_3Ru_2O_7$ [31].

In the region of higher temperature and higher oxygen pressure above the green phase

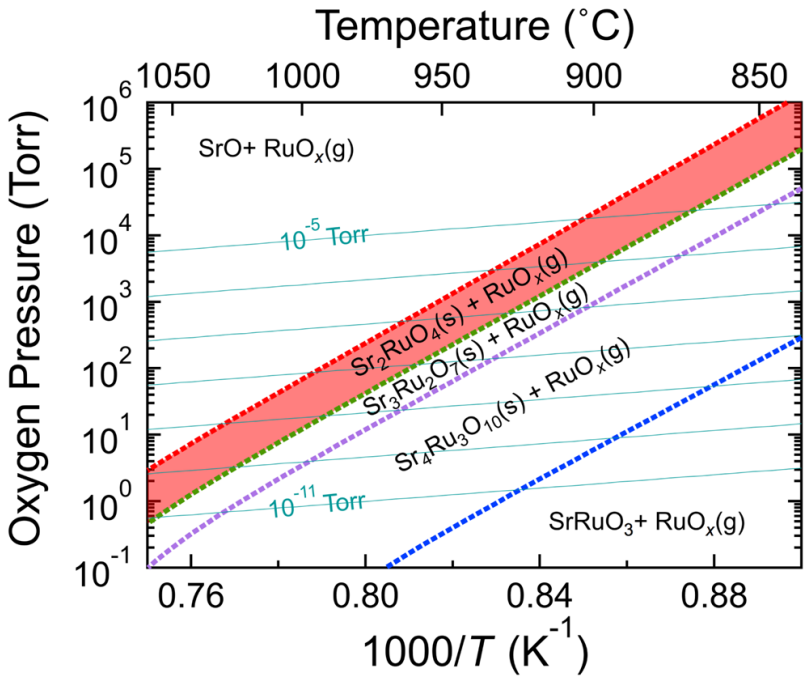

Figure 4.2: Thermodynamics of molecular-beam epitaxy (TOMBE) diagram for the $Sr_{n+1}Ru_nO_{3n+1}$ Ruddleson-Popper phases. The adsorption-controlled growth window for Sr_2RuO_4 is highlighted in red. Reproduced from [31]

boundary in Figure 4.2, Sr_2RuO_4 breaks down into SrO(s) and RuO_x(g), while in the region of lower temperature and lower oxygen pressure, the formation of $Sr_3Ru_2O_7$(s) becomes thermodynamically favorable. High substrate temperatures are crucial to achieve superconducting Sr_2RuO_4 thin films, primarily because they enhance the adatom surface migration length, thus increasing the spacing between out-of-phase boundaries. High substrate temperatures also help to overcome kinetic barriers to growth.

4.3 Considerations for optical measurements

When performing optical measurements of thin films in a reflection geometry, complications can arise when the substrate is tranparent to the incident light. Reflections from the film-substrate interface, and particularly reflections from the bottom of the substrate, can complicate data collection and interpretation. For SHG measurements, one is often concerned with detecting symmetry breaking in the bulk of a noncentrosymmetric film; however, SHG signals such as surface electric-dipole SHG can arise at interfaces, even between centrosymmetric materials. When measuring samples grown on transparent substrates, measures should be taken to ensure that these unwanted contributions to the measured SHG intensity are minimized or eliminated via control of experimental geometry, e.g. the angle of incidence.

Another complicating factor for certain substrates is the presence of green and blue luminescence in complex oxides, particularly $SrTiO_3$ and $KTaO_3$. It is known [32, 33, 34, 35] that these perovskite materials have a broad photoluminescence at low temperature, re-

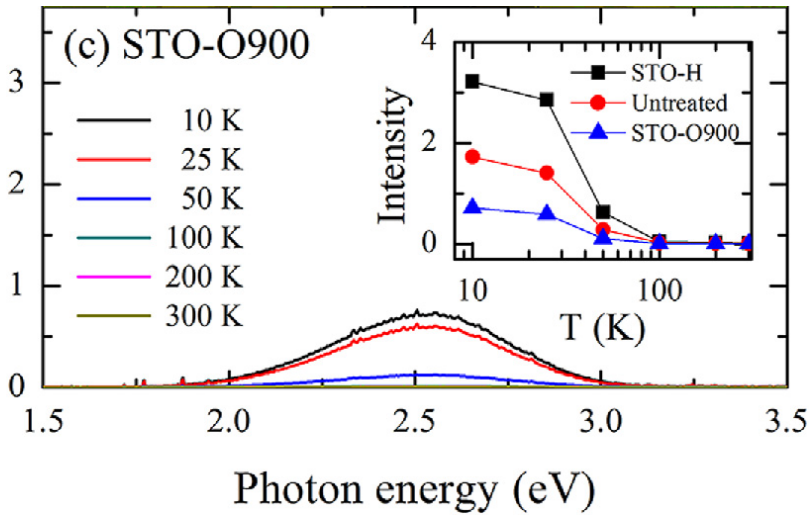

Figure 4.3: Photoluminescence centered around 2.5 eV (496 nm) observed in $SrTiO_3$. When attempting to measure SHG at 400 nm, it is important to consider other broad emissions that may have intensity at the measured wavelength and obscure the SHG response. Reproduced from [33]

lated to defect-induced in-gap states. The increasing photoluminescence intensity with decreasing temperature has been associated with the suppression of the nonradiative decay of excited electrons due to the reduction of thermal phonons [33]. If SHG measurement is carried out using a band-pass filter (e.g. incident light at 800 nm and expected SHG measurement at 400 nm), it is possible that the photoluminescence will have some intensity at the wavelength of interest. Especially when using an incident beam with high fluence, it is important to check the full spectrum of the measured light to ensure that it is indeed narrow-bandwidth SHG.

Chapter 5

Electronic nematicity in the normal state of Sr_2RuO_4

5.1 Normal state properties of Sr_2RuO_4

5.1.1 Crystal structure

Sr_2RuO_4 is a perovskite material that is isostructural to the parent compound of the famous cuprate superconductors, La_2CuO_4. Square lattice planes of RuO_2 are separated by layers of SrO. The space group of the body-centered tetragonal compound is $I4/mmm$ with lattice parameters $a = 3.862$ Å, $c = 12.772$ Å in the bulk [36]. Sr_2RuO_4 is somewhat unusual among the perovskite oxides in that its RuO_6 octahedra do not rotate as a function of temperature, yielding a simpler crystalline and electronic structure.

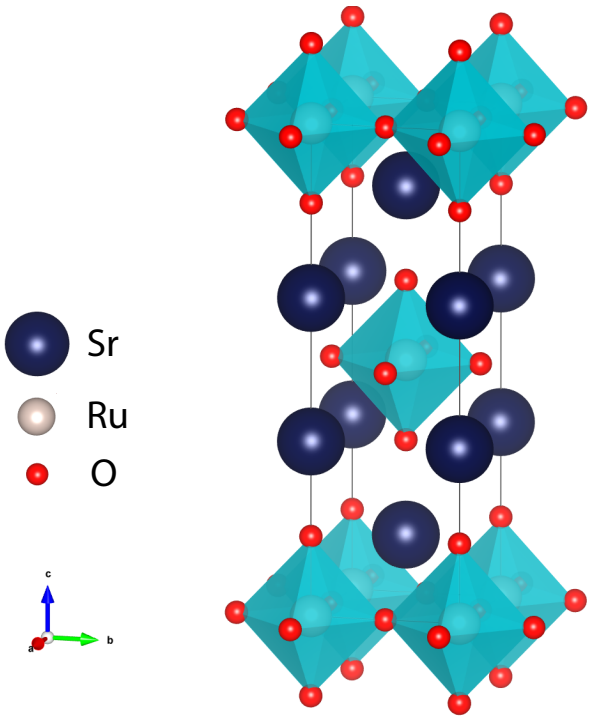

Figure 5.1: Crystal structure of Sr_2RuO_4, which exhibits $I4/mmm$ symmetry (space group 139). Square lattice RuO_2 planes are well separated by layers of SrO. Ruthenium ions are octahedrally coordinated by oxygen.

5.1.2 Electronic band structure

An octahedral crystal field splits the $4d$ electronic states of the Ru ions into lower-lying t_{2g} states and higher e_g states. The ruthenium ions have a formal charge of 4^+, and 4 electrons occupy the lower t_{2g} manifold. The Ru d orbitals hybridize with neighboring oxygen p orbitals, resulting in two quasi-1D bands with d_{xz} and d_{yz} character and one quasi-2D band with d_{xy} character. The Fermi surface is almost entire two-dimensional given the large interplane distance between RuO_2 sheets with very weak k_z dependence.

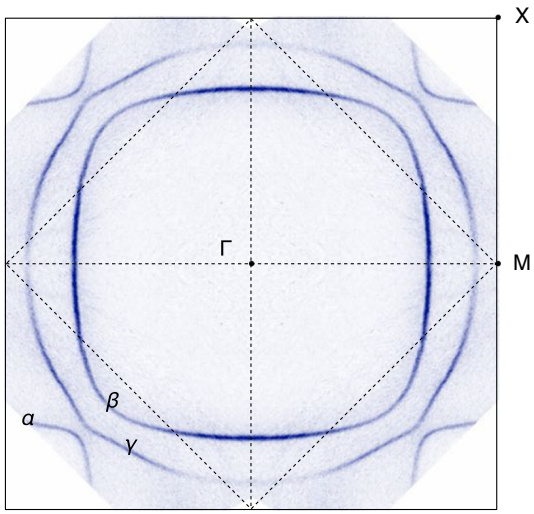

Figure 5.2: Fermi surface of Sr_2RuO_4 at $k_z = 0$ as measured by high-resolution laser-ARPES, demonstrating the three bands present at the Fermi energy (α, β and γ). Figure reproduced from Ref. [37]

5.1.3 Fermi liquid state

Sr_2RuO_4 is observed to undergo a tranisiton to a Fermi liquid state at ∼40 K as seen in Hall transport [38, 39, 40] , optical spectroscopy [41], and nuclear magnetic resonance

[42, 43]. Resistivity which varies with T^2 is observed as well as expected electronic T-linear and phononic T^3 contributions to the specific heat at low temperature [44]. A thorough investigation of quantum oscillations also points to the Fermi liquid state [45]. Quasiparticle parameters such as effective mass m^* provide information about the correlations present in each band: the quasiparticles originating from the α, β, and γ bands are enhanced beyond their band masses by a factor of 3.0, 3.5, and 5.5, respectively, pointing to the presence of strongest correlations in the γ band.

5.2 Strain as a tuning parameter

Many recent investigations of Sr_2RuO_4 have used what is sometimes referred to as uniaxial strain[1] to access a van Hove singularity (vHS) that exists in the γ band ~ 14 meV above the Fermi level [46]. Tuning the Fermi level through this vHS induces a Lifshitz transition in the γ sheet, where it changes from a closed electron-like band to an open contour at the M-point of the Brillouin zone. The most dramatic consequence of compressively straining Sr_2RuO_4 through the vHS is that the superconducting T_c grows by a factor of approximately three [47]. Strain has also been used to observe an ordered static magnetic state [48], to study the potential two-component nature of the superconducting order parameter through heat capacity[49], and recently to map out the phase diagram of the normal state using the elastocaloric effect [50].

[1]The term uniaxial strain is used to indicate that a sample is stressed only along one direction, and the other crystal surfaces are unconstrained and free to expand/contract as determined by the relevant Poisson ratio. There is technically no such thing as a uniaxial strain, only a uniaxial applied stress. Any applied stress, in general, will result in a multi-component strain.

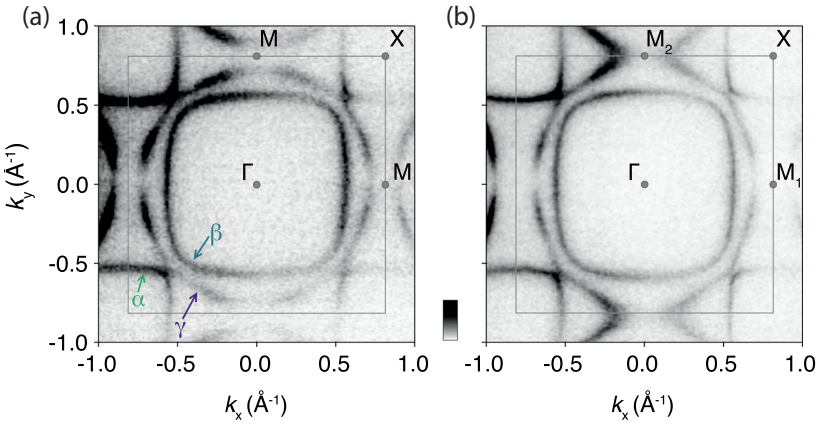

Figure 5.3: Direct measurement of the uniaxial stress-driven Lifshitz transition via ARPES. The γ band undergoes a topological transition from a closed, electron-like band to an open contour at the M point of the Brillouin zone. Figure reproduced from Ref. [51].

5.3 Previous reports of nematicity in Sr_2RuO_4

The inspiration for investigating the nematicity in Sr_2RuO_4 came from the original report of electronic nematicity in angle-resolved transport in epitaxial thin films [52]. In this study, both the longitudinal and transverse resistivity were measured as a function of in-plane angle (ϕ). In a C_4 tetragonal material, the longitudinal resistivity must be isotropic and the transverse resistivity must be zero at every angle by symmetry. Instead, what is found is electronic transport consistent with C_2, or two-fold rotational symmetry, which follows the form

$$\rho(\phi) = \rho + \Delta\rho \cos[2(\phi - a)], \tag{5.1}$$

$$\rho_T(\phi) = \rho_T^0 \sin[2(\phi - a)] \tag{5.2}$$

where $\rho = \frac{(\rho_{\max}+\rho_{\min})}{2}$. An example of the transverse transport anisotropy is shown in Figure 5.4. The magnitude of the nematic order was found to increase with cooling and

appears to diverge near 0 K. Interestingly, the amplitudes of nematicity are substantial and nearly equal in Sr_2RuO_4/LSAT (tetragonal) and Sr_2RuO_4/$NdGaO_3$ (orthorhombic), indicating that the transport nematicity occurs in the absence of a symmetry-breaking strain.

Nematicity is also reported to occur at the surface of Sr_2RuO_4 in the form of checkerboard charge order via rotation of the RuO_6 octahedra [53]. Notably, this nematicity was measured by scanning tunneling microscopy (STM), a probe that is sensitive to local order. Here a combination of checkerboard charge order centered at the Sr sites and the octahedral rotation induces an inequivalence between the oxygen atoms in the Ru plane, i.e. there is a difference between oxygens along the horizontal [10] and vertical [01] directions. The observation of unequal electron density across oxygen atoms corroborates our model of electronic nematicity as observed by optical pump-probe measurements discussed below.

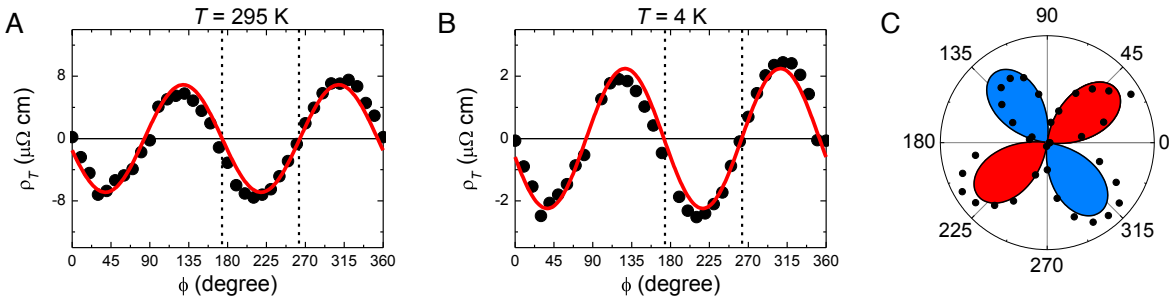

Figure 5.4: Angle-resolved transverse resistivity of a Sr_2RuO_4 film grown on $NdGaO_3$ shows a nematic transport anisotropy. Panels A and B show the nematic transport near room temperature and at 4 K, respectively, demonstrating that the phenomenon survives to room temperature. (Figure reproduced from Ref. [52], Copyright 2020 National Academy of Sciences).

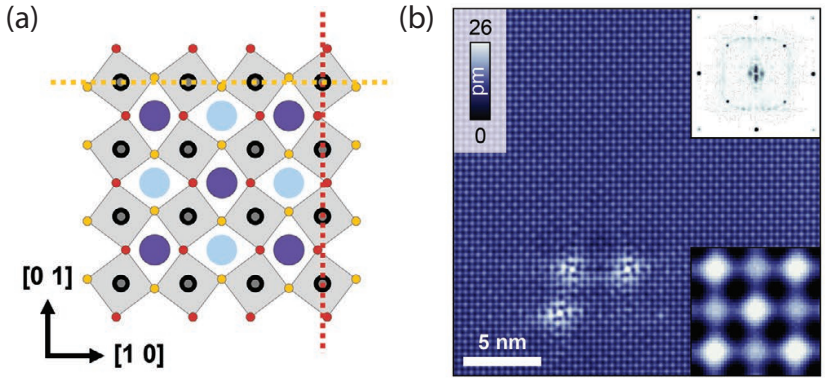

Figure 5.5: Checkerboard charge order at the surface of Sr_2RuO_4. (a) A schematic representation of the checkerboard charge order at the surface. (b) Topography as measured by STM at $V = -5$ mV from the SrO-terminated surface, demonstrating checkerboard charge order. Inset displays Fourier transform showing increase of intensity at (π, π) (Figure reproduced from Ref. [53]).

5.3.1 Theoretical description of the electronic nematic phase

The description of a nematic phase in general originates in the study of liquid crystals, wherein a phase was discovered which has no long-range positional ordering of molecules but breaks the typical full-rotational symmetry of a liquid. In such a system, rod-like molecules orient themselves along a headless vector called a director, which indicate a line in 3D space without a sense of a positive or negative direction.

Electronic nematics, by analogy, are phases in which the electron fluid breaks the rotational symmetry of the underlying atomic lattice. As it pertains to the work in this thesis, the nematic phase transition is characterized by a transition from C_4 (four-fold rotational) symmetry of a tetragonal material to C_2 (two-fold rotational) symmetry. The axis of the C_2 symmetry acts as the "director" of the electronic nematic phase and is often pinned to a lattice vector. In the most general case (i.e., in the absence of a lattice),

the order parameter is determined by some angle $0 \leq \theta < \pi$ [54]:

$$\phi_N = \phi e^{i2\theta} \tag{5.3}$$

On a square lattice – the lattice of interest – we assume that ϕ will lie along either the x or y axis, or equivalently $\theta = 0$ or $\pi/2$. Considering the order parameter at a point (discarding any spatial dependence $\phi(r)$), we can construct a Landau free energy density, f. The free energy must respect the symmetries of the lattice, so f must not change under 90° rotations (C_4 symmetry). For $\theta \to \theta + \pi/2$ (i.e. a 90° rotation), $\phi_N \to -\phi_N$, thus f can only contain even powers of ϕ_N:

$$f = \alpha\phi_N^2 + \beta\phi_N^4 + \gamma\phi_N^2(\nabla\phi_N)^2 + \dots \tag{5.4}$$

As seen in Chapter 1, this is the same form as the order parameter for the Ising ferromagnet.

5.4 Optical dichroism in the linear reflectivity

Nematic order spontaneously breaks rotational symmetry while preserving translational symmetry. In a tetragonal crystal, nematicity results in a lowering of symmetry to an orthorhombic unit cell where the a and b directions become nonequivalent. The spontaneous nature of the symmetry breaking invariably leads to the formation of domains related by 90° rotations, whose average over long length scales retains the parent tetragonal symmetry. Thus, directly detecting nematic symmetry breaking with macroscopic probes generally requires stabilizing the formation of one type of domain, akin to struc-

tural detwinning. Uniaxial strain is an ideal external conjugate field by which one can achieve this effect. In the iron-based superconductors, for example, uniaxial strain has been used to study nematic order with optical, transport, and photoemission experiments [55, 56, 57, 58, 59]. Here, we take advantage of uniaxial epitaxial strain to enable macroscopic transient optical reflectivity measurements of electronic nematic order in Sr_2RuO_4.

We study high-quality thin films of (001)-oriented Sr_2RuO_4 grown on (110)-oriented NdGaO3 and (001)-oriented LSAT substrates by molecular-beam epitaxy [60]. The films are coherently strained to (110) $NdGaO_3$ single-crystal substrates [61], guaranteeing a clean, uniform strain field over the entire sample area. Transport measurements confirm the films are superconducting, with a critical temperature of $T_c \approx 1.4$ K .

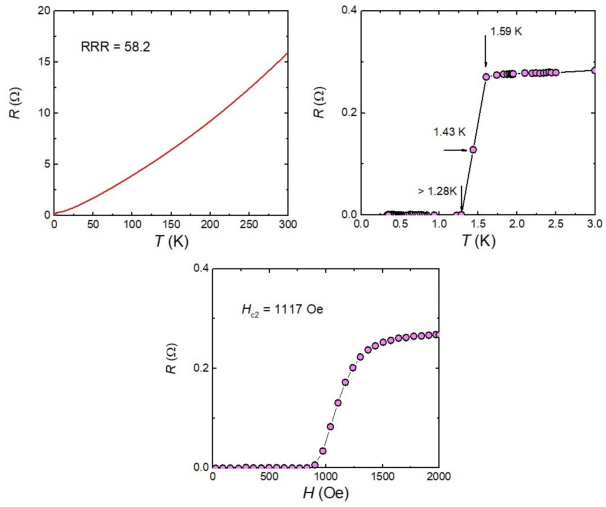

Figure 5.6: Superconducting properties of Sr_2RuO_4 thin films. The electrical resistance versus temperature of a film grown on (110) $NdGaO_3$ shows a residual resistivity ratio (RRR) of 58.2. The superconducting transition at $T_c \approx 1.4$ K is accompanied by a sharp drop in resistance to zero. T_c is observed to decrease with applied magnetic field, until superconductivity is completely suppressed above a critical field of $H_{c2} \approx 1117$ Oe.

$NdGaO_3$ induces a small uniaxial (B_{1g}) strain of $a/b - 1 \approx 0.3\%$ at low temperatures, where a and b are the in-plane lattice constants of the Sr_2RuO_4 film. Specifically, a and b correspond to the $[1\bar{1}0]$ and [001] spacings, respectively, of the (110) $NdGaO_3$ substrate in the *Pbnm* setting [61] (Figure 5.7 . Strain has been used extensively in recent years to study the Lifshitz transition in Sr_2RuO_4 and to enhance superconductivity [62, 46, 48, 63, 49, 47, 51]. We emphasize, however, that the magnitude of uniaxial strain that we employ is not sufficient to induce a Lifshitz transition (estimated in Ref. [62] to be $\varepsilon_{xx} - \varepsilon_{yy} \approx 0.7\%$), and moreover the epitaxial strain is biaxially compressive (-0.1% in the a direction and -0.4% in the b direction at low temperatures) relative to bulk Sr_2RuO_4 [64, 65], which is known to move the Fermi level *away* from the van Hove singularity rather than towards it [46]. Thus, the effects that we measure are due to a relatively weak uniaxial perturbation of the electronic structure and are not expected to be driven by density of states enhancements or changes in band topology.

We first examine the static reflectivity anisotropy, defined as the ratio of reflectivity for light polarized along the a-axis to that along the b-axis. The static optical reflectivity at 800 nm was measured at normal incidence using a linearly polarized probe beam focused to a spot size of ~ 30 μm at the surface of the sample, with negligible fluence. The same probe beam was later used for time-resolved measurements, but for those measurements a larger probe fluence and oblique incidence were employed. A CMOS camera detector continuously measured the reflected intensity as the sample was steadily warmed from ~ 12 K to ~ 300 K over the course of several hours. Throughout the temperature ramp,

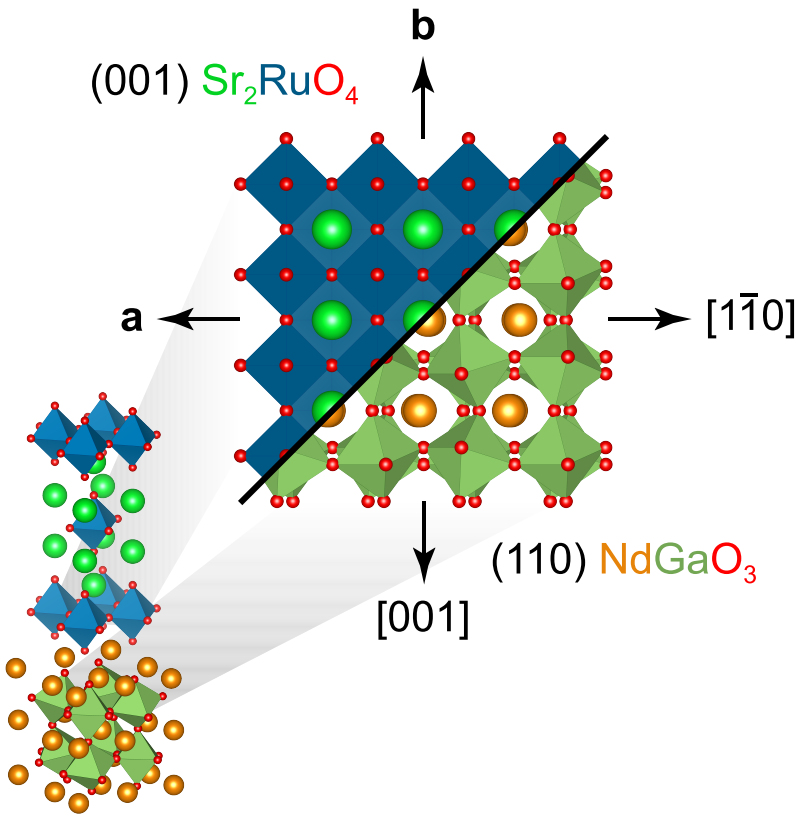

Figure 5.7: Crystallographic directions in the film and substrate. For (001) Sr_2RuO_4 on (110) $NdGaO_3$, the a-axis corresponds to [1$\bar{1}$0] $NdGaO_3$ and the b-axis corresponds to [001] $NdGaO_3$.

the polarization was rapidly switched ($\sim$ 1 Hz) between orientations parallel to the a-axis and the b-axis of the sample by mechanically rotating a polarizer. Taking the ratio of these two signals enabled a measurement robust to low-frequency noise (e.g., laser power fluctuations). Four measurements were collected and averaged for the SRO/NGO sample, and two measurements were averaged for the SRO/LSAT sample.

Figure 5.8 shows the measured anisotropy versus temperature using a probe wavelength of 800 nm, where a striking dichroism is apparent. We find a decrease in reflectivity along the (long) a-axis relative to the (short) b-axis, which becomes more pronounced at lower temperatures. At the lowest temperatures, the maximum reflectivity anisotropy is 1.7%, more than five times larger than the uniaxial strain imposed by the substrate (0.3%). Similar behavior has been observed in detwinned FeSe, where the reflectivity anisotropy was taken as a proxy for the nematic order parameter [55].

To eliminate the possibility that the dichroism is merely due to structural orthorhombicity, we include in the figure the temperature-dependent lattice constant ratio a/b for films strained to $NdGaO_3$. Under the hypothesis that the static dichroism is entirely due to simple $a \neq b$ structural effects, we would expect a linear proportionality with the substrate orthorhombicity as it changes with temperature. To show this, we expand the reflectivity as a power series in the lattice constants: $R_a = R_0 + \alpha\delta a + \ldots$ and $R_b = R_0 + \alpha\delta b + \ldots$, where δa and δb are the small deviations of the a and b lattice constants from perfect tetragonality. The optical reflectivity anisotropy is then given by

$$\frac{R_a}{R_b} - 1 = \frac{R_0 + \alpha\delta a + \ldots}{R_0 + \alpha\delta b + \ldots} - 1 = \frac{\alpha}{R_0}(\delta a - \delta b) + \ldots \tag{5.5}$$

We see that the optical reflectivity anisotropy is linearly proportional to the lattice orthorhombicity $\delta a - \delta b$. The data, however, show a much larger change in the dichroism than the orthorhombicity as temperature is lowered, as shown in Figure 5.8.

Instead, we observe the dichroism grows by an order of magnitude upon cooling, while the substrate orthorhombicity only increases by 30%. As a control, we also measure the reflectivity of Sr_2RuO_4 grown on (001) $(LaAlO_3)_{0.29}$ $(SrTa_{1/2}Al_{1/2}O_3)_{0.71}$ (LSAT), which is tetragonal and induces no uniaxial strain ($a = b$) [66]. In this case, we detect no appreciable dichroism. Our static optical anisotropy measurements suggest that the electronic structure of Sr_2RuO_4 possesses either spontaneous nematic order (scenario I) or a large nematic susceptibility (scenario II). In scenario I, an electronic instability results in the formation of microscopic nematic domains fluctuating in space and time, with one orientation favored by the uniaxial strain over the other. This imbalance induces a net macroscopic anisotropy in the optical response. In scenario II, the weak uniaxial strain drives a strong electronic nematic response via a large nematic susceptibility. Without the strain, however, the electronic structure would retain tetragonal symmetry at all temperatures. Both scenarios are consistent with an absence of dichroism in films grown on LSAT.

5.5 Nematicity in pump-probe response

Now that signatures of electronic nematic order in the optical dichroism have been established, we next turn to measuring the ultrafast response of the order. As we will show,

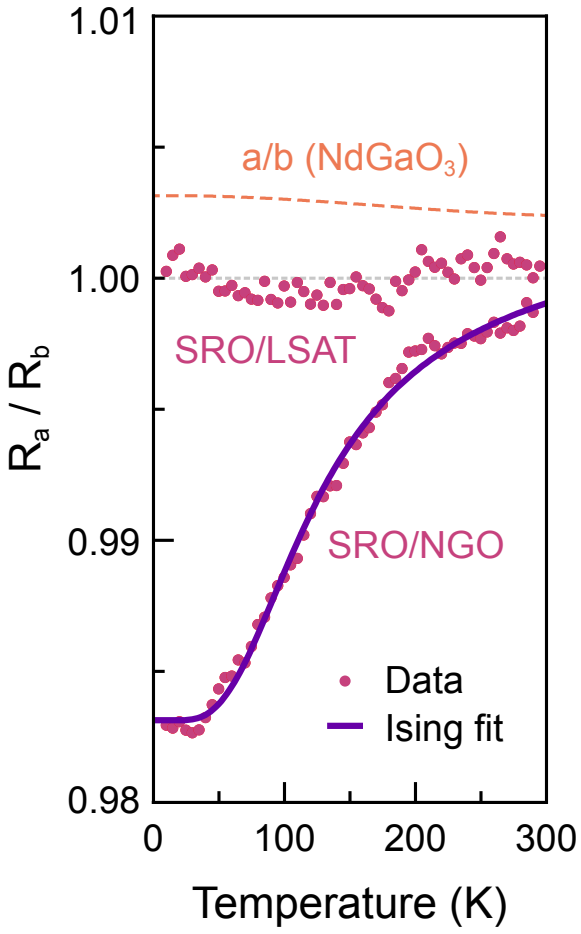

Figure 5.8: Reflectivity anisotropy R_a/R_b versus temperature for films grown on $NdGaO_3$ (SRO/NGO) and LSAT (SRO/LSAT). A fit to an Ising model of nematic order is shown, as well as the lattice constant ratio a/b for films strained to $NdGaO_3$ (from Ref. [61]).

this reveals much larger signatures of nematicity than the static reflectivity and enables the extraction of dynamical information. We use a standard pump-probe transient reflectivity technique to measure changes in the dichroism induced by an ultrafast ($\sim$50 fs) pump pulse of wavelength 760 nm and fluence $\sim$25 μJ/cm^2. Pump pulses were chopped at 500 Hz with a chopper wheel, and the probe signal was measured with a photodiode using a lock-in amplifier. Probe pulses with a center wavelength of 800 nm were used to measure the change in reflectivity after a time delay t controlled by an optical delay stage. To eliminate any possible anisotropy due to the polarization of the pump, we keep the pump and probe pulses fixed in a cross-polarized configuration and rotate the sample about its surface normal (Figure 5.9).

Like the static reflectivity, we uncover a pronounced anisotropy of the transient response. Figure 5.10 shows raw transients of the relative change in reflectivity $\Delta R/R$ versus pump-probe time delay at 12 K for several angles between the a-axis (0°) and the b-axis (90°). A clear breaking of tetragonal symmetry is apparent: for optical polarization parallel to the a-axis, we observe a sharp peak in $\Delta R/R$ that decays over a $\sim$1 ps timescale, whereas for polarization parallel to the b-axis, we observe only a flat step. This nematic ($C_4 \rightarrow C_2$) symmetry breaking can be seen more clearly in a polar plot of the area under the curve (inset). While the static reflectivity shows a modest 1.7% anisotropy, the transient reflectivity anisotropy exceeds 100%. Ultrafast optical anisotropies of this magnitude are routinely observed in the nematic phase of iron-based superconductors [67, 68, 69, 70, 71]. Sub-picosecond timescales are dominated by low-

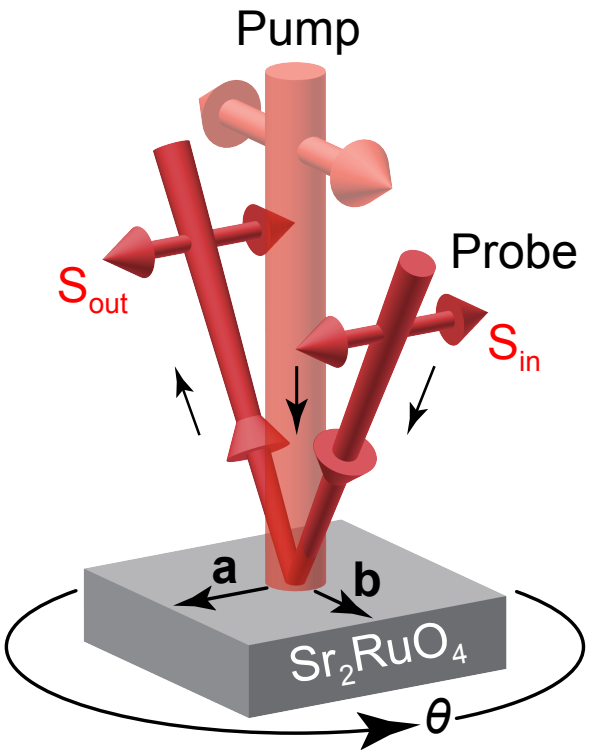

Figure 5.9: Illustration of the pump-probe experimental geometry. The pump and probe beams remain fixed in a cross-polarized configuration while the sample is rotated about its surface normal. $\theta = 0°$ when the probe is polarized along the a-axis (as shown) and $\theta = 90°$ when polarized along the b-axis.

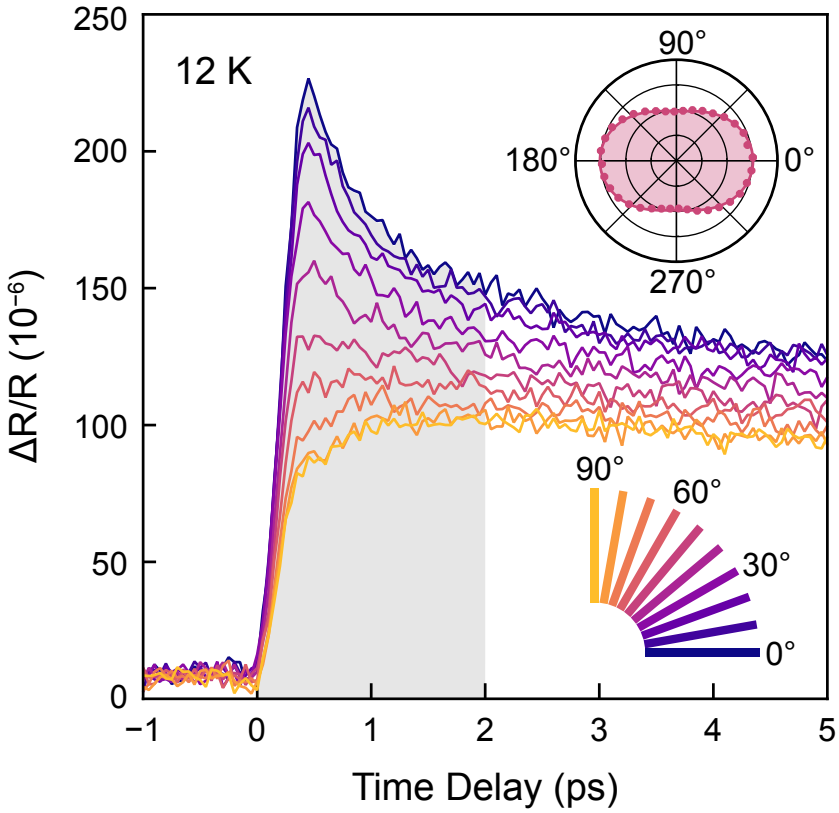

Figure 5.10: Raw transient reflectivity curves for several values of θ at 12 K. A clear anisotropy is observed in the picosecond-scale transient response. The inset shows a polar plot of $\Delta R/R$ integrated from 0 to 2 ps (gray shaded region).

energy electrons, affirming that the dichroism we observe is a result of electronic nematic order rather than structural orthorhombicity.

5.5.1 Nematicity across several relaxation timescales

To probe the low-temperature orientation dependence of the transient reflectivity, samples were cooled using a tabletop optical cryostat to a base temperature of 12 K. For long timescales, the transient reflectivity can be fit to

$$\Delta R(t) = \sum_{i=1}^{3} A_i e^{-t/\tau_i},$$

where the exponential decay terms describe three relaxation processes, each with an amplitude A_i and a characteristic lifetime τ_i. To reveal the nematic symmetry of these relaxation processes, we measured the rotational dependence of the transient reflectivity. As the sample rotates, so too does the orientation θ of the probe polarization with respect to the crystal axes. We emphasize that the pump polarization is always fixed to be orthogonal to the probe, and does not affect the observed nematicity (i.e., the pump polarization does not fix the nematic direction).

Orientation Dependence

Transient reflectivity curves were measured at 12 K and the characteristic amplitudes A_i and lifetimes τ_i were extracted for the three relaxation processes, each of which showed a marked in-plane anisotropy with nematic two-fold rotational symmetry. τ_1 (ranging from 0.4 to 6.5 ps) changes most dramatically with θ, traversing over an order of magni-

tude. This shortest timescale is associated with thermalization of hot electrons, as well as electron-phonon interactions as the electrons begin to transfer energy to the lattice. The longer-lifetime relaxation processes, τ_2 (ranging from 6.4 to 61 ps) and τ_3 (ranging from 184 to 265 ps), also exhibit nematicity. Figure 5.11 is a polar plot of the nematicity observed across all timescales. Figure 5.12(b,d,f) show the same lifetimes τ_i, and Figure 5.12 (a,c,e) show that the two-fold rotational symmetry is also present in the A_i amplitudes, each having a minimum near $\theta = 90°$ (polarization along the b-axis).

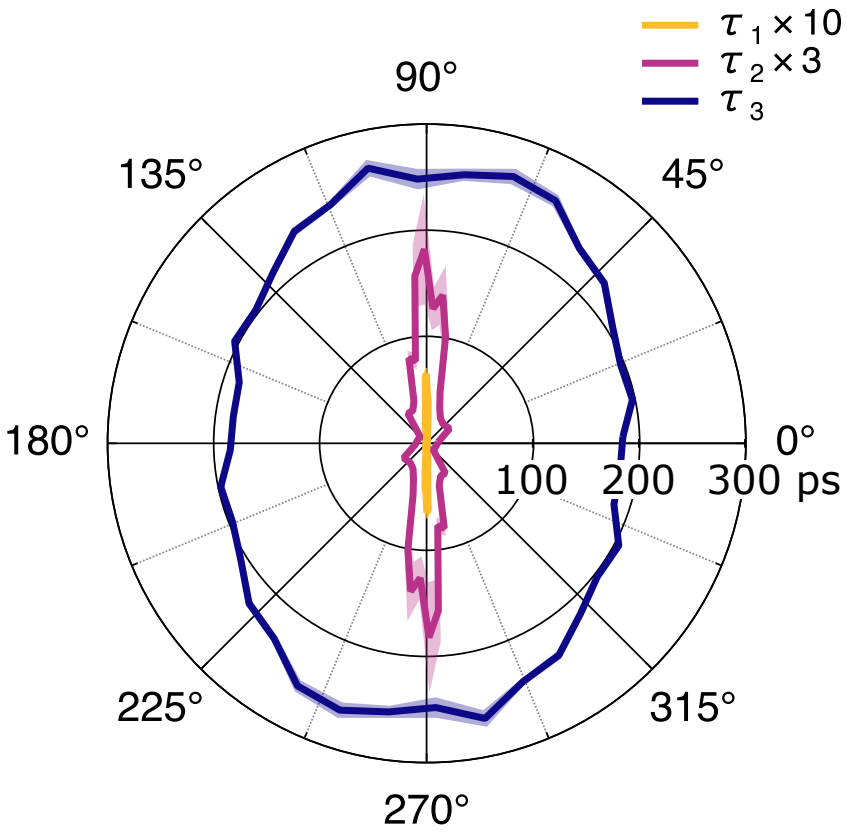

Figure 5.11: Two-fold symmetry with respect to angle θ is observed across all three relaxation lifetimes. $\theta = 0°$ corresponds to a probe polarization oriented along the a-axis. τ_1 exhibits a particularly strong anisotropy, spanning an order of magnitude. Note that τ_1 and τ_2 are scaled by a factor of 10 and 3, respectively. Shaded regions indicate one standard deviation in the extracted lifetime parameters from least-squares fits of the data.

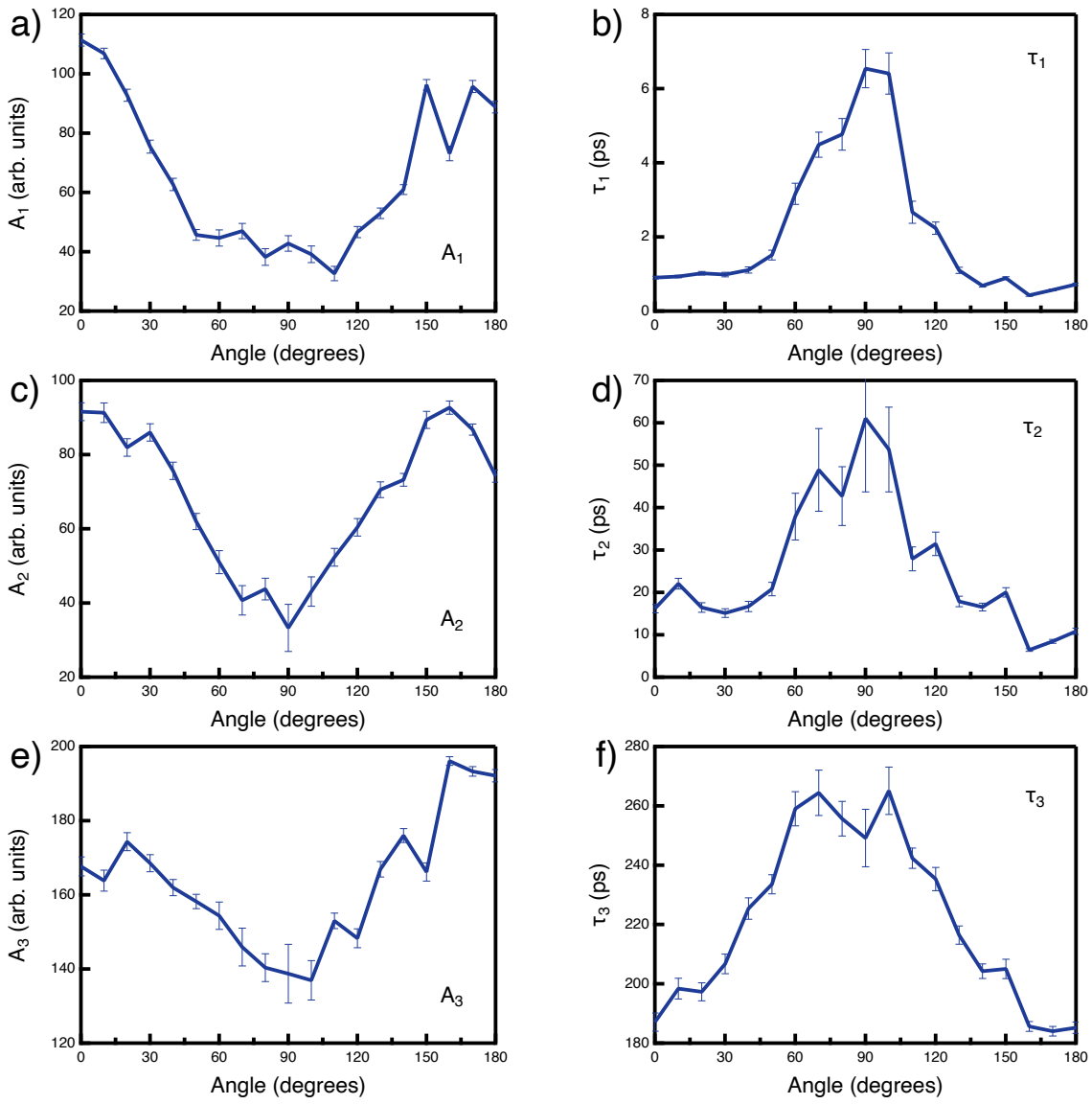

Figure 5.12: Fit parameters as a function of sample orientation angle θ. (a), (c), and (e) show the amplitudes A_i of the equilibration processes, each with a minimum at 90° (along the b-axis). (b), (d), and (e) show the relaxation lifetimes τ_i, each peaked at 90°. Two-fold nematic rotational symmetry is seen in both A_i and τ_i for all three relaxation processes.

Pump Fluence Dependence

We also studied the effects of pump fluence on our measurements. The pump fluence was adjusted via the average pump power (with a fixed laser pulse repetition rate and spot size). We used pump powers ranging from 0.5 to 6 mW, spanning over an order of magnitude (Fig. 5.13).

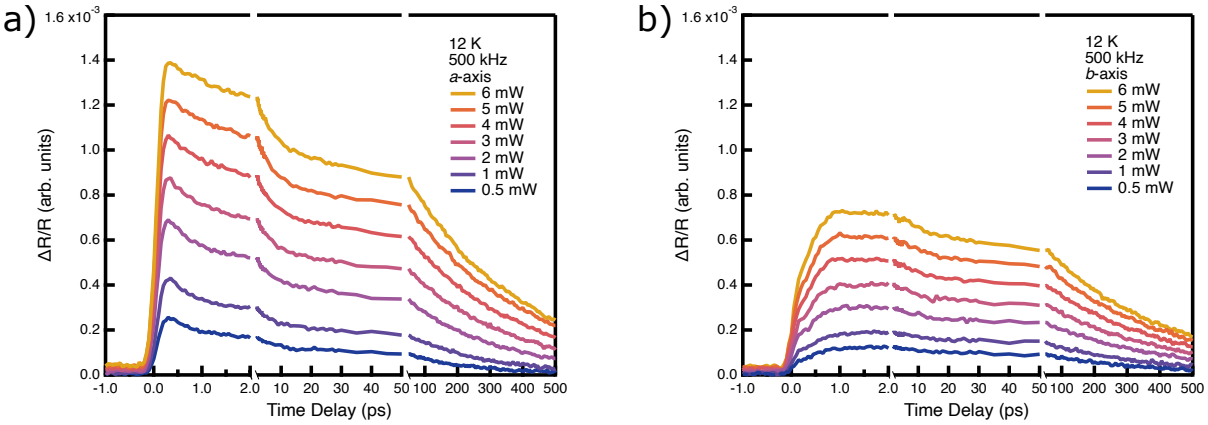

Figure 5.13: Transient reflectivity traces acquired using several selected average pump powers. The magnitude of the transient reflectivity is observed to grow approximately linearly with increasing pump power. (a) Transient reflectivity for $\theta = 0°$ (along the a-axis). (b) Transient reflectivity for $\theta = 90°$ (along the b-axis). Nematicity is observed at all pump powers measured.

We find that $\Delta R/R$ increases approximately linearly with increasing pump fluence up to 6 mW, with slight evidence of saturation at the highest fluence. Two-fold symmetry is retained across the entire time-delay range studied, from 0 to 500 ps. Strikingly, we observe the pump fluence to significantly affect the magnitude of the observed nematicity at short (sub-picosecond) time delays. Figure 5.14 illustrates this difference.

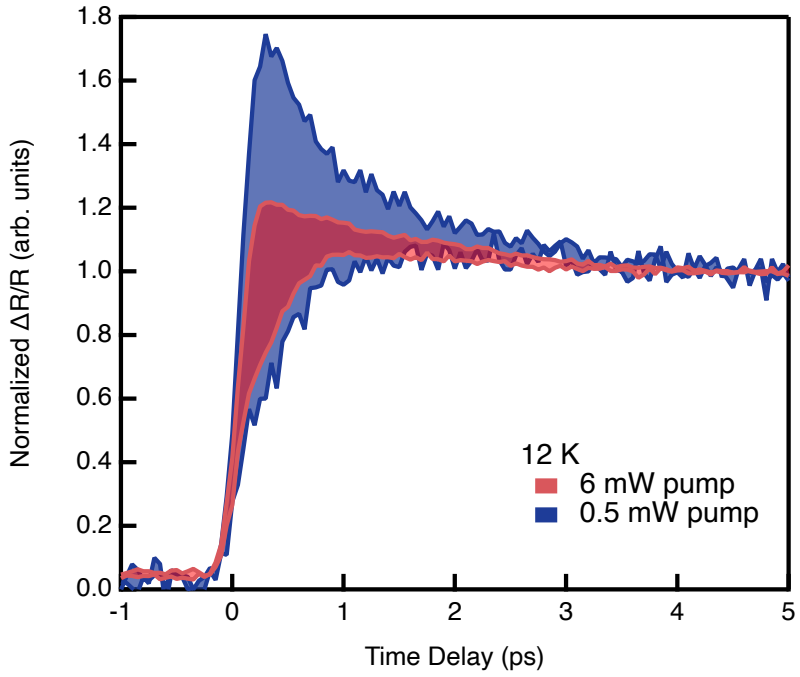

Figure 5.14: Pump power dependence of nematicity at 12 K. Traces are normalized such that $\Delta R/R = 1$ at 5 ps. A larger pump power is seen to suppress nematicity. The shaded area represents the difference in the transient response between $\theta = 0°$ and 90° for the lowest pump fluence (blue) and highest pump fluence (red).

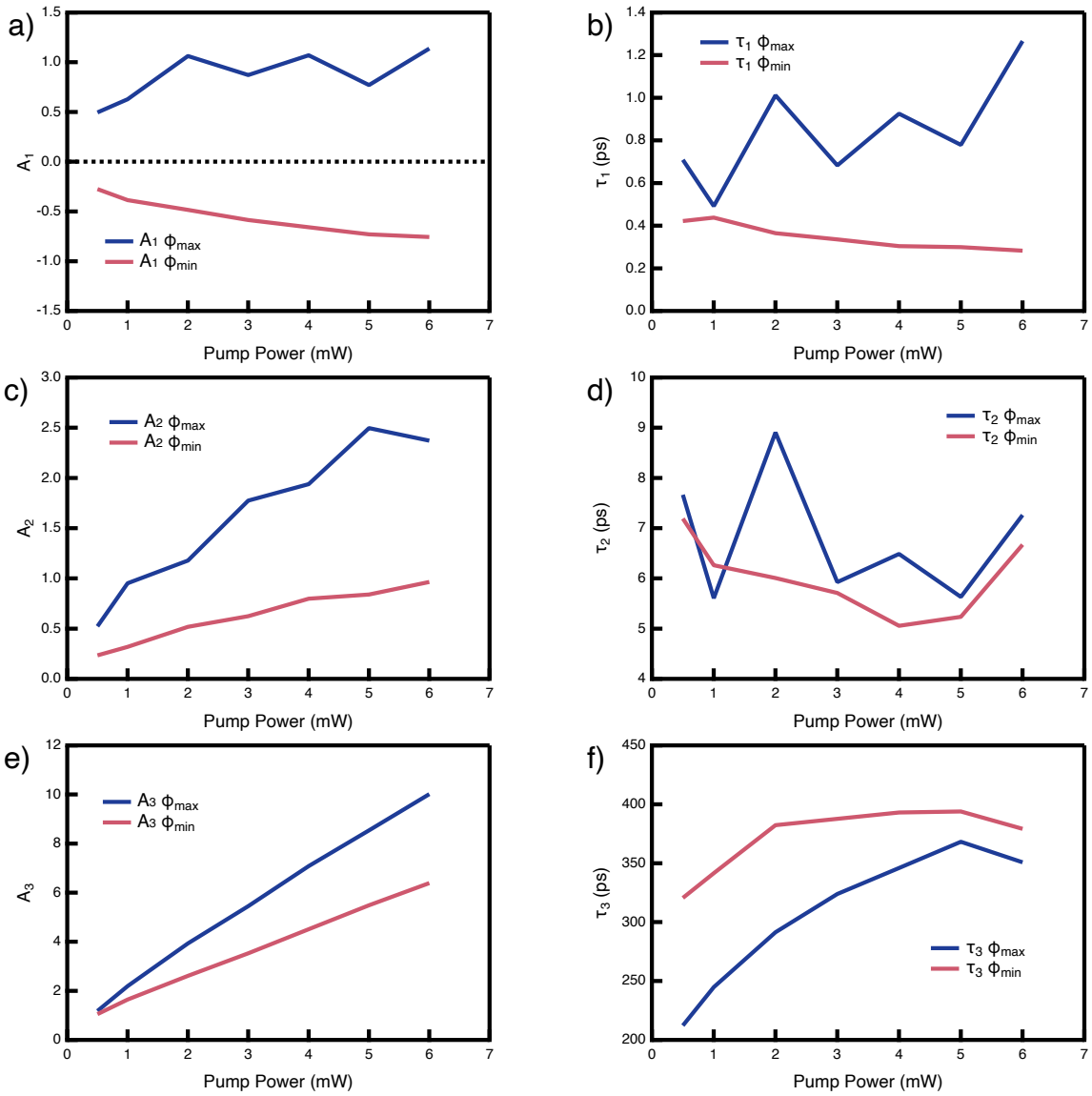

Figure 5.15: Fit parameters of transient reflectivity data as a function of pump fluence. The data are fit well by three equilibration processes, each with characteristic amplitude A and lifetime τ. Amplitudes are shown in 4(a), (c), and (e). Lifetimes are shown in 4(b), (d), and (f). Pump power has a greater impact on longer lifetime processes.

5.5.2 Ising model of the static dichroism

A saturation at low temperatures is evident in the static dichroism [Fig. 5.8], resembling an Ising-like order parameter. To quantitatively analyze the data, we therefore develop a heuristic mean-field Ising model of the nematic order, which can describe both scenarios discussed above. Within the model, we define an order parameter ϕ that takes the values $+1$ or -1, corresponding to a nematic director oriented along the a- or b-axis, respectively. The Hamiltonian is

$$\mathcal{H} = -\frac{1}{2}\sum_{i,j} U(\mathbf{r}_i - \mathbf{r}_j)\phi_i\phi_j - F\sum_i \phi_i,$$

where i and j label unit cells, $U(\mathbf{r})$ is the interaction energy (related to the stiffness of the nematic order), and F is the uniaxial strain field, which favors $+1$ domains over -1 domains. Within mean-field theory, the average order parameter $\langle\phi\rangle$ satisfies the self-consistency equation

$$\langle\phi\rangle = \tanh\left(\frac{U\langle\phi\rangle + F}{k_B T}\right),$$

where $U = \sum_i U(\mathbf{r}_i)/2 = k_B T_c$ defines the critical temperature of the nematic phase transition. We assume the measured optical anisotropy is proportional to the order parameter ($R_a/R_b - 1 \propto \langle\phi\rangle$) and fit the data to this functional form. The least-squares fit, included in Fig. 5.8, yields the parameters $U = 53 \pm 8$ K and $F = 53 \pm 7$ K. Excellent agreement with the data is achieved despite the relative simplicity of our model. Taking it at face value, the model predicts a critical temperature of $T_c \approx 50$ K, where global nematic order spontaneously condenses following scenario I. In reality, this transition

is spread over a wide temperature range due to the large magnitude of the symmetry-breaking uniaxial strain field. Scenario II, where nematic order does not occur without strain, would require $U \leq 0$, which is not consistent with our data. Based on the success of this simple Ising nematic model, we will continue to use it to quantitatively analyze the data.

5.5.3 Pump-induced temperature change

Figure 5.16(a) shows measurements at several temperatures between 12 K and 300 K for polarization along the a-axis (R_a) and b-axis (R_b). To isolate temperature-dependent changes in the anisotropy from other effects, we also show the difference ($R_a - R_b$) and sum ($R_a + R_b$). We see that the sharp peak in $\Delta R/R$ is entirely due to the nematicity of the material, while the flat step after time-zero represents the isotropic component of the optical response. Moreover, while the isotropic response monotonically decreases with increasing temperature (Fig. 5.17 (left)), we uncover an unusual non-monotonic temperature dependence of the nematic component of the response [Fig. 5.17 (right)]. The isotropic transient response is likely caused by an increase in temperature ΔT after absorption of the pump.

The transient reflectivity data were obtained using a pump fluence of ~ 25 μJ/cm^2 (0.5 mW average chopped power at a repetition rate of 500 kHz over a spot size of diameter ~ 100 μm). We seek to calculate the energy deposited per formula unit under such a fluence. We assume the pump is absorbed following Beer's law, $I(z) = I_0 e^{-\alpha z}$,

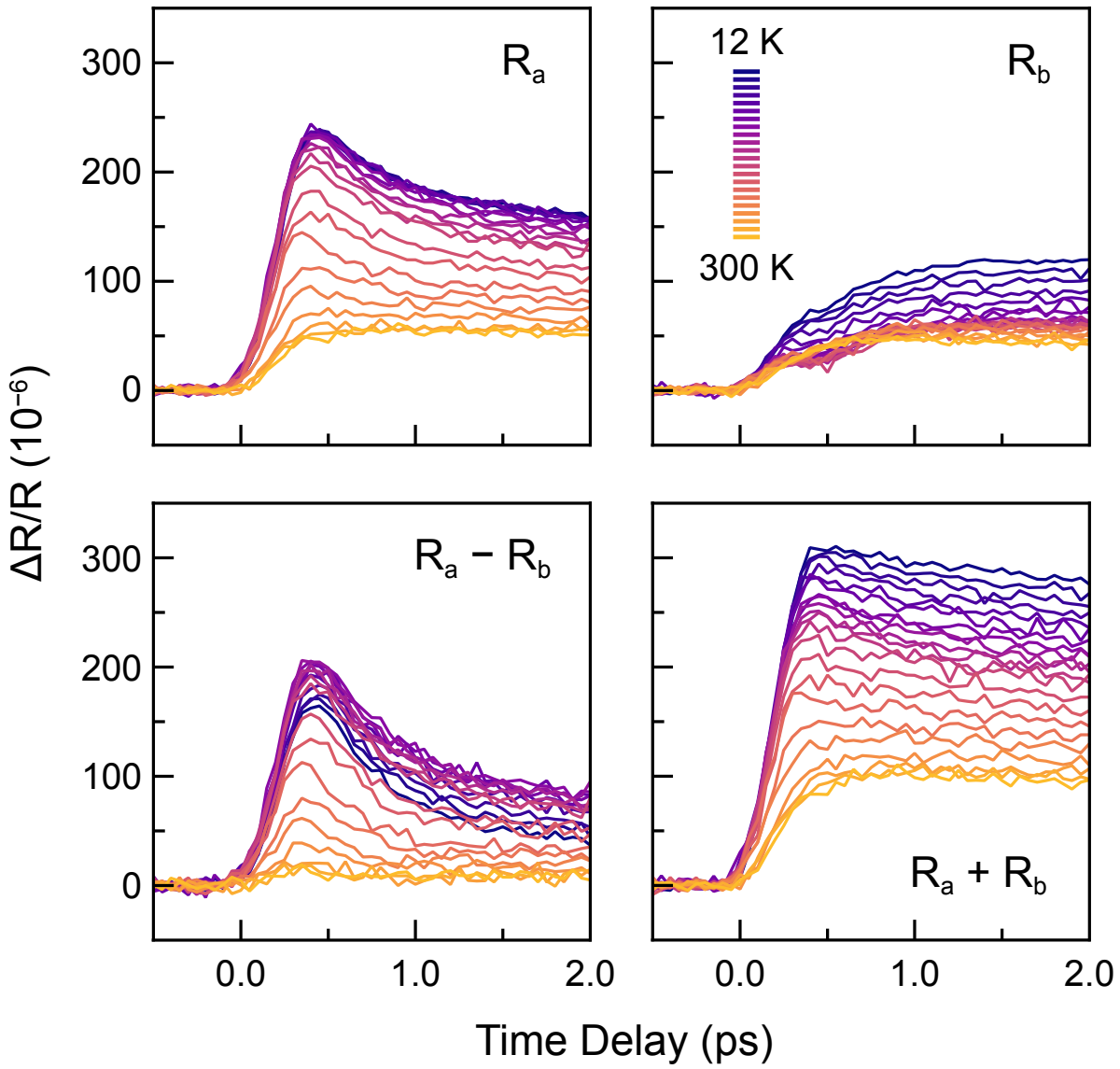

Figure 5.16: $\Delta R/R$ for selected temperatures between 12 K and 300 K for polarization along the a-axis (upper left), b-axis (upper right), their difference (lower left), and their sum (lower right).

with an absorption coefficient given by $\alpha = \frac{4\pi\kappa}{\lambda}$. From Ref. [41], we determine the index of refraction of Sr_2RuO_4 at 800 nm to be $n + i\kappa = 1.2 + 0.98i$, from which we calculate an absorption length $\alpha^{-1} = 65$nm. Using the Fresnel equations, we also calculate the surface reflection loss for S-polarized light with angle of incidence 12° to be $R = 0.18$. The in-plane area of one unit cell of Sr_2RuO_4 is $a^2 = (3.86\text{Å})^2$ and the RuO_2 planes are separated by a distance $c/2 = 6.36$Å. A naive calculation of the energy deposited per formula unit yields

$$\Delta E_0 = \frac{25\mu\text{J/cm}^2 \times (3.86\text{Å})^2 \times 6.36\text{Å} \times (1 - 0.18)}{65\text{nm}} = 1.87 \text{ meV}. \tag{5.6}$$

A more careful analysis, however, shows that a factor of 2/3 is needed to correct this value. This arises from the fact that the intensity of the pump decays exponentially with depth below the surface of the sample. We are measuring a property, the pump-induced change in reflectivity ΔR, that depends functionally on the deposited energy at different depths: $\Delta R(\Delta E_0 e^{-\alpha z})$. The probe beam, measuring this property at a specific depth z, must travel a total distance $2z$ within the material, through which its intensity also decays. Integrating over all depths, the average signal that is measured in the experiment is

$$\frac{\int_0^\infty \Delta R(\Delta E_0 e^{-\alpha z}) e^{-2\alpha z} dz}{\int_0^\infty e^{-2\alpha z} dz} = 2\int_0^1 \Delta R(\Delta E_0 x) x dx. \tag{5.7}$$

We make the additional assumption, verified experimentally, that ΔR is linearly proportional to pump intensity. Thus, $\Delta R(\Delta E_0 x) = \Delta R(\Delta E_0)x$, from which we find

$$\frac{\int_0^{1/2} x^2 dx}{\int_0^1 2\Delta R(\Delta E_0) dx} = 3\Delta R(\Delta E_0) = \Delta R\left(\frac{2}{3} \times \Delta E_0\right). \tag{5.8}$$

The net result is that the measured change in reflectivity ΔR_{avg} corresponds to the change in reflectivity calculated for a pump with 2/3 the incident intensity. Thus, we use $\Delta E = \frac{2}{3} \times \Delta E_0 = 1.25\text{meV}$. An electronic heat capacity $C(T) = \gamma T$ corresponds to an internal energy $U(T) = \frac{\gamma T^2}{2}$. Applying conservation of energy, we find $U(T_{\text{initial}}) + \Delta E = U(T_{\text{final}})$, whose solution is $T_{\text{final}} = \sqrt{T^2 + \frac{2\Delta E}{\gamma}}$. Finally, we set $\Delta T_{\text{max}} = T_{\text{final}} - T_{\text{initial}}$. Using the initial electronic heat capacity coefficient $\gamma = 3.88 \times 10^{-4}\text{meV}/K^2$ reported in Ref. [72], we find $\left(\frac{2\Delta E}{\gamma}\right) \approx (80K)^2$.

A function of the form $g(T) = \alpha + \beta \Delta T_{\text{max}}(T)$ fits the isotropic component extremely well [gray line in Fig. 5.17]. We use this fact to scale the data at each temperature to match $g(T)$ and correct for laser fluctuations during the experiment, where, for example, the two data points near $\sim$35 K are otherwise anomalously low. This normalization procedure is used for the remainder of our analysis.

Figure 5.8 shows that the onset of nematic order reduces the optical reflectivity along the a-axis. After the pump pulse, this reflectivity increases. It follows that the effect of the pump is to suppress the nematic order, likely through a transient increase in temperature. To model this, we assume the dichroism is proportional to the nematic order parameter ϕ. The measured change in dichroism is therefore proportional to the change in ϕ:

$$\Delta(R_a - R_b)/R \propto (1 + \delta)\phi(T + \Delta T) - \phi(T),$$

where $\phi(T)$ is the equilibrium value of the order parameter at the measurement temperature T, ΔT is the increase in electronic temperature after absorption of the pump energy,

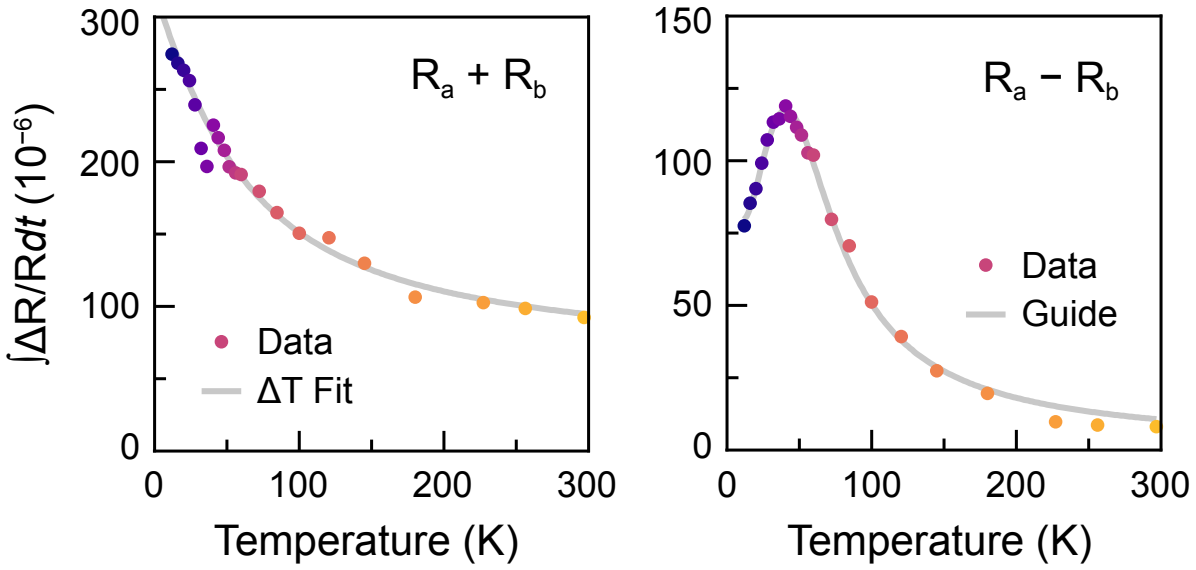

Figure 5.17: (Left) Temperature dependence of the average value of $\Delta(R_a + R_b)/R$ between 1.5 and 2 ps, representing the isotropic component of the transient response. The response monotonically decreases with increasing temperature. The gray line is a fit to the sample temperature change. (Right) Temperature dependence of the average value of $\Delta(R_a - R_b)/R$ between 0 and 2 ps, representing the nematic component of the transient response. An unusual non-monotonic behavior is observed.

and $\delta < 0$ represents a non-thermal suppression of the order parameter amplitude by the pump pulse. The previously developed Ising model provides an expression for $\phi(T)$. The temperature increase ΔT is not necessarily instantaneous. Instead, we allow the temperature of the electrons to rise to some time-dependent fraction $0 \leq f(t) \leq 1$ of $\Delta T_{\max}$ $[\Delta T(t) = f(t)\Delta T_{\max}]$. With this model, we fit the transient optical data at all time delays and all temperatures simultaneously. The fit includes three global parameters (U, F, and a fixed scaling factor) and two time-dependent parameters [$\delta(t)$ and $f(t)$]. The results of the fit, shown in Fig. 5.19(a), are excellent ($R^2 = 0.994$).

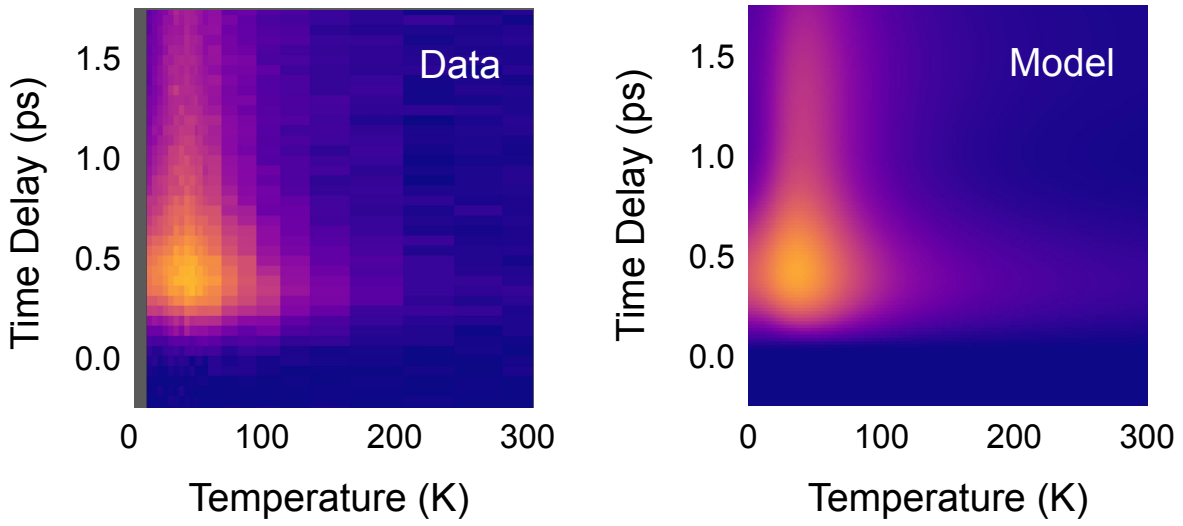

Figure 5.18: (Left) Two-dimensional joint time delay and temperature dependence of $\Delta(R_a - R_b)/R$. (Right) Corresponding depiction generated by fitting to the Ising nematic model.

A number of salient points are uncovered by the fit: **(1)** The non-monotonic temperature dependence of the dichroism (Fig. 5.17 (right)) is a result of the flattening of the nematic order parameter at low temperatures ($d\phi/dT \to 0$ as $T \to 0$), which reduces the effect of pump heating. **(2)** Uncertainties in the fit parameters U and F are correlated,

which is a result of their coupled influence on $\phi(T)$. The F-test-derived confidence regions displayed in Fig. 5.19(c), however, show that $U > 0$ with high confidence. Within the applicability of the model, this implies that the nematic order we observe is spontaneous (scenario I). **(3)** While we extract a value for F similar to that of the static measurement (46 K versus 53 K), the value of U is smaller (23 K versus 53 K). We conjecture that repeatedly exciting the sample with high-fluence optical pulses does not allow it to completely return to equilibrium, causing a net suppression of the order parameter. This subsequently renormalizes the average interaction energy U. **(4)** Figure 5.19(c) shows that the nematic electron temperature rises to ∼50% of the maximum calculated increase ΔT_{max} within ∼0.6 ps. This shows that the pump energy is first absorbed by background electrons during the pulse (∼50 fs) and then quickly transferred to the nematic electrons via thermal equilibration mediated by electron–electron interactions. At a much slower rate dictated by electron–phonon interactions, thermal equilibration with the lattice commences, causing a gradual cooling. To make this picture more quantitative, we fit $f(t)$ to the heat equation $df/dt = k(f_0 - f)$, where $f_0(t) = e^{-t/\tau}$ represents the background electronic temperature, with lattice equilibration timescale τ. We find excellent agreement with the data for $\tau = 0.82$ ps. **(5)** The non-thermal suppression of the order parameter after the pump pulse [Fig. 5.19(d)] reveals a coherent oscillation, which can be understood with a damped harmonic oscillator model: $d^2\delta/dt^2 + 2\gamma d\delta/dt + \omega_0^2(\delta - \delta_0) = 0$, where γ is the damping rate, ω_0 is the natural frequency, and δ_0 is the pump-induced displacement of the order parameter amplitude. A solution to this equation fits the data

well if $\delta_0(t) = \alpha e^{-t/\tau} + \beta$, representing a sharp impulsive suppression at $t = 0$ followed by a rapid recovery ($\tau = 0.09$ ps) to a displaced equilibrium amplitude $\beta = -5.0\%$ relative to the initial value [gray curve in Fig. 5.19(d)]. We extract a frequency $\omega_0/2\pi = 0.89$ THz for the nematic amplitude mode.

5.6 Microscopics: the Emery model

The foregoing optical dichroism experiments suggest that Sr_2RuO_4 supports a high-temperature Ising-like nematic order parameter with an order-disorder phase transition below ∼50 K. To put forth a possible microscopic origin for this order, we turn to the Emery model, first used to describe hole doping of CuO_2 planes in cuprate superconductors away from half filling [73]. Here, we use the model to study intra-unit-cell nematic order in RuO_2 planes with fillings adjacent to the van Hove singularity of the γ band [74]. Our mean-field analysis closely follows Ref. [75], with details provided below. Figure 5.20(a) shows the hopping and interaction parameters defined within the model, and Fig. 5.20(b) shows the resulting band structure. Of central importance are the Coulomb repulsion between neighboring oxygen p-orbitals (V_{pp}), which favors a nematic charge order $\eta = n_{p_x} - n_{p_y}$ with different electron densities on the p_x and p_y orbitals, and the van Hove singularity of the γ band at the X point, which leads to a diverging density of states that supports electronic instabilities by reducing the energy cost to redistribute orbital density. Figure 5.20(c) shows the mean-field ground state phase diagram as a function of V_{pp} and filling. A nematic phase is stabilized for sufficiently large values of V_{pp} that

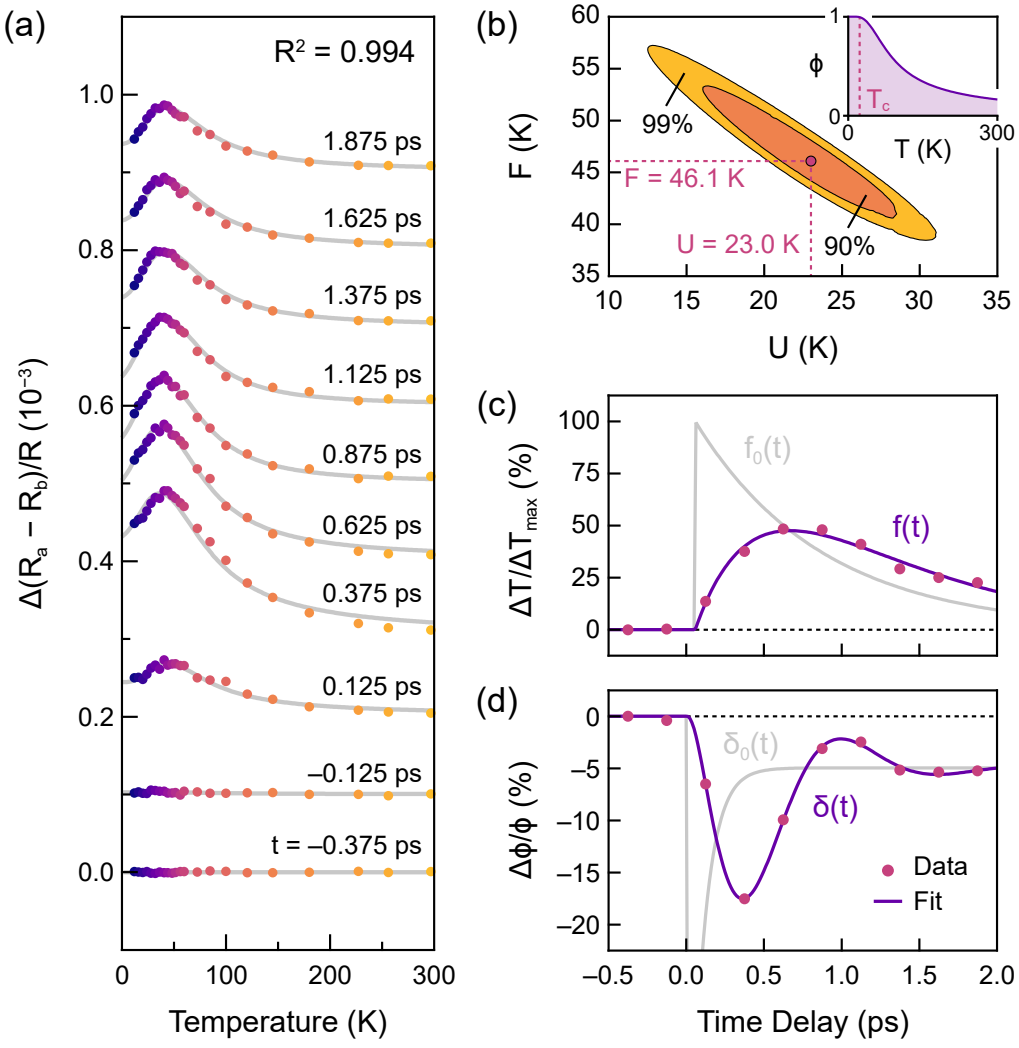

Figure 5.19: Ising model fit of optical anisotropy. (a) $\Delta(R_a - R_b)/R$ versus temperature for selected time delays after the pump pulse. Curves are offset by 10^{-4}. Gray lines show the global fit to the Ising nematic model, as described in the text. (b) Confidence regions for the Ising parameters U and F computed through an F-test. $U > 0$ with greater than 99% confidence, implying the existence of spontaneous nematic order. The inset shows the order parameter $\phi(T)$ together with the critical temperature T_c for spontaneous nematic order when $F = 0$. (c) Electronic temperature increase versus time delay as a fraction of the calculated maximum increase. Also shown is a fit to the solution of the heat equation $df/dt = k(f_0 - f)$ (purple curve) with background electronic temperature f_0 (gray curve). (d) Relative suppression of the nematic order versus time delay, showing a coherent oscillation of the order parameter amplitude. Also shown is a fit to a damped harmonic oscillator (purple curve) with a pump-induced displacement of the equilibrium amplitude (gray curve).

depend on the proximity to the van Hove filling. Bulk Sr_2RuO_4 has $n - n_{vH} \approx -0.2$ [74], which requires an interaction strength $V_{pp} > 1.7$ eV to stabilize nematic order. The full temperature–filling phase diagram is displayed in Fig. 5.20(d), where it is seen that such order, if it exists, condenses well above room temperature. The model shows that Sr_2RuO_4 is exceptionally close to a nematic instability, and offers a plausible microscopic picture of an Ising-like ($\eta = \pm\eta_0$) nematic charge order. We conjecture that at high temperatures this nematicity is spatially disordered at the nanoscale, but shows an order-disorder phase transition to a globally nematic state at lower temperatures.

To develop this model, we performed a mean-field analysis of the Emery model of the RuO_2 plane, closely following Ref. [75]. Instead of duplicating their detailed analysis, however, here we simply identify the principal differences. First, because we are interested in Ru d_{xy} orbitals (instead of Cu $d_{x^2-y^2}$ orbitals relevant to CuO_2 planes), the kinetic energy part of the Hamiltonian (associated with hopping between the transition metal d-orbital and oxygen p-orbitals) is different. Second, because we are only interested in phase boundaries, we ignore other interaction parameters (namely, U_d and V_{pd}) that do not change the boundary locations. We define a 1000×1000 square grid of k-points, and at each point numerically diagonalize the Hamiltonian matrix, where

$$H_k = \begin{pmatrix} \xi_x & \gamma_2(k) & \gamma_1(k_x) \\ \gamma_2(k) & \xi_y & \gamma_1(k_y) \\ \gamma_1(k_x) & \gamma_1(k_y) & \xi_d \end{pmatrix}, \tag{5.9}$$

$$\gamma_1(k_i) = -2t_{pd} \sin\left(\frac{ki}{2}\right), \tag{5.10}$$

$$\gamma_2(k) = -4t_{pp} \sin\left(\frac{k_x}{2}\right) \sin\left(\frac{k_y}{2}\right), \tag{5.11}$$

$$\xi_x = -(2V_{pp} - U_p/4)\eta - \mu, \tag{5.12}$$

$$\xi_y = +(2V_{pp} - U_p/4)\eta - \mu, \tag{5.13}$$

$$\xi_d = \Delta - \mu, \tag{5.14}$$

with all hopping and interaction parameters defined as in Fig. 5.20(a). Band filling (relative to the van Hove singularity) is implicitly controlled through the chemical potential μ. Following Ref. [76], we take $t_{pd} = 1.5$ eV, $t_{pp} = 0.4$ eV, and $U_p = 4.4$ eV. Δ is the charge-transfer energy, which we take to be 0.5 eV to best match the density-functional theory calculated band structure of Sr_2RuO_4 (e.g., Fig. 1 of Ref. [77]). Our results, however, are insensitive to the exact values of these parameters. $\eta = (n_{px\uparrow} + n_{px\downarrow}) - (n_{py\uparrow} + n_{py\downarrow})$ is the nematic charge order parameter, which is finite when there is unequal occupation of the p_x and p_y orbitals. We define the grand potential per unit cell

$$\omega = -2k_BT \sum_{\alpha,k} \ln[1 + \exp(-\xi_{\alpha,k}/k_BT)] + (V_{pp} - U_p/8)\eta^2, \tag{5.15}$$

where $\xi_{\alpha,k}$ are the eigenvalues of the matrix H_k. To find the phase boundaries, we set $\frac{\partial^2\omega}{\partial\eta^2}\Big|_{\eta=0} = 0$ and solve this equation for V_{pp} at each temperature and band filling. These phase boundaries are shown in Fig. 5.20(c) and (d). Our results are very similar to those of Ref. [75], with the major difference being a shift and reversal of direction of the filling axis.

In conclusion, optical dichroism measurements of epitaxially strained thin films strongly support the existence of electronic nematic order in Sr_2RuO_4. By fitting our data to a simple Ising model, we conjecture that this order emerges spontaneously at low temperatures through an order-disorder transition, rather than through a large nematic susceptibility. We present a microscopic model of intra-unit-cell nematic order based on the Emery model [73], showing that Sr_2RuO_4 is exceptionally close to a nematic instability. We hypothesize that at high temperatures this nematicity is spatially disordered at the nanoscale, but shows an order-disorder phase transition to a globally nematic state at lower temperatures. Our results corroborate the angle-resolved transverse resistivity measurements that first uncovered electronic nematicity in Sr_2RuO_4 [52]. While electrical transport and optical reflectivity are disparate probes operating at different energy scales, they both show clear signatures of two-fold electronic anisotropy. Furthermore, although transport can be sensitive to non-local effects such as defect scattering, especially in a material with ostensible microscopic nematic domains, optical reflectivity is a local, bulk-sensitive probe. Our findings also offer a new perspective on the Fermi liquid crossover at $T_{\mathrm{FL}} \sim 40$ K observed by Hall transport [38, 39, 40], optical spectroscopy [41],

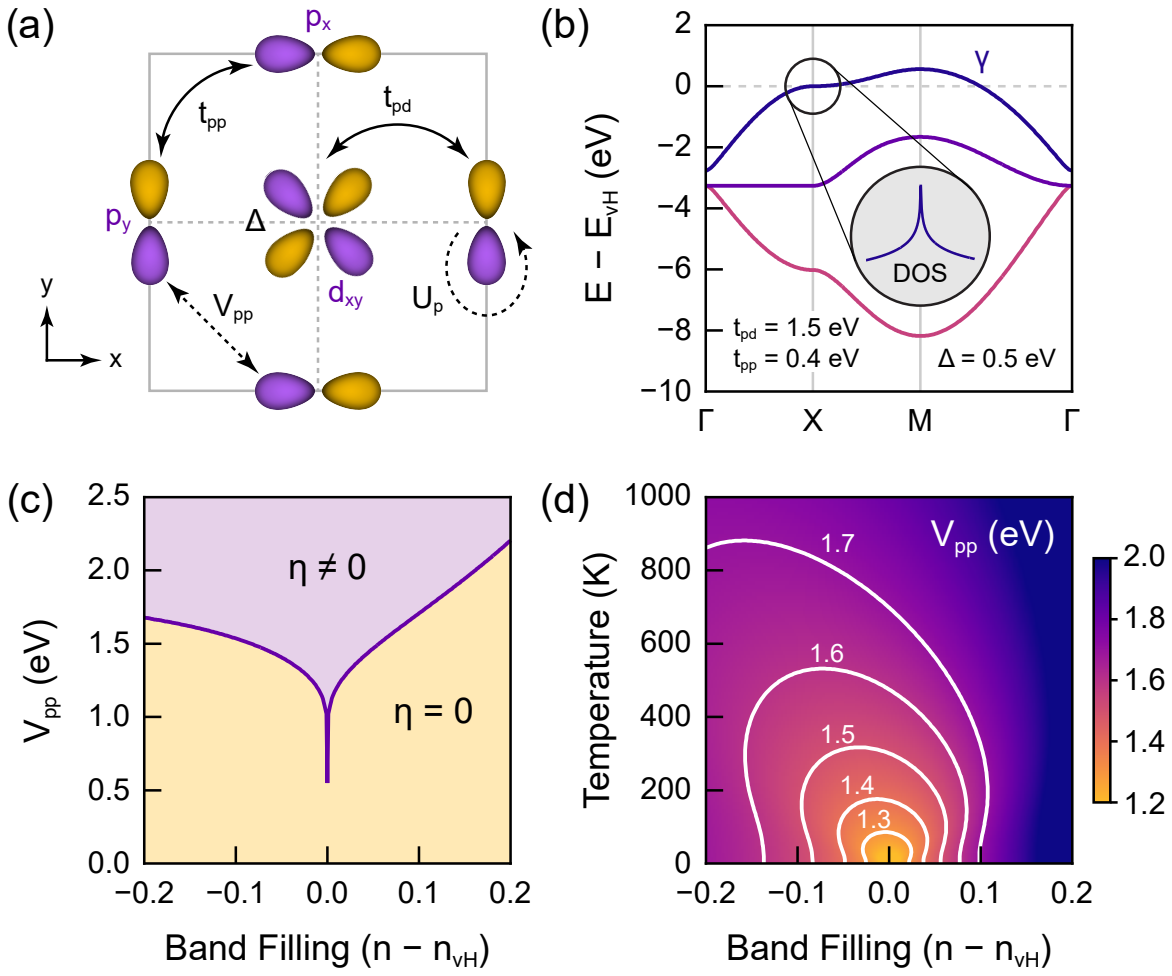

Figure 5.20: Microscopic model of nematic order in Sr_2RuO_4. (a) Unit cell of the RuO_2 plane showing the three-orbital basis (Ru d_{xy} and O p_x and p_y) of the Emery model. Hopping integrals (solid lines) and interaction parameters (dashed lines) are defined following Ref. [75]. (b) Resulting tight-binding band structure, with parameters taken from Ref. [76]. (c) Interaction–filling phase diagram showing the critical value of V_{pp} necessary to produce a nematic ground state ($\eta \neq 0$). (d) Temperature– filling phase diagram for different values of V_{pp}. Panels (c) and (d) were calculated for $U_p = 4.4$ eV [[76]].

and nuclear magnetic resonance [42, 43]. We speculate that the crossover is directly related to nematicity, which appears to develop at the same temperature. Indeed, such a Fermi liquid crossover has been theoretically shown to emerge in the vicinity of an Ising nematic quantum critical point [78, 79, 80]. Nematic order also offers a natural explanation for the checkerboard charge order observed at the surface of Sr_2RuO_4 by scanning tunneling microscopy [53]. An important open question is to what extent electronic nematic order in the normal state of Sr_2RuO_4 influences the likelihood of different forms of superconductivity at lower temperatures. Future experimental and theoretical work is necessary to address this principal question.

Chapter 6

Ferroelectricity in thin films of $SrTiO_3$

Despite its long history and contemporary interest, the superconducting phase of $SrTiO_3$ is still not well understood [81]. A central open question is how the superconductivity emerges from an exceptionally dilute Fermi gas. In this regime, the Fermi energy is less than the Debye frequency, making conventional Bardeen-Cooper-Schrieffer (BCS) and Migdal-Eliashberg theories of acoustic phonon mediated electron pairing inapplicable [82]. It has become increasingly clear that an unconventional pairing mechanism is responsible for superconductivity in $SrTiO_3$. Given the proximity of the material to a polar instability, fluctuations of ferroelectric order are an obvious candidate [83, 84, 85]. Ferroelectricity and superconductivity, however, have a precarious relationship. Superconductivity requires free carriers, with the superconducting energy gap depending strongly on

the density of states at the Fermi level, while free charges tend to rapidly screen electric dipole fields and prevent long-range spontaneous electric polarization. Indeed, only recently have long-sought examples of so-called "polar metals" been discovered [86, 87, 88]. Because of this discordance, the fundamental relationship between ferroelectricity and superconductivity in $SrTiO_3$ is still a matter of debate.

6.1 Methods

Unless otherwise noted, the optical SHG measurements in the studies described below are carried out as follows: Experiments were performed using an ultrafast laser supplying 40 fs pulses at a 10 kHz repetition rate and a center wavelength of 800 nm. The laser spot size was 30 μm and the fluence was below 20 mJ/cm^2. Temperature-dependent longitudinal and Hall resistance measurements were performed using a Quantum Design Physical Property Measurement System. Hall measurements at 300 K were used to determine bulk carrier densities n_{3D}. For SHG-RA measurements, the angle of the scattering plane ϕ is rotated through 360° to collect rotational anisotropy patterns at every temperature point. The dependence of SHG on light polarization was determined using both in-plane ($S_{in/out}$) and out-of-plane ($P_{in/out}$) polarization geometries for the incident and outgoing beams.

6.2 Ferroelectric enhancement of superconductivity in compressively strained $SrTiO_3$ films

The putative link between superconductivity and ferroelectricity has in recent years motivated studies of the effects of enhanced ferroelectric fluctuations on the superconducting properties of $SrTiO_3$. Experiments have reported a modest increase in the superconducting critical temperature T_c by tuning the material towards a ferroelectric ground state using oxygen isotope substitution [89] and alloying with calcium [90]. In thin films, epitaxial strain is also known to stabilize ferroelectricity [91, 92, 93, 94], and a striking recent study has shown that in-plane compressive strain can enhance the superconducting critical temperature by up to a factor of two [95]. To establish a clear link between this superconducting enhancement and ferroelectricity, here we directly measure the ferroelectric order parameter of compressively strained films of electron-doped $SrTiO_3$ [96]. The metallic nature of these films precludes traditional electrical methods for measuring polarization. Optical second harmonic generation (SHG), on the other hand, is an all-optical technique that is acutely sensitive to inversion symmetry breaking, making it an ideal and sensitive probe of polar order [5].

Samarium-doped $SrTiO_3$ films of thickness 200 nm were grown epitaxially on (001) LSAT substrates via hybrid molecular beam epitaxy. Sm^{3+} substitutes for Sr^{2+}, resulting in controlled electron doping of the films. Static in-plane compressive strain was produced by a 1% lattice mismatch between bulk $SrTiO_3$ and the substrate.

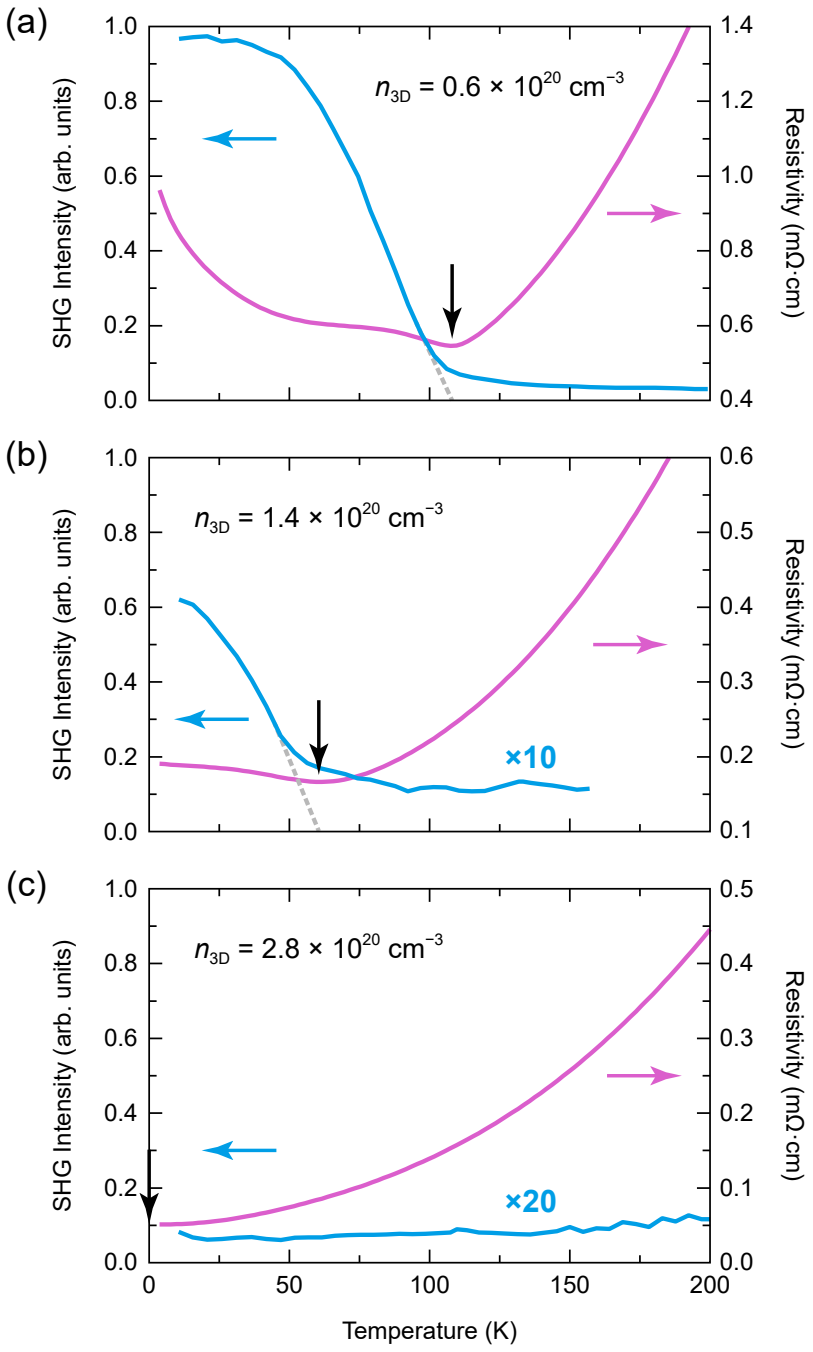

Figure 6.1: Correlation between the onset of ferroelectricity and resistivity anomalies. Temperature dependence of SHG intensity (left axis) and electrical resistivity (right axis) for films with bulk carrier densities of (a) $n_{3D} = 0.6\times10^{20}$ cm^{-3}, (b) $n_{3D} = 1.4\times10^{20}$ cm^{-3}, and (c) $n_{3D} = 2.8 \times 10^{20}$ cm^{-3}. Black arrows mark local minima in the resistivity, which correlate with the onset temperatures of the ferroelectric order parameter.

Fig. 6.1 compares the temperature dependence of SHG intensity collected at 5 K temperature intervals and electrical resistivity for three films with varying carrier densities. A small but finite SHG signal is measured at high temperatures for all films, but a sharp onset is observed at low temperatures for the $n_{3D} = 0.6 \times 10^{20}$ cm^{-3} and 1.4×10^{20} cm^{-3} films. Remarkably, local minimum anomalies in the resistivity occur at precisely the same temperature as the onset of SHG. We interpret these results as follows: at high temperatures, a nonzero SHG response exists due to inversion symmetry breaking by the dissimilar substrate and vacuum interfaces, producing a small polarizing field extending across the thickness of the film. As the temperature is reduced in the two lower-doped films, ferroelectric phase transitions occur resulting in a sharp increase in the SHG response. At the temperature where spontaneous ferroelectric order sets in, screening of the polar charges causes carriers to localize, decreasing the carrier density and increasing the film resistivity. In the highest doped film, the long-range dipolar interactions necessary for spontaneous ferroelectricity are sufficiently screened by charge carriers, and a polar instability is avoided. These observations demonstrate an unambiguous link between ferroelectricity and electrical transport signatures that have previously been associated with an enhancement of superconductivity [95].

To determine the symmetry of the ferroelectric order parameter, we performed SHG rotational anisotropy measurements at low temperatures. Such measurements can be used to precisely determine the full crystallographic and electronic point group symmetries of a material by measuring the individual elements of the nonlinear optical suscepti-

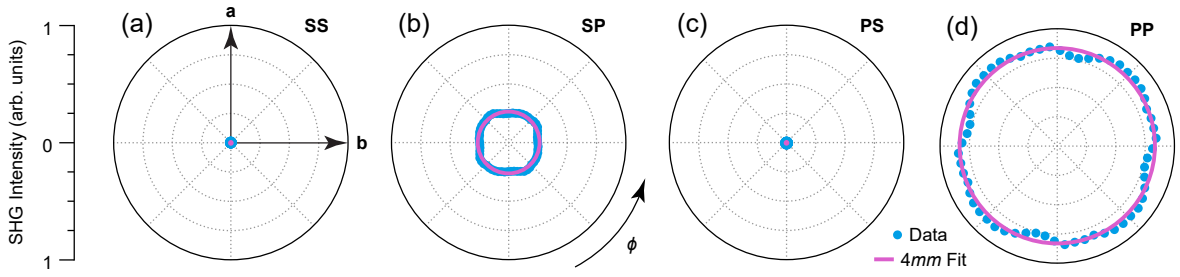

Figure 6.2: Symmetry properties of the ferroelectric phase. SHG rotational anisotropy patterns for (a) S_{in}-S_{out}, (b) S_{in}-P_{out}, (c) P_{in}-S_{out}, and (d) P_{in}-P_{out} polarization geometries measured at 10 K on a $n_{3D} = 0.6 \times 10^{20}$ cm^{-3} film. Patterns have been four-fold symmetrized to reduce noise. The polarization and angular dependence are consistent with a noncentrosymmetric $4mm$ point group, where SHG is forbidden for S_{out} geometries and ϕ-independent for P_{out} geometries. $4mm$ is the isotropy subgroup of the $4/mmm$ high-temperature tetragonal point group generated by an A_{2u} out-of-plane ferroelectric order parameter.

bility tensor [97, 98, 5]. This tensor relates the polarization response of the material at the second harmonic to the incident electric field via the equation $P_i(2\omega) = \chi_{ijk} E_j(\omega) E_k(\omega)$. Fig. 6.2 shows rotational anisotropy patterns for all four polarization channels: S_{in}-S_{out}, S_{in}-P_{out}, P_{in}-S_{out}, and P_{in}-P_{out}. We detect no measurable SHG in the S_{out} channels, while the P_{out} channels are independent of the scattering plane angle ϕ. These observations are fully consistent with a $4mm$ (C_{4v}) polar point group, where $I_{SS} = 0$, $I_{SP} \propto |\chi_{zxx}|^2 \sin^2\theta$, $I_{PS} = 0$, and $I_{PP} \propto \left|\chi_{zzz} \sin^2\theta - \chi_{zxx} \cos^2\theta\right|^2 \sin^2\theta$ are predicted by symmetry considerations [6]. Here $\theta \approx 30°$ is the angle of incidence in the experiment. The relative magnitudes of the S_{in}-P_{out} and P_{in}-P_{out} SHG responses show that the dominant nonlinear susceptibility element is χ_{zzz}, representing out-of-plane anharmonic motion of electrons driven by an out-of-plane electric field. The measured point group $4mm$ is an isotropy subgroup of the $4/mmm$ high-temperature tetragonal symmetry of the film. The symmetry lowering is generated by an A_{2u} ferroelectric order parameter directed normal to

the plane of the film, as expected for compressive strain. Identical symmetry is observed for films with other carrier densities and at other temperatures, including temperatures above the phase transition.

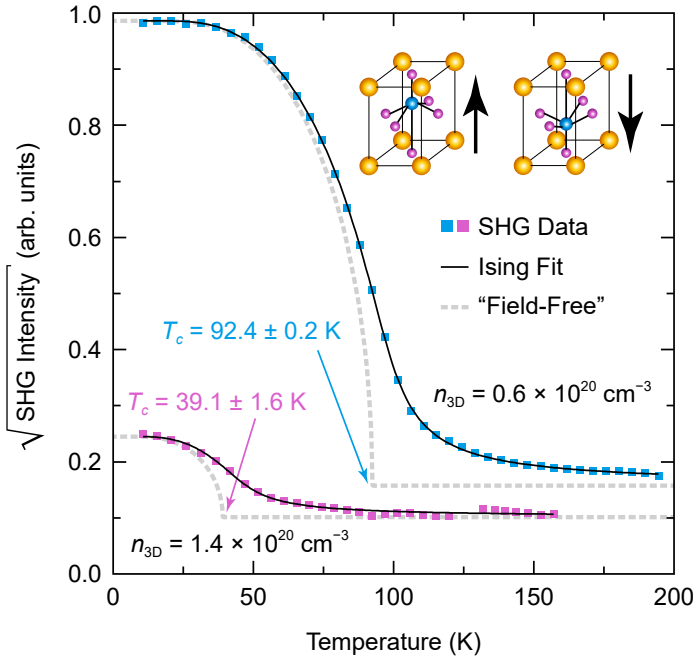

Figure 6.3: Mean-field Ising model of the ferroelectric phase transition. The square root of SHG intensity, proportional to the ferroelectric order parameter, is reproduced exactly by a mean-field Ising model that includes a small symmetry-breaking field arising from the substrate and vacuum interfaces of the thin film, as described in the text. The inset illustrates polar unit cell distortions equivalent to a bistable Ising order parameter. Dashed curves show the hypothetical order parameter in the absence of a field, from which the critical temperature of the phase transition can be estimated.

A mean-field Ising model of ferroelectricity can be used to fit the temperature dependence of the SHG intensity, as shown in Fig. 6.3. In this model, the two opposite polar unit cell distortions stabilized by in-plane compressive strain are equivalent to a bistable Ising order parameter (illustrated in the inset of Fig. 6.3). In addition to a long-range electric dipole–dipole interaction term, a small extrinsic polarizing field breaking

the symmetry of "up" and "down" configurations is included to account for the dissimilar substrate and vacuum environments sandwiching the film. The Hamiltonian of this model is

$$\mathcal{H} = -\frac{1}{2}\sum_{i,j} U(\mathbf{r}_i - \mathbf{r}_j) p_i p_j - E\sum_i p_i,$$

where i and j label unit cells, $p_i = \pm 1$ is the Ising order parameter, $U(\mathbf{r})$ is the dipolar interaction potential energy, and E is the preexisting polarizing field. Because of the long-range nature of the interaction term, which ensures that a unit cell dipole will be influenced by many of its neighbors, a mean-field approximation is expected to be accurate. Within mean-field theory, the space-averaged order parameter $\langle p \rangle$ satisfies the self-consistency equation

$$\langle p \rangle = \tanh\left(\frac{\bar{U}\langle p \rangle + E}{k_B T}\right),$$

where $\bar{U} = \sum_j U(\mathbf{r}_j)/2 = k_B T_c$ determines the critical temperature of the phase transition. $\bar{U}$ depends sensitively on carrier density because of electrostatic screening effects. To connect this statistical mechanical model to optical measurements, we assume χ_{ijk} to be proportional to the ferroelectric order parameter [98] and include a small temperature-independent background term to account for secondary SHG from the film interfaces. Solutions to the self-consistency equation fitted to the data are plotted in Fig. 6.3. From the fits, we extract bulk critical temperatures (phase transition temperatures without the polarizing field) of $T_c = 92.4 \pm 0.2$ K for $n_{3D} = 0.6 \times 10^{20}$ cm^{-3} and $T_c = 39.1 \pm 1.6$ K for $n_{3D} = 1.4 \times 10^{20}$ cm^{-3}. Polarizing field energies are on the order of $E/k_B \sim 2$ K. Although the preceding mean-field Ising model is simple, the goodness of the fits demon-

strates that such a model can accurately capture the essential physics of ferroelectricity in strained $SrTiO_3$.

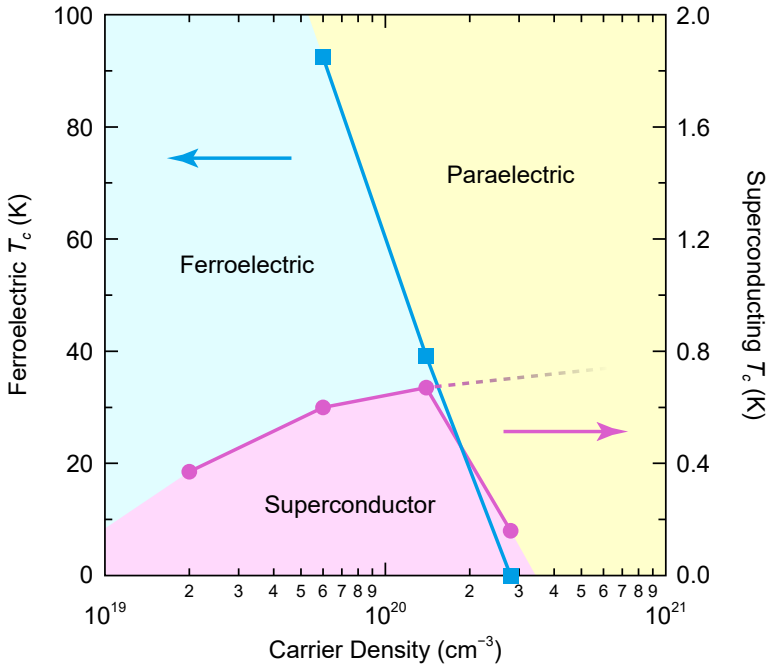

Figure 6.4: Doping–temperature phase diagram of compressively strained $SrTiO_3$. In familiar analogy with other classes of unconventional superconductors, a "dome" of superconductivity exists in proximity to the quantum critical point of a coexisting order, in this case ferroelectricity. The dome appears to terminate abruptly at the point where long-range ferroelectric order is destroyed by screening from increased charge carriers, highlighting the essential role that ferroelectricity plays in the superconducting phase.

To place our observations in a broader context, we plot the measured doping–temperature phase diagram of compressively strained $SrTiO_3$ in Fig. 6.4, showing both the ferroelectric and superconducting phase boundaries (necessarily on different temperature scales). The values for the ferroelectric critical temperature are derived from the Ising model fits discussed above, which allow us to extrapolate thin film properties to a hypothetical bulk sample without an extrinsic polarizing field. The superconducting critical temperatures,

measured in Ref. [95], are for the same films studied in this work. The phase diagram shows the well-known superconducting "dome" in $SrTiO_3$ [81] in close proximity to the quantum critical point of the spontaneous ferroelectric order. In this region, the superconducting critical temperature is enhanced by up to a factor of two in comparison with identically-doped strain-free films grown on $SrTiO_3$ substrates [95], highlighting the role played by strain-induced spontaneous ferroelectricity. We emphasize, moreover, that the superconducting enhancement cannot be due to strain alone because the enhancement only occurs in a finite range of carrier densities near the ferroelectric quantum critical point. In addition, the superconducting dome appears to terminate prematurely at the ferroelectric phase boundary, where screening by charge carriers overcomes any tendency towards a polar instability.

In conclusion, we used optical second harmonic generation to measure the doping and temperature dependence of the out-of-plane ferroelectric polarization in compressively strained $SrTiO_3$ thin films. We found a direct link between enhanced superconductivity and the onset of spontaneous ferroelectricity. We also developed a mean-field Ising model to capture the essential physics of the ferroelectric order parameter. Our results support a long-suspected connection between ferroelectricity and superconductivity in $SrTiO_3$ and should have significant value for developing and testing theoretical models relating superconductivity and ferroelectric fluctuations.

6.3 Disentangling the effect of localized magnetic states and charge doping

By doping strained $SrTiO_3$ films with Sm, we were able to simultaneously tune the ferroelectric transition and modulate T_c. While the effect was explained in terms of adding extra free charge carriers to the system, Sm^{3+} ions also introduce magnetic moments through localized unpaired f-electrons. To study the effect of charge doping separately from the effect of magnetic ions, we optimally dope (i.e., doping that results in maximum T_c) strained films of $SrTiO_3$ with Sm, and further introduce Eu into the films [99]. Eu is isovalent with Sr, and so substitutes into the lattice without adding extra electrons. It does, however, introduce additional f-electrons, which allows for the study of magnetism separately from charge doping.

Figure 6.5 shows the SHG response of the Sm-doped $SrTiO_3$ films with 0, 0.5%, 2%, and 3% Eu as a function of temperature from 10 K to 200 K. As the temperature is reduced, the Sm:$SrTiO_3$ film with 0% Eu shows a sharp increase in the SHG response, indicating the ferroelectric phase transition at 92 K (this is a repeat measurement of the sample in Fig. 6.1(a)). The film with 3% Eu showed a similar transition. The films with 0.5% Eu and 2%, curiously, did not show a significant change in SHG signal with temperature. All films have a finite high-temperature SHG signal, which is due to polar nanodomains [100, 101] and potentially other contributions to the SHG such as surface electric dipole SHG and bulk electric quadrupole SHG.

Naively, one would expect the strength of the transition seen in SHG measurements to decrease monotonically as a function of increasing Eu doping if the presence of magnetic moments is detrimental to establishing polar order. Instead, we find that the ferroelectric state is remarkably robust to Eu doping and is instead more sensitive to strain relaxation in the films. The films with 0.5% and 2% Eu doping were both slightly strain relaxed, resulting in an incomplete and inhomogeneous compressive strain across the film. This can be seen in the sheet resistance and upper critical field measurements reported in Ref. [99], where changes in superconducting T_c and H_{c2} can be completely accounted for by n_{3D}. The remarkable finding of this study is that superconductivity and ferroelectricity are insensitive to significant (few-percent) amounts of magnetic dopants, contrary to the expectation for a conventional s-wave superconductor.

6.4 Local polar order and the role of strain-relaxation

As strain relaxation was proven to be a key parameter in tuning the ground state of doped $SrTiO_3$ films[99], we realized that while a *global* ferroelectric state may be somewhat fragile, *local* ferroelectric order may be sufficient to facilitate an unconventional pairing mechanism which relies upon broken inversion symmetry. So far, ferroelectricity in these films has been studied only in the context of coherently strained films, and the role of local inversion symmetry breaking has not yet been considered.

The behavior of the nanodomains is systematic as a function of carrier density[101], strain, and proximity to the ferroelectric transition. Below, we investigate the relationship

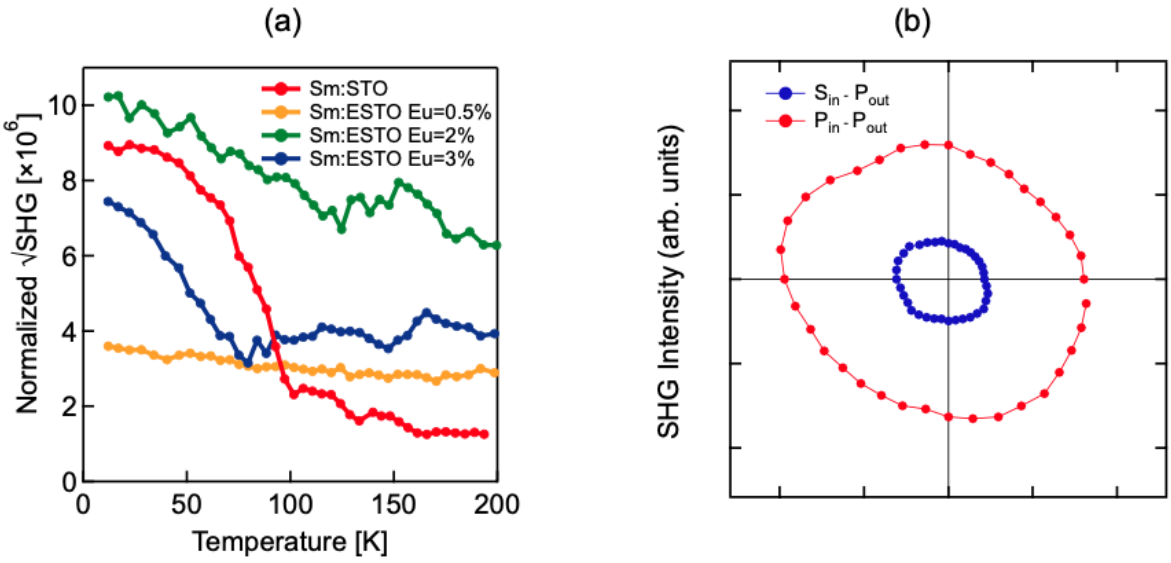

Figure 6.5: (a) Temperature dependence of SHG intensity for films doped with Eu. Only the Eu-free and Eu=3% samples show a global polar phase transition. (b) SHG rotational anisotropy for the film with 3% suggests the noncentrosymmetric $4mm$ point group. Note, the SHG signals were normalized to the incident laser beam power. Reproduced from Ref. [99]

between nanodomains and strain, and the impact of domain size on ferroelectricity and superconductivity. We keep the carrier density constant, but vary the degree of strain relaxation in epitaxial thin films[102].

Thin films are grown by MBE with rare-earth dopants. Films A and C are doped with Sm, and films B and D with La. We will recall from above that Sm dopes with charge carriers and magnetic unpaired f-electrons, while La is simply an n-type dopant. However, T_c is insensitive to the type of dopant [99]. The carrier density (n_{3D}) was calculated from the Hall effect at 300 K and ranged between 6 and $8 \times 10^{19}\text{cm}^{-3}$, which is slightly on the underdoped side of the superconducting dome of the phase diagram[96].

Films were grown to a thickness of ∼180 nm, near the critical thickness for strain

relaxation on LSAT [103]. Sample A was fully strained, while films B, C, and D showed some strain relaxation in XRD (Fig. 6.6).

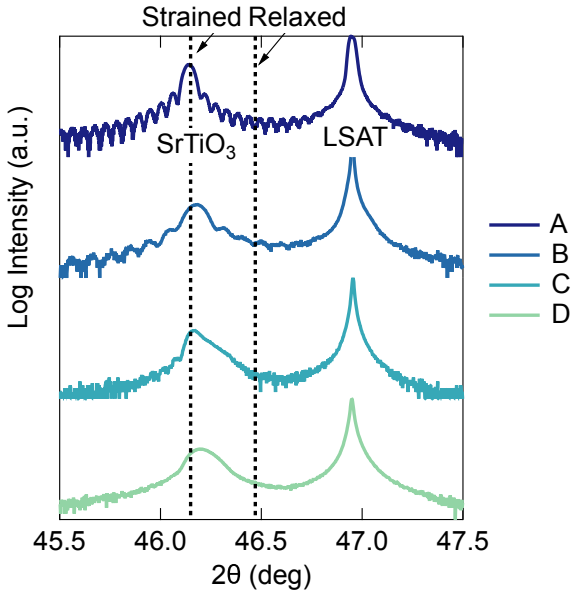

Figure 6.6: High-resolution X-ray diffraction data of films A - D. The dashed lines indicate the 2θ values corresponding to out-of plane lattice parameters for fully strained and fully relaxed $SrTiO_3$ films, respectively. Reproduced from Ref. [102]

Figure 6.8 shows temperature-dependent SHG intensity for samples A–D between 200 and 10 K. Upon cooling, only the fully strained sample A shows a sharp increase in the SHG response, which indicates the transition to a globally ferroelectric phase at ∼90 K. As shown previously, the electric polarization is normal to the film plane in film A [96]. In contrast, samples B, C, and D do not show a ferroelectric transition.

The SHG signal changes gradually and linearly with temperature, without clear signs of saturation at low temperature. This strongly suggests the absence of a long-range ordered ferroelectric state, regardless of in-plane or out-of-plane polarization. It is important to note that SHG is sensitive only to polarized domains which are larger than

the spot size of the laser. However, if ferroelectric domains larger than the laser wavelength but smaller than the laser spot size exist, one expects to see a speckle pattern. No such pattern is observed experimentally, and therefore we rule out the existence of these domains. All samples have a weak but finite SHG signal which persists to high temperatures, likely due to a combination of diffuse SHG from the presence of polar nanodomains, smaller than the laser wavelength, and higher-order optical processes such as electric quadrupole SHG that do not depend on the breaking of inversion symmetry.

High-angle annular dark-field scanning transmission electron microscopy (HAADF-STEM) reveals that in film A the Ti-O columns displace primarily along [001] (red color) and form large polar nanodomains. This is consistent with the finding that coherently strained films have an out-of-plane polarization and a global ferroelectric state [96]. The other films (B–D) have smaller domains with polarizations parallel to $[00\overline{1}]$, [010], and $[0\overline{1}0]$, respectively. Nanodomains span approximately eight unit cells at the largest with average Ti-O column displacements of $\sim$10 pm for all films. In the partially relaxed films, the polarization direction is not strongly pinned to the out-of-plane direction, in contrast to film A. The different polarization directions average to give an isotropic, but finite, SHG signal. Nevertheless, all films exhibit a substantially enhanced T_c. The major finding of this study is that a global polar state is *not* required for enhanced T_c, establishing the importance of a local order picture.

The intuitive explanation for the persistence of enhanced T_c is as follows: if polar domains are larger than the separation of the Cooper pairs, then the Cooper pairs

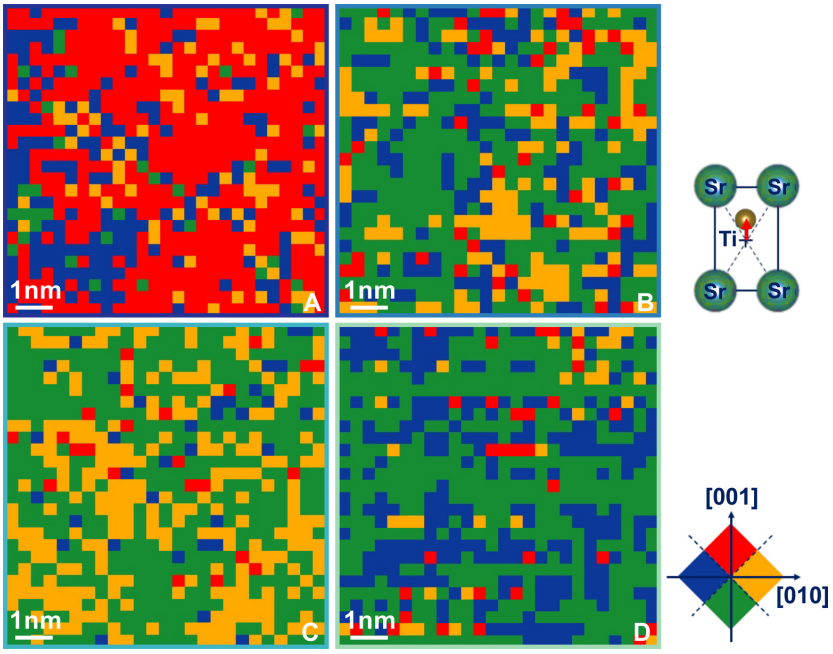

Figure 6.7: HAADF-STEM results showing polar domains in films A–D. Each pixel represents the displacement of the Ti-O column in that unit cell. Reproduced from Ref. [102].

still experience a noncentrosymmetric environment. In this case, sufficiently large nanodomains achieve the same enhancement of T_c as a globally ferroelectric film. We can then tie in these findings to earlier studies of carrier concentration: unstrained films also show polar nanodomains, though they are quite small (3.9 ± 0.9 unit cells). Overdoped films, however, have no nanodomains at room temperature [102] (though low temperature measurements have not been performed to check for formation of nanodomains). In strained films, T_c is rapidly suppressed upon a slight increase in carrier density; this supports the idea that nanodomains are suppressed at all temperatures due to screening by free carriers. Thus, all results are consistent with the length scale of polar order determining T_c of $SrTiO_3$.

These experiments represent accumulating evidence that superconductivity in $SrTiO_3$ is intimately linked with, and potentially requires, inversion symmetry breaking. This would provide a natural explanation as to why ferroelectricity and superconductivity vanish at similar carrier densities on the overdoped side, where the nanodomains collapse upon screening by the free carriers (Figure 6.4).

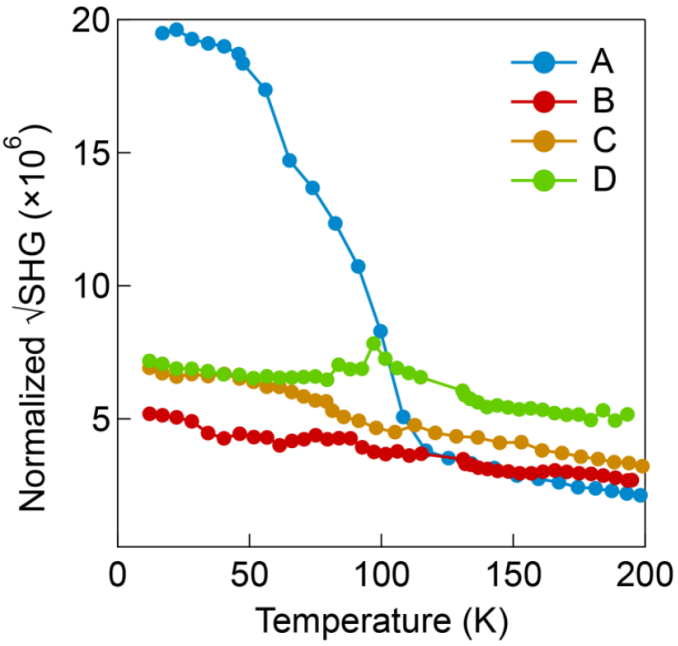

Figure 6.8: Temperature dependence of the SHG intensity of films A–D. Partial strain relaxation suppresses the transition to a global ferroelectric phase. Reproduced from Ref. [102].

6.5 Critical film thickness for polar order and superconductivity

Another avenue for control over ferroelectricity and superconductivity is through the film thickness. As the two phenomena have been shown to have linked behavior when tuning other parameters such as strain and charge doping, here we investigate their dependence on spatial confinement of charge carriers and find a critical thickness for both ferroelectricity and superconductivity.

In general, perovskite thin films which have a polar phase exhibit a critical thickness on the order of several unit cells, below which ferroelectricity is suppressed by depolarization fields [104, 105]. Separately, T_c can be suppressed with decreasing film thickness[106], however the mechanism does not in general share common physics with the suppression of ferroelectricity in thin films. As such, while both phases may disappear in sufficiently thin films, there is no fundamental reason why superconductivity and ferroelectricity should vanish at the same thickness if the two phenomena are not intrinsically related.

In this study [107], Sm-doped, compressively strained $SrTiO_3$ films are grown with four different thicknesses: 70, 40, 25, and 10 nm (labeled A–D in order of decreasing thickness). The two thinnest films, C and D, are capped with a layer of Sm-doped $EuTiO_3$ which prevents carrier depletion at the $SrTiO_3$ film surface. Additional films with thickness 25 and 10 nm are also grown without capping layers to ensure that there are no unintended effects induced by the capping layer.

The temperature evolution of the ferroelectric order parameter was measured using optical second harmonic generation (SHG) experiments as described above. In an updated method, each point shown in Figure 6.9 is an average of many points taken continuously as the temperature is ramped. The SHG intensity at each reported temperature is the average of the points within a chosen temperature interval. The primary source of noise in the SHG data is a result of low-frequency laser power fluctuations. To account for this, we report error bars which are calculated as root mean square errors from linear fits to the data from films that did not undergo a ferroelectric transition.

Thickness fringes from X-ray diffraction (Ref. [107] Figure 1) confirmed that interfaces are smooth and that the films are coherently strained. While the thicker films (A and B) became superconducting, the thinner films did not. Films A and B undergo a ferroelectric transition at $\sim$100 K, consistent with the transition measured in similar samples above. Figure 6.9 also shows that the thinner, non-superconducting films (C and D) do not undergo a ferroelectric transition.

The uncapped films (25 and 10 nm thick) additionally did not undergo a ferroelectric transition. However, these films suffer from carrier depletion, which can destabilize the ferroelectric phase. Though there exists a small step in the data from the uncapped 25 nm film around 70 K, it is unlikely to be intrinsic to the sample. Rather, it is likely to be an experimental anomaly arising from the measurement itself, given that the points reported both above and below in temperature maintain the linear trend. As expected from previous studies, all films show finite SHG intensity above the ferroelectric transition

temperature, arising from inversion symmetry breaking at interfaces or surfaces, polar nanodomains, and higher-order terms independent of inversion symmetry breaking.

The results of the SHG measurements indicate that ferroelectricity in doped, strained films appears to disappear between 25 and 40 nm. This critical thickness is large compared to other ferroelectric perovskites, which tend to lose ferroelectricity at a thickness around several nanometers. Additionally, strained, *undoped* films of $SrTiO_3$ remain ferroelectric to at least 20 nm [108]. The presence of free carriers in doped films likely contributes to the early collapse of the ferroelectric phase and the suppression of nanodomain formation.

What is even more interesting is that superconductivity in these films also disappears at the 25 nm thickness threshold. This is an unexpected result, given previous reports of quasi-two-dimensional superconductivity in 2D electron gases at the surface of $SrTiO_3$ [109]. Again, if ferroelectricity and superconductivity were unrelated phenomena in $SrTiO_3$, there is no reason that the critical thickness for both phenomena should be the same. The discovery that the two critical thicknesses are in fact the same further supports the idea that the two phenomnea are related.

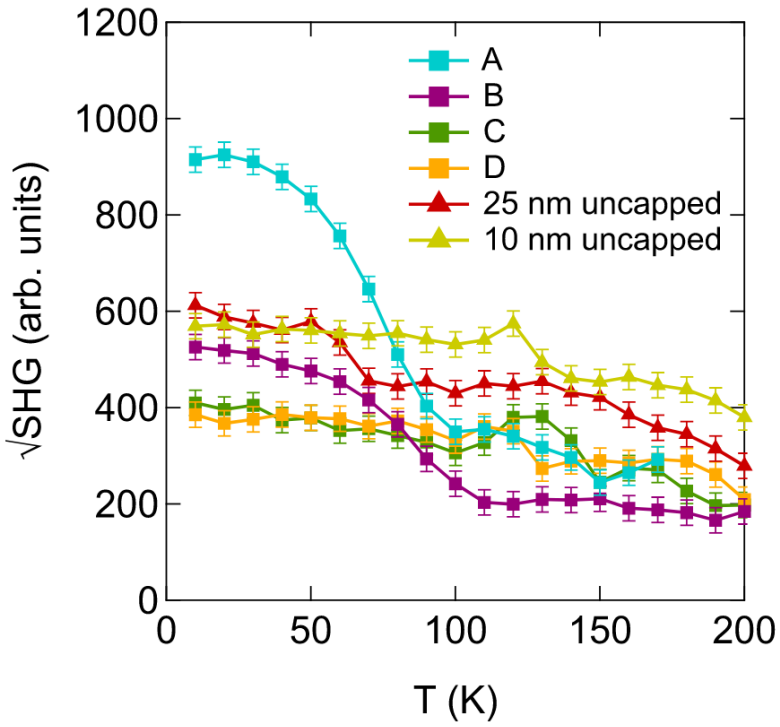

Figure 6.9: SHG response as a function of temperature in films with different thickness. The ferroelectric transition is suppressed for the thinnest films at 25 and 10 nm thickness. The primary source of error in the measurements is low-frequency laser power fluctuations. As such, reported error bars are the root mean square errors of linear fits to samples which are not ferroelectric. Reproduced from Ref. [107].

6.6 Alloying with Eu: crossover from global to local polar order

Having found several ways to control the polar and superconducting transition in $SrTiO_3$ films, we return to a parameter which had little effect in a previous study [99]: doping with Eu. Due to nearly identical bulk lattice constants between $SrTiO_3$ and $EuTiO_3$, and similar ionic radii between Sr^{2+} and Eu^{2+}, Eu can be alloyed at large concentrations without altering the strain state of the material. This makes Eu an ideal ion with which to study the effect of heavy magnetic doping in isolation from other variables. Here, we investigate compressively strained, Sm-doped films of $Eu_xSr_{(1-x)}TiO_3$ with significantly higher concentrations of Eu in an attempt to find a critical magnetic doping concentration [110].

As before, moderately thick (70-100 nm) films are doped near optimal T_c with Sm^{3+} and then further doped with Eu^{2+}. Using what we learned from our previous study on film thickness, a thin (10 nm) Sm-doped $EuTiO_3$ capping layer is used to prevent issues with carrier depletion at the film surface. X-ray photoemission spectroscopy estimates the Eu doping concentration across films labeled B1-B3 as x=0.09, 0.14, and 0.30, respectively.

Figure 6.10(a) shows the SHG intensity measurements for the series B films, scaled by film thickness. As in the study previously discussed [107], many data points are continuously measured as the temperature is changed. Each SHG intensity point shown is the average of the points within a chosen temperature interval. A strained, 0% Eu

sample is included for reference (same sample as seen in Fig. 6.1(a)).

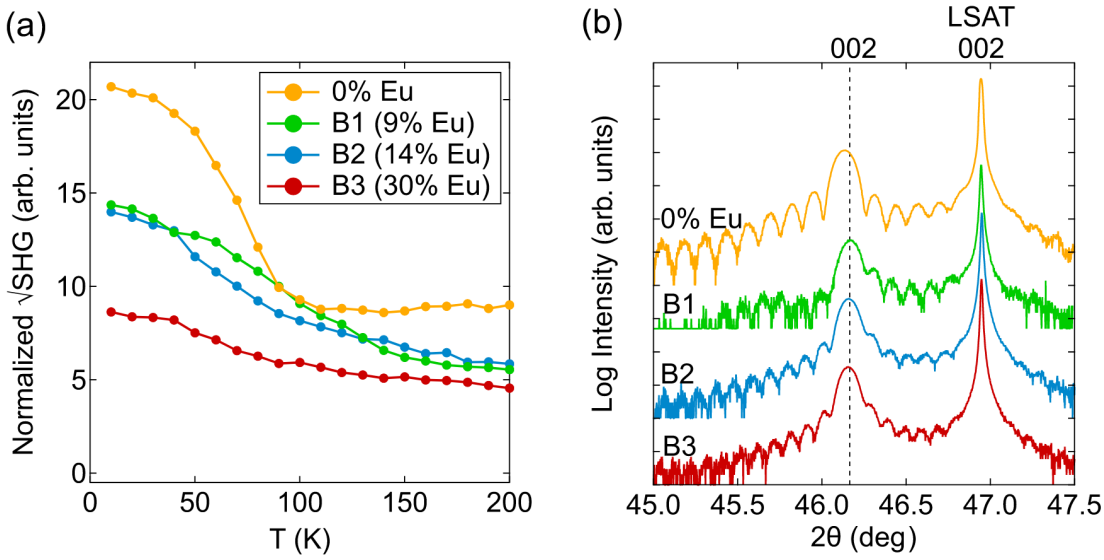

Figure 6.10: SHG intensity as a function of temperature in films with higher Eu doping (0, 9%, 14%, and 30%). Doping with increasing Eu gradually suppresses the polar transition. Reproduced from Ref. [110].

Here, all Eu-doped films lack the sharp polar transition that appears in films with sufficiently low (or zero) Eu doping. Signs of a polar transition exist as a shallow, broad increase in the SHG which saturates at low temperature, and the transition weakens as a function of increasing Eu concentration. By x=0.30, the polar transition has essentially disappeared. While strain relaxation is a known culprit for the suppression of ferroelectricity [102], XRD indicates that films are coherently strained (Fig. 6.10(b)).

Having ruled out strain relaxation, we seek an explanation for the disappearance of the polar phase in the presence of Eu. Hall transport measurements indicate that all films have similar n_{3D} at high temperature, which decreases due to carrier depletion near 100 K (Ref. [110] Figure 5(d)). Notably, films with increasing concentration of Eu have

decreasing carrier depletion, indicating that free carriers are not localizing to screen polar nanodomains. Sheet resistance measurements (Ref. [110] Figure 5(a,b)) also lack any anomalies which would typically accompany magnetic ordering, indicating that all films remain paramagnetic.

Films with x=0.09 were also doped with different levels of Sm to check for a superconducting dome. The superconducting T_c in these films (shown in Ref. [110] Figure 3) follow the same trends as found in previous studies of films without Eu [107]. However, it is noted that H_{c2} in these 9% Eu films is strongly suppressed, even compared to films with 3% Eu. The critical field values H_{c2} for in-plane and out-of-plane external fields also converge with increased Eu doping, indicating that the film is becoming less anisotropic.

Given the lack of both magnetic order and inhomogeneous strain, the presence and size of polar nanodomains again appear to be candidates to explain the changes in highly Eu-doped films. STEM shows no polar nanodomains at room temperature for the x = 0.09 film, while undoped films do have nanodomains at room temperature. This, taken with a suppressed global ferroelectric transition in the SHG, indicates that the addition of x = 0.09 Eu has led to a crossover to a phase in which a long-range ordered state cannot be established. However, increasing SHG at low temperature still points to an increasing polarization upon cooling.

Our interpretation of these data is that the addition of Eu to the $SrTiO_3$ host lattice decreases the lattice polarizability and leads to a crossover from a uniform polar ferroelectric ground state to a phase that hosts only local polar regions. The decrease in H_{c2}

which accompanies the suppresion of ferroelectricity suggests that a polar phase may prevent magnetic depairing of Cooper pairs. Beyond x=0.09, films remain superconducting to at least $x = 0.14$. In this regime, local polar regions support Cooper pairing in an inversion-symmetry broken environment, until superconductivity is finally suppressed between $0.14 < x < 0.30$. At these very high Eu concentrations, the destruction of the superconducting phase may be associated with a complete suppression of the polar phase. We emphasize that the loss of superconductivity does not appear to be driven by magnetic ordering or lattice disorder, but by suppression of polar nanodomain formation. Finally, we note that tuning $SrTiO_3$ films closer to their putative quantum critical point suppresses superconductivity, rather than enhancing it. This provides further evidence that the superconductivity in $SrTiO_3$, whatever the pairing mechanism, is not mediated by fluctuations of the polar order which are enhanced near a critical point.

Chapter 7

Study of ultrafast dynamics in Ca_2RuO_4 via pump-probe spectroscopy

A characteristic feature of the ruthenate oxides is that the relevant electronic states derive from three t_{2g} orbitals which are occupied by four electrons. As compared to the $3d$ compounds, the $4d$ orbitals are extended and space and result in weaker intra-atomic Coulomb interaction U. The extended nature of the $4d$ orbitals also increases the interaction between the d- and nearest-neighbor oxygen orbitals, leading to distortions away from the parent K_2NiF_4 structure. These distortions generally include octahedral rotations which result in deviations away from 180° of the metal-oxygen-metal bond angle, reducing the d-electron bandwidth and favoring insulating behavior. A rare example of

a $4d$ t_{2g} insulator, Ca_2RuO_4 provides a material system in which to study the interplay of structural and electronic degrees of freedom. Here, we present ultrafast optical pump-probe studies of thin-film Ca_2RuO_4 grown on $LaAlO_3$ (LAO) by molecular beam epitaxy.

7.1 Metal-insulator transition in Ca_2RuO_4

The layered perovskite oxide Ca_2RuO_4 is a multiband Mott insulator with a high temperature metallic state and a low temperature insulating state. It is a tetragonal material with space group Pbca. The insulating state is accompanied by a structural distortion at 365 K, and antiferromagnetic (AFM) magnetic order sets in at 110 K in bulk samples. As with many other transition metal oxides (TMOs), partially filled d-shells result in a correlated electronic state. The Mott phenomenon, i.e. the localization of electrons due to strong Coulomb repulsion (and as a result, a reduced bandwidth), is typically regarded as key to the physics of the observed strong correlations in the TMOs.

The temperature-driven insulator-metal transition in Ca_2RuO_4 accompanies an isosymmetric structural transition, where the c-axis lattice parameter serves as a proxy for the state of the system. In the high temperature metallic phase, the c-axis is long (denoted L-Pbca). Upon cooling and entering the insulating phase, the c-axis shortens (denoted S-Pbca). This shrinking of the c-axis lattice parameter is accompanied with an increase in the tilt angle of the RuO_6 octahedra. This distortion lowers the energy of the xy orbital, which becomes completely filled with two electrons, while the xz and yz orbital become half filled. The bands contributed by these orbitals become narrower and lead

to the Mott insulating state. These octahedral tilts couple strongly to strain fields, and the properties of the material correlate strongly with its local structure. This makes Ca_2RuO_4 a promising material in which control of physical properties can be achieved by relatively small external perturbations. Below, we study the effect of ultrafast photoexcitation on the dynamics of Ca_2RuO_4 and the fundamental interactions between its structural and electronic degrees of freedom.

7.2 Ultrafast volume expansion

We use ultrafast optical pump-probe reflectivity measurements to investigate the photoinduced insulator-to-metal transition in a 25 nm strained thin film of Ca_2RuO_4 epitaxially grown on an $LaAlO_3$ [001] substrate [111]. A pump wavelength of 1.64 eV excites electrons across a 1.2 eV band gap and induces an ultrafast isostructural insulator-metal transition. A rapid (sub-picosecond) photoinduced change in electronic properties is indicated by the sharp increase in reflectivity. The changes in reflectivity persist to 100 ps (Figure 7.1), and even longer, as shown below (Figs. 7.3 and 7.4).

Optical transient reflectivity measurements are complemented by time-resolved x-ray diffraction and optical-pump terahertz-probe measurements which enable a comparison between electronic and lattice dynamics. Time-resolved X-ray diffraction indicates a photoinduced lattice expansion via the change in the 008 Bragg peak, which is a proxy for the '*c*-axis' lattice parameter. 4 ps after photoexcitation, the lattice has shifted from the *S-Pbca* insulating phase to the *L-Pbca* metallic phase. Terahertz reflectivity indicates

a possible metallic response from photoinduced carriers, and has a slower rise time than the optical reflectivity and X-ray diffraction.

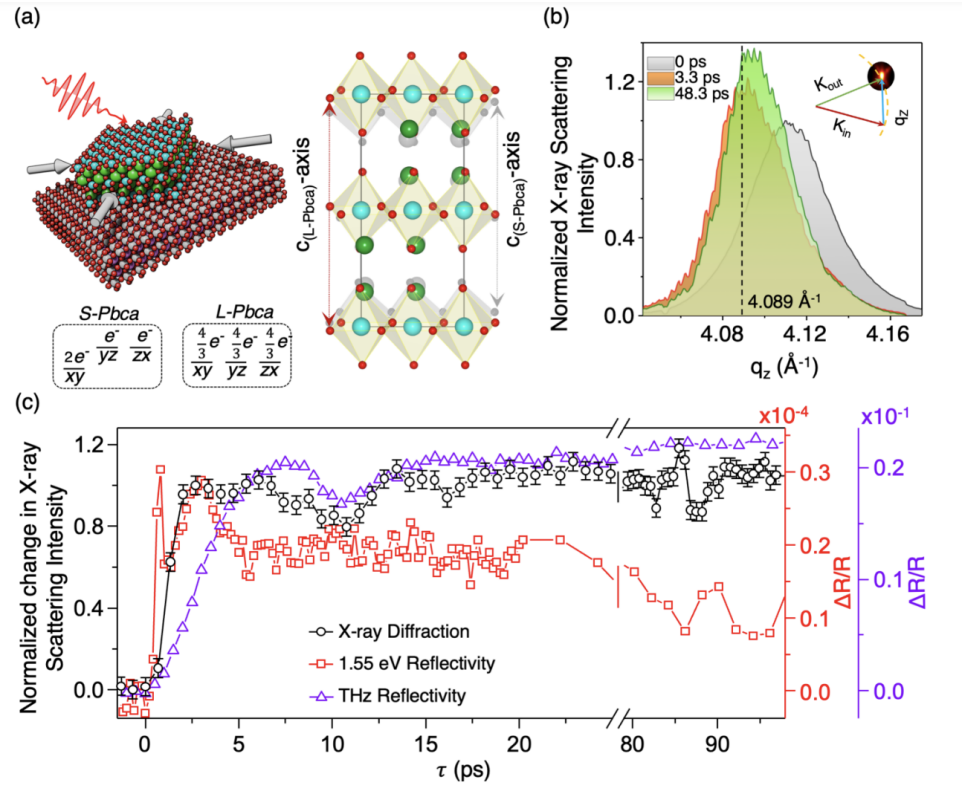

Figure 7.1: (a) Schematic representation of the epitaxially strained thin film which undergoes an isosymmetric structural phase transition from *L-Pbca* to *S-Pbca*, and electronic configuration of Ru *d*-orbitals in Ca_2RuO_4. (b) Photoinduced dynamics of 008 Bragg peak of strained Ca_2RuO_4 thin film at pump fluence of 50 mJ cm^{-2}, where the peak-shift towards a lower momentum transfer indicates a lattice expansion. (c) The time-resolved normalized change in the scattering intensity (black squares, incident pump fluence 50 mJ cm^{-2}). The time-resolved optical reflectivity (red circles, E=1.55 eV, incident pump-fluence 0.14 mJ cm^{-2}) increases rapidly (within 1 ps) and shows a broad peak coincident with the lattice expansion. A finite optical transient reflectivity persists for over 100 ps. The time-resolved THz reflectivity signal (purple triangles, THz-bandwidth from 0.8 meV to 10 meV, incident pump-fluence 15.1 mJ cm^{-2}) increases within ∼8 ps and persists for 100 ps. Reproduced from Ref. [111]

7.3 Other observations from transient reflectivity measurements

7.3.1 Temperature dependence

The thin films of Ca_2RuO_4 studied here are known to have a metal-insulator transition at 200 K – a suppressed value compared to that of the bulk material (365 K). Reflectivity transients in the above study were collected at 130 K (well below the MIT). To study the change in dynamics across the phase transition, we collect data across a wide range of temperatures.

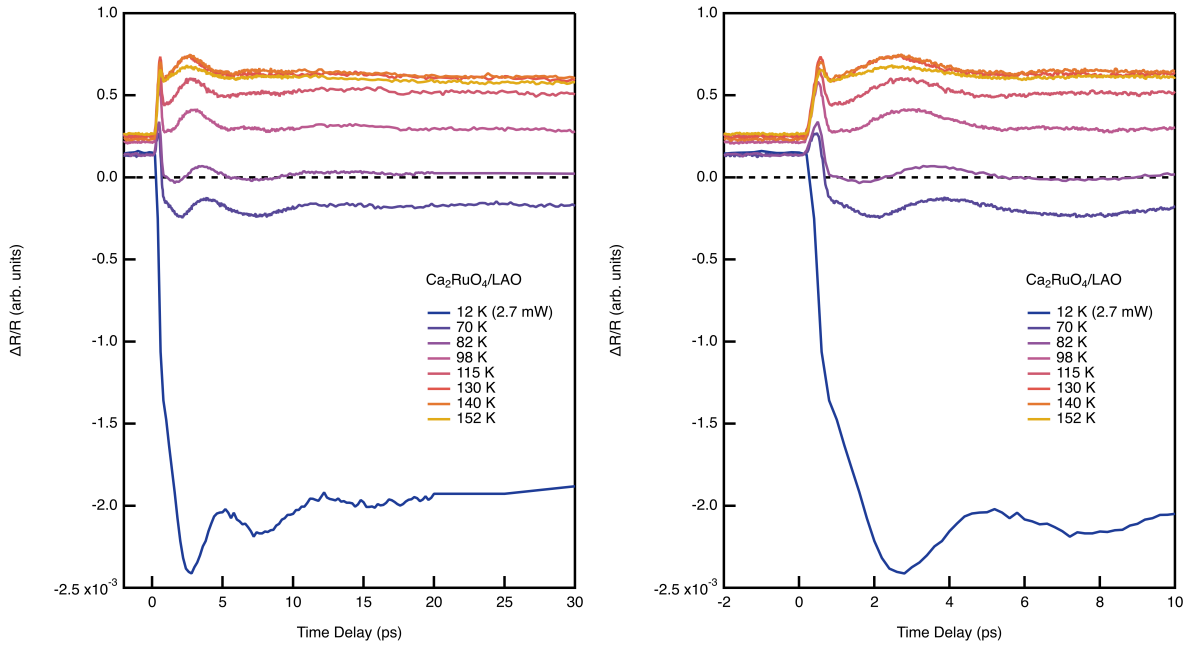

Figure 7.2: Temperature dependence of transient reflectivity of Ca_2RuO_4/LAO. $\Delta R/R$ up to 30 ps time delay (left), and $\Delta R/R$ up to 10 ps time delay (right).

Several features are apparent from a study of the temperature dependence: 1) Strong

oscillations occur in the transient reflectivity at all temperatures, indicating a mode which couples strongly to the pump wavelength (757 nm). 2) At intermediate temperatures around 100 K, $\Delta R/R$ transitions from positive to negative for at least some range of time delay, indicating that the effect of the pump at these temperatures is to decrease, rather than increase, the reflectivity. There is a global maximum in $\Delta R/R$ which appears to occur around 130 K. 3) the magnitude of the transient reflectivity is much larger and the sign is negative at low temperature. The low temperature dynamics of this system are curious, and will be discussed further in the next section regarding pump-fluence dependence.

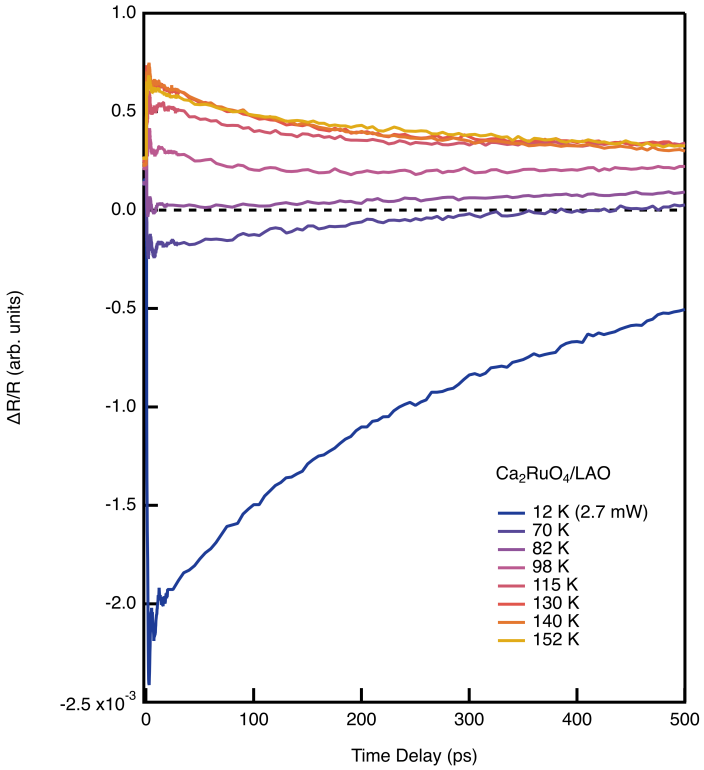

Figure 7.3: Temperature dependence of transient reflectivity of Ca_2RuO_4/LAO. $\Delta R/R$ up to 500 ps time delay.

It is known that bulk Ca_2RuO_4 crystals exhibit a sharp decrease in reflectivity under optical pumping at near-IR wavelengths in the insulating phase [112]. A previous study also reports that there is a transition between negative and positive $\Delta R/R$ between the insulating and metallic state of a Fe-doped bulk crystal [113]. However, the continuous tuning between negative and positive $\Delta R/R$ demonstrated in Figures 7.2 and 7.3 suggests that the MIT is not a steep, discontinuous function of temperature in these strained films. Our study [111] on these same thin film samples indicates a nano-textured coexistence between the insulating and metallic phases in this system. This may explain the smeared-out transition, which could be a result of a continuous tuning of the fraction of metallic and insulating regions with temperature. An outstanding question is why the crossover between positive and negative transient reflectivity occurs at a temperature below the MIT. This lower apparent temperature could be the result of heating by the pump laser, which could be calculated as in [60].

A closer look at the high-temperature (metallic-like) phase reveals a positive $\Delta R/R$ as well as coherent oscillations. A clear mode with period on the order of $\sim$ 30 ps is visible in the long time-delay transients (Figure 7.4).

Higher-frequency oscillations have been reported previously [112] at 3.8 THz and above. It is possible that these modes exist in the thin films studied here, though the effects of strain and the nano-texture on the phonon frequency and amplitude are an open question. Additionally, the measurements performed here likely do not have the frequency resolution to observe these modes. Another notable feature in these high-temperature

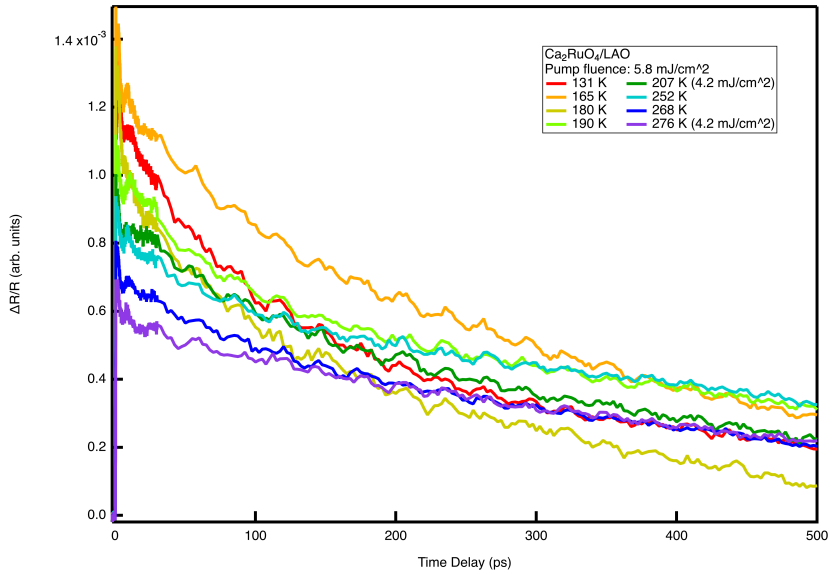

Figure 7.4: Temperature dependence of transient reflectivity of Ca_2RuO_4/LAO from 131 K to 276 K for time delay up to 500 ps.

reflectivity transients is the broad peak centered near 2-3 ps time delay, which coincides with the time of the lattice expansion [60]. A similar feature was previously observed in Fe-doped Ca_2RuO_4 crystals and was attributed to Brillouin scattering [113].

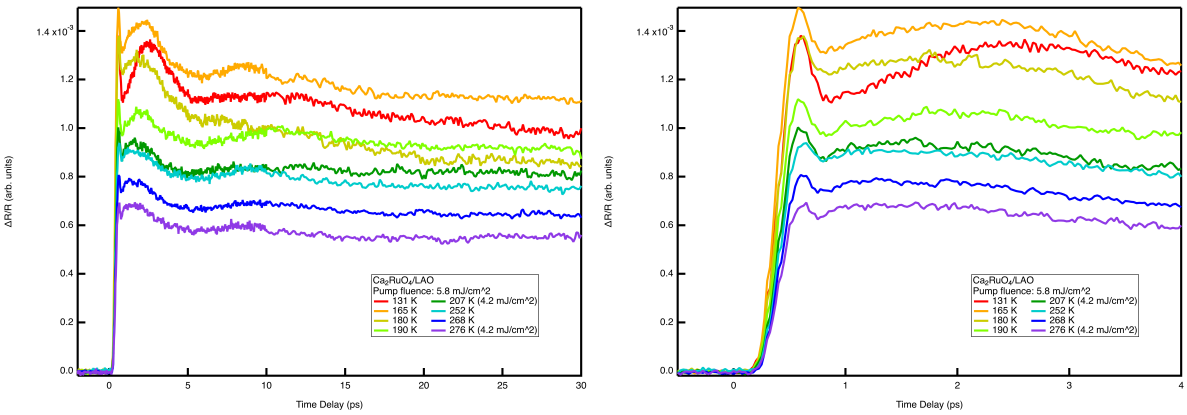

Figure 7.5: Temperature dependence of transient reflectivity of Ca_2RuO_4/LAO from 131 K to 276 K for time delay up to 30 ps (left) and up to 10 ps (right).

7.3.2 Pump-fluence dependence

Transient reflectivity varies linearly with pump fluence at intermediate temperatures (∼130 K). Figure 7.6 shows the reflectivity transients as a function of fluence tuned through the average power. Measurements were made with a pump power between 0.25 and 9.7 mW, spanning more than an order of magnitude. An interesting feature of the data is that the pre-time-zero signal also increases linearly as a function of pump fluence. Generally, condensed matter systems will fully equilibrate within several hundred picoseconds unless a long-lived metastable state has been established. Evidence from pump-probe X-ray diffraction and optical-pump terahertz-probe spectroscopy also suggest that the films remain in an out-of-equilibrium state for at least 100 ps after excitation.

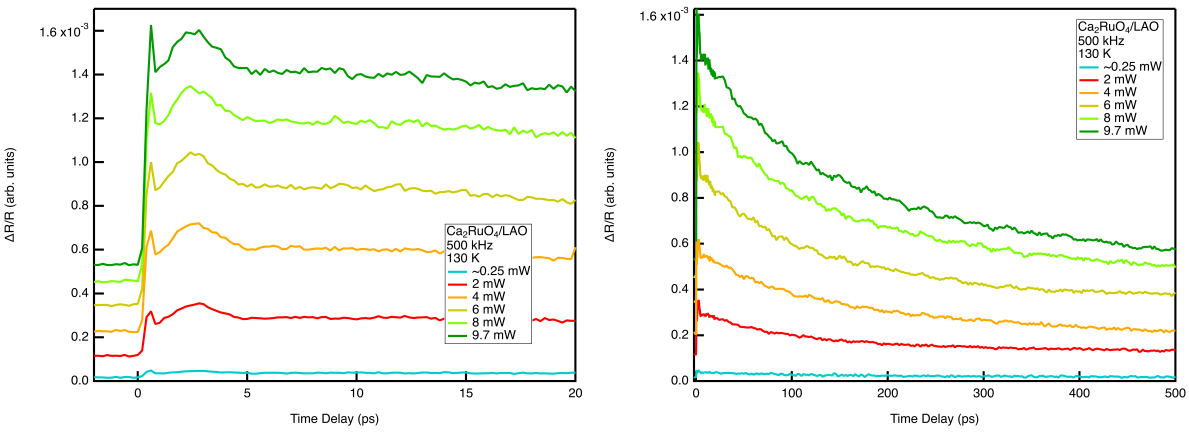

Figure 7.6: Linear pump-fluence dependence of transient reflectivity at 130 K for time delay up to 20 ps (left) and 500 ps (right). Note the non-zero signal at negative time delay, indicating a long-lived metastable state.

7.3.3 Nonlinear response at low temperature

Although the transient reflectivity depends linearly on pump fluence at higher temperatures, the response becomes highly nonlinear at low temperatures. Figure 7.7 shows the transient reflectivity as a function of pump fluence at 12 K for pump powers between 1 and 11.3 mW. At 6.6 mW, the shape of the short time delay response changes dramatically and coherent oscillations appear. The origin of this change in optical response is unknown, and motivates future study into the system.

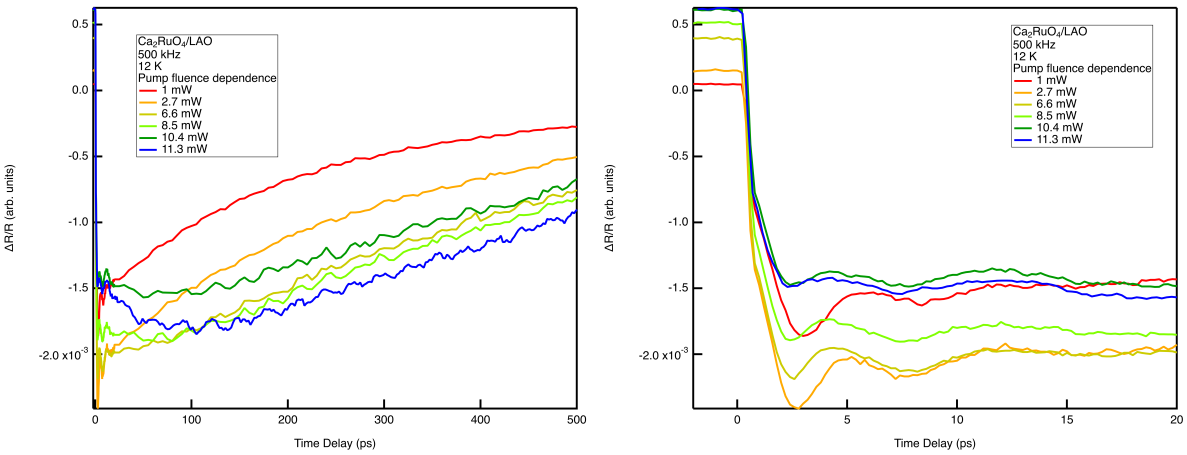

Figure 7.7: Unusual pump-fluence dependence of low-temperature (12 K) transient reflectivity. The line shape changes dramatically during the first few tens of picoseconds after optical pumping. A coherent mode appears at a critical fluence corresponding to ~ 6.6 mW. $\Delta R/R$ shown for time delay up to 500 ps (left) and 20 ps (right).

Chapter 8

Future directions

8.1 Optical studies of $SrTiO_3$

Having performed an extensive set of measurements linking the ferroelectric and superconducting phases of $SrTiO_3$, the question of the superconducting pairing mechanism remains open. While a phonon-mediated pairing mechanism seems unlikely from a comparison of the Fermi energy and the ferroelectric soft-mode phonon frequency, there exist planar tunnel junction measurements which claim to show that the lowest-energy transverse optical phonon, TO1, maintains an energy lower than that of the Fermi energy [114]. Cooper pairing via this phonon would resolve the apparent anti-adiabatic pairing regime problem, though typically electron coupling with the TO1 phonon is not allowed by symmetry. There exist theoretical proposals for two-phonon pairing, as well as phonon-mediated interorbital electron tunneling, which would enable coupling to the TO1 phonon [115].

The studies to date have considered only chemically doped bulk $SrTiO_3$, and the hierarchy of energy scales found in these samples is not guaranteed to hold in strained, doped films. A study which could test the hypothesis of a viable TO1 phonon pairing mechanism in such films could be performed using Raman spectroscopy to monitor the TO1 phonon frequency as a function of charge doping over the range of carrier densities where the superconducting dome is found. The mode frequency can then be compared to the Fermi energy to check the validity of the proposed theory. Additional complications may arise from measurement of the Fermi energy in epitaxial films, which was performed using de Haas–van Alphen quantum oscillation measurements on bulk samples.

Separately, optical pumping has previously been shown to stabilize ferroelectricity in $SrTiO_3$ via resonant excitation of phonons with infrared and terahertz light [116, 117]. While coherent excitation of lattice modes has been proven to stabilize ferroelectricity, the effect of optical pumping remains an open question. The ferroelectric phase in strained, doped films of $SrTiO_3$ is shown by our work to depend sensitively on the carrier density of the film. Optical pumping induces large changes in the electronic population, which could result in a short-lived polar phase. A pump-probe SHG measurement would be sensitive to inversion symmetry breaking caused by optical pumping, which could indicate transient ferroelectricity. These measurements could be performed on samples that are on both the under- and over-doped sides of the polar phase transition to explore the effect, if any, of optical pumping.

8.2 Optical studies of Sr_2RuO_4

8.2.1 Raman spectroscopy in thin films of Sr_2RuO_4

While we provide evidence for a nematic phase with our time-resolved optical measurements, several questions remain unanswered: Why do electronic transport measurements resolve nematicity in both orthorhombic (NGO) and tetragonal (LSAT) films? Is the observed checkerboard charge order at the surface of Sr_2RuO_4 truly a surface effect, or does it originate in bulk nematicity? Does the Emery model explain the nematicity seen by other probes?

One promising approach to test for the existence of the nematic phase is to use Raman spectroscopy to probe the nematic fluctuations that should be present in films that approach a nematic instability. By choosing an appropriate experimental geometry with regard to the crystal axes and the polarization of the incoming and outgoing light, excitations can be mapped and separated into their respective symmetry channels using group-theoretical analysis [118]. This approach has been used successfully in a known nematic material, (Co-doped) $BaFe_2As_2$ [119, 120]. There are several nice features of such an experiment: (1) As a spectroscopic probe, the electronic Raman response is insensitive to the acoustic phonons in the system, allowing one to distinguish between lattice-driven and electronically driven nematicity. (2) Nematic fluctuations, if they exist, should be present in the tetragonal film grown on LSAT. Raman spectroscopy is sensitive to these fluctuations, which should increase toward the nematic ordering temperature. Evidence

of nematicity from tetragonal films removes the uncertainty associated with probing nematic order in a uniaxially strained system. (3) The electronic Raman response χ^{μ} is proportional to ϕ^2, rather than ϕ (the nematic order parameter) [120]. As a result, even though ϕ changes sign under a 90° rotation, ϕ^2 is C_4 symmetric and remains finite even if nematic fluctuations render $\langle\phi\rangle = 0$.

A previous study has indeed investigated Sr_2RuO_4 crystals with polarized Raman spectroscopy [121]. It is found that the d_{xy} derived quasiparticles are significantly more correlated than those originating from the d_{xz}/d_{yz} orbitals, and a symmetry-resolved static Raman susceptibility is reported for both the B_{1g} and B_{2g} channels. Although the authors claim that the B_{1g} susceptibility is flat with temperature, close observation suggests an anomaly in this signal around 50-60 K – similar to the nematic ordering temperature extracted by our Ising-model analysis of the optical dichroism. Follow-up studies of the electronic Raman response may clarify the presence of this anomaly, which could signal increasing nematic fluctuations upon approaching the nematic ordering temperature. A comparison of tetragonal films, uniaxially strained films, and bulk samples may be informative.

8.2.2 Strained single-crystal Sr_2RuO_4

Many recent investigations of Sr_2RuO_4 have been performed on strained single crystals mounted in a strain rig which can apply uniaxial pressure [42, 63, 49]. This technique is advantageous in that it allows for the continuous tuning of the strain state of the material,

rather than the discrete, fixed strain state imposed by a chosen substrate. Repeating the optical transient reflectivity measurements reported in Chapter 5 while varying the strain may provide additional information about the onset of nematicity as a function of the symmetry-breaking strain. The Raman spectroscopy experiments described above may also be interesting in strained single crystals, leveraging continuous uniaxial pressure as a tuning knob for the nematicity.

8.3 Further investigation of Ca_2RuO_4 thin films

Several features of the optical pump-probe response of the Ca_2RuO_4 thin films measured in Chapter 7 warrant further investigation. In particular, the qualitative change of the transient reflectivity as a function of pump fluence at low temperature (12 K) is intriguing. The change in line shape during the first several tens of picoseconds is quite dramatic, and an explanation of this phenomenon is lacking. Further, coherent modes appear in the $\Delta R/R$ signal at sufficiently high pump fluence, with a period of approximately 30 ps. The origin of this mode is unknown, as is the reason for its apparent dependence on fluence. Other coherent modes may also be revealed with better frequency resolution in future measurements. The linear pump-fluence dependence of the transient reflectivity at higher temperature also indicates the presence of a long-lived metastable state as seen in the nonzero signal at negative time delay. The pump-fluence dependence of this pre-time-zero signal can be analyzed to reveal details about the long-lived state, as established by previous studies using the optical pump-probe technique [15].

Appendix A

Appendix

A.1 Computing expressions for SHG intensity

We use Mathematica notebooks to carry out the tensor multiplication necessary to produce expressions which correspond to the anticipated signal in each of the 4 polarization channels for a given point group symmetry. To see how this actually carried out in Mathematica, an example is given below for the point group $\bar{4}3m$, which is the point group of GaAs (a sample commonly used to calibrate our setup). First, we write down the general form of the $\chi^{(2)}$ tensor, and then define a new tensor with only the unique nonzero elements which remain after applying the relevant point group symmetries.

```
In[1]:= χ2={{{χxxx,χxxy,χxxz},{χxyx,χxyy,χxyz},{χxzx,χxzy,χxzz}},
         {{χyxx,χyxy,χyxz},{χyyx,χyyy,χyyz},{χyzx,χyzy,χyzz}},{{χzxx,
         χzxy,χzxz},{χzyx,χzyy,χzyz},{χzzx,χzzy,χzzz}}}
         χ24bar3m=χ2/.{χxxx→0,χxxy→0,χxxz→0,χxyx→0,χxyy→0,
         χxyz→χxyz,χxzx→0,χxzy→χxyz,χxzz→0,χyxx→0,χyxy→0,
         χyxz→χxyz,χyyx→0,χyyy→0,χyyz→0,χyzx→χxyz,χyzy→0,χyzz→0,
         χzxx→0,χzxy→χxyz,χzxz→0,χzyx→χxyz,χzyy→0,χzyz→0,χzzx→0,
         χzzy→0,χzzz→0}
```

The tensors in matrix form are generated below:

```
Out[1]= {{{χxxx,χxxy,χxxz},{χxyx,
         χxyy,χxyz},{χxzx,χxzy,χxzz}},
         {{χyxx,χyxy,χyxz},{χyyx,
         χyyy,χyyz},{χyzx,χyzy,χyzz}},
         {{χzxx,χzxy,χzxz},{χzyx,
         χzyy,χzyz},{χzzx,χzzy,χzzz}}}

Out[2]= {{{0,0,0},{0,0,χxyz},{0,χxyz,0}},
         {{0,0,χxyz},{0,0,0},{χxyz,0,0}},
         {{0,χxyz,0},{χxyz,0,0},{0,0,0}}}
```

The tensor product and contraction is then performed:

In[3]:=
```
SS=FullSimplify[TensorContract[TensorProduct[χ24bar3m,{Sin[ϕ],-
Cos[ϕ],0},{Sin[ϕ],-Cos[ϕ],0},{Sin[ϕ],-Cos[ϕ],0}],{{1,4},{2,5},
{3,6}}]^2]
SP=FullSimplify[TensorContract[TensorProduct[χ24bar3m,{Cos[θ]*
Cos[ϕ],Cos[θ]*Sin[ϕ],Sin[θ]},{Sin[ϕ],-Cos[ϕ],0},{Sin[ϕ],-Cos[
ϕ],0}],{{1,4},{2,5},{3,6}}]^2]
PS=FullSimplify[TensorContract[TensorProduct[χ24bar3m,{Sin[ϕ],-
Cos[ϕ],0},{-Cos[θ]*Cos[ϕ],-Cos[θ]*Sin[ϕ],Sin[θ]},{-Cos[θ]*Cos[
ϕ],-Cos[θ]*Sin[ϕ],Sin[θ]}],{{1,4},{2,5},{3,6}}]^2]
PP=FullSimplify[TensorContract[TensorProduct[χ24bar3m,{Cos[θ]*
Cos[ϕ],Cos[θ]*Sin[ϕ],Sin[θ]},{-Cos[θ]*Cos[ϕ],-Cos[θ]*Sin[ϕ],Sin
[θ]},{-Cos[θ]*Cos[ϕ],-Cos[θ]*Sin[ϕ],Sin[θ]}],{{1,4},{2,5},{3,6
}}]^2]
```

This yields functions corresponding to the SHG versus ϕ in each polarization channel:

Out[3]= 0

Out[4]= $\chi xyz^2 Sin[\theta]^2 Sin[2\phi]^2$

Out[5]= $\chi xyz^2 Cos[2\phi]^2 Sin[2\theta]^2$

Out[6]= $4\chi xyz^2 Cos[\theta]^4 Cos[\phi]^2 Sin[\theta]^2 Sin[\phi]^2$

A.2 Measurements of Sr_2RuO_4 on an LSAT substrate

Transient reflectivity measurements were performed on a Sr_2RuO_4 thin film grown on an LSAT substrate, which is tetragonal and induces no uniaxial strain. Figure A.1(a) shows that in the absence of uniaxial strain, the in-plane anisotropy of the transient reflectivity vanishes. Figure A.1(b) compares the transient reflectivity of SRO/LSAT to a particular weighted average of the transient reflectivity of SRO/NGO at the 0° (maximum) and 90° (minimum) orientations. The similarity of the two responses using an approximate 3:1 ratio is curious, suggesting a nontrivial averaging of nematic domains within the SRO/LSAT sample. Without an epitaxial strain field setting a preferred global alignment direction for the domains, it is possible that the polarization direction of the pump and/or probe is preferentially aligning them. Under this scenario, we would not observe rotational anisotropy (because the pump and probe polarization rotate with θ), but we would observe a domain imbalance.

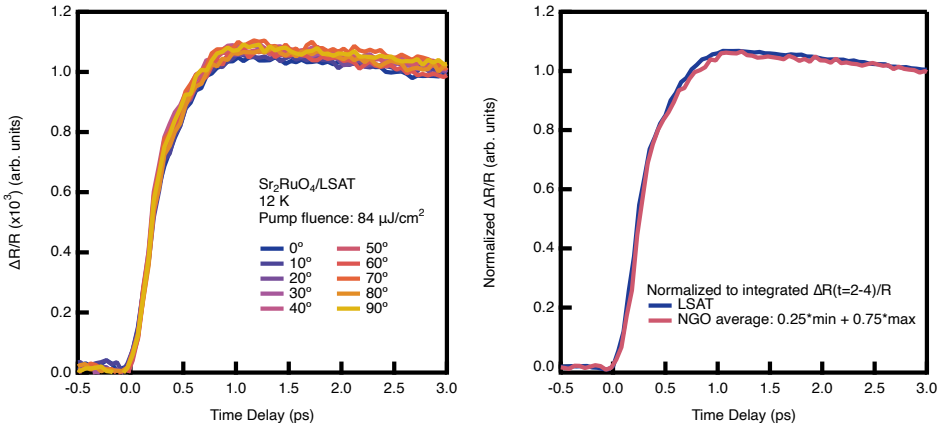

Figure A.1: Transient reflectivity measurements of Sr_2RuO_4 grown on a tetragonal LSAT substrate. (a) Absence of nematic anisotropy in the transient optical response. (b) Comparison of SRO/LSAT data with a weighted average of SRO/NGO data.

Bibliography

[1] B. Keimer and J. E. Moore. The physics of quantum materials. *Nature Physics*, 13(11):1045–1055, November 2017.

[2] Alberto de la Torre, Dante M. Kennes, Martin Claassen, Simon Gerber, James W. McIver, and Michael A. Sentef. Colloquium: Nonthermal pathways to ultrafast control in quantum materials. *Reviews of Modern Physics*, 93(4):041002, October 2021.

[3] D. N. Basov, Richard D. Averitt, Dirk van der Marel, Martin Dressel, and Kristjan Haule. Electrodynamics of correlated electron materials. *Reviews of Modern Physics*, 83(2):471–541, June 2011.

[4] Yoshinori Tokura, Masashi Kawasaki, and Naoto Nagaosa. Emergent functions of quantum materials. *Nature Physics*, 13(11):1056–1068, November 2017.

[5] Liuyan Zhao, Darius Torchinsky, John Harter, Alberto de la Torre, and David Hsieh. Second Harmonic Generation Spectroscopy of Hidden Phases. In *Encyclopedia of Modern Optics*, pages 207–226. Elsevier, 2018.

[6] Robert W. Boyd, Alexander L. Gaeta, and Enno Giese. Nonlinear Optics. In Gordon W. F. Drake, editor, *Springer Handbook of Atomic, Molecular, and Optical Physics*, Springer Handbooks, pages 1097–1110. Springer International Publishing, Cham, 2023.

[7] Margherita Maiuri, Marco Garavelli, and Giulio Cerullo. Ultrafast Spectroscopy: State of the Art and Open Challenges. *Journal of the American Chemical Society*, 142(1):3–15, January 2020.

[8] Tao Dong, Si-Jie Zhang, and Nan-Lin Wang. Recent Development of Ultrafast Optical Characterizations for Quantum Materials. *Advanced Materials*, 35(27):2110068, 2023.

[9] Philip B. Allen. Theory of thermal relaxation of electrons in metals. *Physical Review Letters*, 59(13):1460–1463, September 1987.

[10] Manuel Obergfell and Jure Demsar. Tracking the Time Evolution of the Electron Distribution Function in Copper by Femtosecond Broadband Optical Spectroscopy. *Physical Review Letters*, 124(3):037401, January 2020.

[11] M. Först, C. Manzoni, S. Kaiser, Y. Tomioka, Y. Tokura, R. Merlin, and A. Cavalleri. Nonlinear phononics as an ultrafast route to lattice control. *Nature Physics*, 7(11):854–856, November 2011.

[12] D. M. Riffe and A. J. Sabbah. Coherent excitation of the optic phonon in Si: Transiently stimulated Raman scattering with a finite-lifetime electronic excitation. *Physical Review B*, 76(8):085207, August 2007.

[13] R. Merlin. Generating coherent THz phonons with light pulses. *Solid State Communications*, 102(2):207–220, April 1997.

[14] H. J. Zeiger, J. Vidal, T. K. Cheng, E. P. Ippen, G. Dresselhaus, and M. S. Dresselhaus. Theory for displacive excitation of coherent phonons. *Physical Review B*, 45(2):768–778, January 1992.

[15] Noah Ratcliff, Lily Hallett, Brenden R. Ortiz, Stephen D. Wilson, and John W. Harter. Coherent phonon spectroscopy and interlayer modulation of charge density wave order in the kagome metal CsV_3Sb_5. *Physical Review Materials*, 5(11):L111801, November 2021.

[16] J. W. Harter, D. M. Kennes, H. Chu, A. de la Torre, Z. Y. Zhao, J.-Q. Yan, D. G. Mandrus, A. J. Millis, and D. Hsieh. Evidence of an Improper Displacive Phase Transition in $Cd_2Re_2O_7$ via Time-Resolved Coherent Phonon Spectroscopy. *Physical Review Letters*, 120(4), January 2018.

[17] A. Y. Cho and J. R. Arthur. Molecular beam epitaxy. *Progress in Solid State Chemistry*, 10:157–191, January 1975.

[18] Tsuyoshi Ohnishi, Keisuke Shibuya, Takahisa Yamamoto, and Mikk Lippmaa. Defects and transport in complex oxide thin films. *Journal of Applied Physics*, 103(10):103703, May 2008.

[19] William Nunn, Tristan K. Truttmann, and Bharat Jalan. A review of molecular-beam epitaxy of wide bandgap complex oxide semiconductors. *Journal of Materials Research*, 36(23):4846–4864, December 2021.

[20] Federico Baiutti, Georg Christiani, and Gennady Logvenov. Towards precise defect control in layered oxide structures by using oxide molecular beam epitaxy. *Beilstein Journal of Nanotechnology*, 5:596–602, May 2014.

[21] J.H. Haeni, C.D. Theis, and D.G. Schlom. RHEED Intensity Oscillations for the Stoichiometric Growth of $SrTiO_3$ Thin Films by Reactive Molecular Beam Epitaxy. *Journal of Electroceramics*, 4(2):385–391, June 2000.

[22] Suresh Thapa, Rajendra Paudel, Miles D. Blanchet, Patrick T. Gemperline, and Ryan B. Comes. Probing surfaces and interfaces in complex oxide films via in situ X-ray photoelectron spectroscopy. *Journal of Materials Research*, 36(1):26–51, January 2021.

[23] A. Y. Cho. Film Deposition by Molecular-Beam Techniques. *Journal of Vacuum Science and Technology*, 8(5):S31–S38, September 1971.

[24] Matthew Brahlek, Arnab Sen Gupta, Jason Lapano, Joseph Roth, Hai-Tian Zhang, Lei Zhang, Ryan Haislmaier, and Roman Engel-Herbert. Frontiers in the Growth of Complex Oxide Thin Films: Past, Present, and Future of Hybrid MBE. *Advanced Functional Materials*, 28(9):1702772, 2018.

[25] Bharat Jalan, Roman Engel-Herbert, Nicholas J. Wright, and Susanne Stemmer. Growth of high-quality $SrTiO_3$ films using a hybrid molecular beam epitaxy approach. *Journal of Vacuum Science & Technology A: Vacuum, Surfaces, and Films*, 27(3):461–464, May 2009.

[26] Bharat Jalan, Pouya Moetakef, and Susanne Stemmer. Molecular beam epitaxy of $SrTiO_3$ with a growth window. *Applied Physics Letters*, 95(3):032906, July 2009.

[27] Tyler A. Cain, Adam P. Kajdos, and Susanne Stemmer. La-doped $SrTiO_3$ films with large cryogenic thermoelectric power factors. *Applied Physics Letters*, 102(18):182101, May 2013.

[28] Junwoo Son, Pouya Moetakef, Bharat Jalan, Oliver Bierwagen, Nicholas J. Wright, Roman Engel-Herbert, and Susanne Stemmer. Epitaxial $SrTiO_3$ films with electron mobilities exceeding 30,000 $cm^2\ V^{-1}\ s^{-1}$. *Nature Materials*, 9(6):482–484, June 2010.

[29] Jake S. Bobowski, Naoki Kikugawa, Takuto Miyoshi, Haruki Suwa, Han-shu Xu, Shingo Yonezawa, Dmitry A. Sokolov, Andrew P. Mackenzie, and Yoshiteru Maeno. Improved Single-Crystal Growth of Sr_2RuO_4. *Condensed Matter*, 4(1):6, March 2019.

[30] M. Uchida, M. Ide, H. Watanabe, K. S. Takahashi, Y. Tokura, and M. Kawasaki. Molecular beam epitaxy growth of superconducting Sr_2RuO_4 films. *APL Materials*, 5(10):106108, October 2017.

[31] Hari P. Nair, Jacob P. Ruf, Nathaniel J. Schreiber, Ludi Miao, Morgan L. Grandon, David J. Baek, Berit H. Goodge, Jacob P. C. Ruff, Lena F. Kourkoutis, Kyle M. Shen, and Darrell G. Schlom. Demystifying the growth of superconducting Sr_2RuO_4 thin films. *APL Materials*, 6(10):101108, October 2018.

[32] Shabnam Dadgostar, Jose Luis Pura Ruiz, Jorge Serrano Gutierrez, Bruno Lepine, Philippe Schieffer, and Juan Jimenez. Luminescence in undoped and Nb-doped $SrTiO_3$ crystals: Bulk and surface emission. *Materials Science and Engineering: B*, 283:115830, September 2022.

[33] Junhwi Lim, Hyeontae Lim, and Y.S. Lee. Ambient dependence of visible emissions in $SrTiO_3$. *Current Applied Physics*, 19(11):1177–1181, November 2019.

[34] Zhen Song, Jing Zhao, and Quanlin Liu. Luminescent perovskites: Recent advances in theory and experiments. *Inorganic Chemistry Frontiers*, 6(11):2969–3011, 2019.

[35] V. S. Vikhnin, S. Kapphan, and R. I. Eglitis. Localized Polaronic Exciton and Active Impurity Problems in Incipient and Relaxor Ferroelectrics. *Ferroelectrics*, 299(1):11–20, January 2004.

[36] Q. Huang, J.L. Soubeyroux, O. Chmaissem, I.Natali Sora, A. Santoro, R.J. Cava, J.J. Krajewski, and W.F. Peck. Neutron powder diffraction study of the crystal structures of Sr_2RuO_4 and Sr_2IrO_4 at room temperature and at 10 K. *Journal of Solid State Chemistry*, 112(2):355–361, 1994.

[37] A. Tamai, M. Zingl, E. Rozbicki, E. Cappelli, S. Riccò, A. de la Torre, S. McKeown Walker, F. Y. Bruno, P. D. C. King, W. Meevasana, M. Shi, M. Radović, N. C. Plumb, A. S. Gibbs, A. P. Mackenzie, C. Berthod, H. U. R. Strand, M. Kim, A. Georges, and F. Baumberger. High-Resolution Photoemission on Sr_2RuO_4 Reveals Correlation-Enhanced Effective Spin-Orbit Coupling and Dominantly Local Self-Energies. *Physical Review X*, 9(2):021048, June 2019.

[38] A. P. Mackenzie, N. E. Hussey, A. J. Diver, S. R. Julian, Y. Maeno, S. Nishizaki, and T. Fujita. Hall effect in the two-dimensional metal Sr_2RuO_4. *Physical Review B*, 54(10):7425–7429, September 1996.

[39] Naoki Shirakawa, Keizo Murata, Yoshikazu Nishihara, Shuji Nishizaki, Yoshiteru Maeno, Toshizo Fujita, J. Georg Bednorz, Frank Lichtenberg, and Noriaki Hamada. Novel Hall-Coefficient Behavior inSuperconducting Sr_2RuO_4. *Journal of the Physical Society of Japan*, 64(4):1072–1075, April 1995.

[40] Manuel Zingl, Jernej Mravlje, Markus Aichhorn, Olivier Parcollet, and Antoine Georges. Hall coefficient signals orbital differentiation in the Hund's metal Sr_2RuO_4. *npj Quantum Materials*, 4(1):1–6, July 2019.

[41] D. Stricker, J. Mravlje, C. Berthod, R. Fittipaldi, A. Vecchione, A. Georges, and D. van der Marel. Optical Response of Sr_2RuO_4 Reveals Universal Fermi-Liquid Scaling and Quasiparticles Beyond Landau Theory. *Physical Review Letters*, 113(8):087404, August 2014.

[42] A. Chronister, M. Zingl, A. Pustogow, Yongkang Luo, D. A. Sokolov, F. Jerzembeck, N. Kikugawa, C. W. Hicks, J. Mravlje, E. D. Bauer, J. D. Thompson, A. P. Mackenzie, A. Georges, and S. E. Brown. Tuning the Fermi liquid crossover in Sr_2RuO_4 with uniaxial stress. *npj Quantum Materials*, 7(1):1–6, December 2022.

[43] T. Imai, A. W. Hunt, K. R. Thurber, and F. C. Chou. ^{17}O NMR Evidence for Orbital Dependent Ferromagnetic Correlations in Sr_2RuO_4. *Physical Review Letters*, 81(14):3006–3009, October 1998.

[44] Yoshiteru Maeno, Koji Yoshida, Hiroaki Hashimoto, Shuji Nishizaki, Shin-ichi Ikeda, Minoru Nohara, Toshizo Fujita, Andrew P. Mackenzie, Nigel E. Hussey, J. Georg Bednorz, and Frank Lichtenberg. Two-Dimensional Fermi Liquid Behavior of the Superconductor Sr_2RuO_4. *Journal of the Physical Society of Japan*, 66(5):1405–1408, May 1997.

[45] C. Bergemann, A. P. Mackenzie, S. R. Julian, D. Forsythe, and E. Ohmichi. Quasi-two-dimensional Fermi liquid properties of the unconventional superconductor Sr $_2$ RuO $_4$. *Advances in Physics*, 52(7):639–725, November 2003.

[46] B. Burganov, C. Adamo, A. Mulder, M. Uchida, P. D. C. King, J. W. Harter, D. E. Shai, A. S. Gibbs, A. P. Mackenzie, R. Uecker, M. Bruetzam, M. R. Beasley, C. J. Fennie, D. G. Schlom, and K. M. Shen. Strain Control of Fermiology and Many-Body Interactions in Two-Dimensional Ruthenates. *Physical Review Letters*, 116(19):197003, May 2016.

[47] Alexander Steppke, Lishan Zhao, Mark E. Barber, Thomas Scaffidi, Fabian Jerzembeck, Helge Rosner, Alexandra S. Gibbs, Yoshiteru Maeno, Steven H. Simon, Andrew P. Mackenzie, and Clifford W. Hicks. Strong peak in T_c of Sr_2RuO_4 under uniaxial pressure. *Science*, 355(6321):eaaf9398, January 2017.

[48] Vadim Grinenko, Shreenanda Ghosh, Rajib Sarkar, Jean-Christophe Orain, Artem Nikitin, Matthias Elender, Debarchan Das, Zurab Guguchia, Felix Brückner, Mark E. Barber, Joonbum Park, Naoki Kikugawa, Dmitry A. Sokolov, Jake S. Bobowski, Takuto Miyoshi, Yoshiteru Maeno, Andrew P. Mackenzie, Hubertus Luetkens, Clifford W. Hicks, and Hans-Henning Klauss. Split superconducting and time-reversal symmetry-breaking transitions in Sr_2RuO_4 under stress. *Nature Physics*, March 2021.

[49] You-Sheng Li, Naoki Kikugawa, Dmitry A. Sokolov, Fabian Jerzembeck, Alexandra S. Gibbs, Yoshiteru Maeno, Clifford W. Hicks, Jörg Schmalian, Michael Nicklas, and Andrew P. Mackenzie. High-sensitivity heat-capacity measurements on Sr_2RuO_4 under uniaxial pressure. *Proceedings of the National Academy of Sciences*, 118(10):e2020492118, March 2021.

[50] You-Sheng Li, Markus Garst, Jörg Schmalian, Sayak Ghosh, Naoki Kikugawa, Dmitry A. Sokolov, Clifford W. Hicks, Fabian Jerzembeck, Matthias S. Ikeda, Zhenhai Hu, B. J. Ramshaw, Andreas W. Rost, Michael Nicklas, and Andrew P. Mackenzie. Elastocaloric determination of the phase diagram of Sr_2RuO_4. *Nature*, 607(7918):276–280, July 2022.

[51] Veronika Sunko, Edgar Abarca Morales, Igor Marković, Mark E. Barber, Dijana Milosavljević, Federico Mazzola, Dmitry A. Sokolov, Naoki Kikugawa, Cephise Cacho, Pavel Dudin, Helge Rosner, Clifford W. Hicks, Philip D. C. King, and Andrew P. Mackenzie. Direct observation of a uniaxial stress-driven Lifshitz transition in Sr_2RuO_4. *npj Quantum Materials*, 4(1):46, December 2019.

[52] Jie Wu, Hari P. Nair, Anthony T. Bollinger, Xi He, Ian Robinson, Nathaniel J. Schreiber, Kyle M. Shen, Darrell G. Schlom, and Ivan Božović. Electronic nematicity in Sr_2RuO_4. *Proceedings of the National Academy of Sciences*, 117(20):10654–10659, May 2020.

[53] Carolina A. Marques, Luke C. Rhodes, Rosalba Fittipaldi, Veronica Granata, Chi Ming Yim, Renato Buzio, Andrea Gerbi, Antonio Vecchione, Andreas W. Rost, and Peter Wahl. Magnetic-Field Tunable Intertwined Checkerboard Charge Order and Nematicity in the Surface Layer of Sr2RuO4. *Advanced Materials*, 33(32):2100593, 2021.

[54] Eduardo Fradkin. Electronic Liquid Crystal Phases in Strongly Correlated Systems. In Daniel C. Cabra, Andreas Honecker, and Pierre Pujol, editors, *Modern Theories of Many-Particle Systems in Condensed Matter Physics*, Lecture Notes in Physics, pages 53–116. Springer, Berlin, Heidelberg, 2012.

[55] M. Chinotti, A. Pal, L. Degiorgi, A. E. Böhmer, and P. C. Canfield. Optical anisotropy in the electronic nematic phase of FeSe. *Physical Review B*, 96(12):121112, September 2017.

[56] Jiun-Haw Chu, James G. Analytis, Kristiaan De Greve, Peter L. McMahon, Zahirul Islam, Yoshihisa Yamamoto, and Ian R. Fisher. In-Plane Resistivity Anisotropy in an Underdoped Iron Arsenide Superconductor. *Science*, 329(5993):824–826, August 2010.

[57] A. Dusza, A. Lucarelli, F. Pfuner, J.-H. Chu, I. R. Fisher, and L. Degiorgi. Anisotropic charge dynamics in detwinned $Ba(Fe_{1-x}Co_x)_2As_2$. *Europhysics Letters*, 93(3):37002, February 2011.

[58] M. A. Tanatar, E. C. Blomberg, A. Kreyssig, M. G. Kim, N. Ni, A. Thaler, S. L. Bud'ko, P. C. Canfield, A. I. Goldman, I. I. Mazin, and R. Prozorov. Uniaxial-strain mechanical detwinning of $CaFe_2As_2$ and $BaFe_2As_2$ crystals: Optical and transport study. *Physical Review B*, 81(18):184508, May 2010.

[59] Ming Yi, Donghui Lu, Jiun-Haw Chu, James G. Analytis, Adam P. Sorini, Alexander F. Kemper, Brian Moritz, Sung-Kwan Mo, Rob G. Moore, Makoto Hashimoto, Wei-Sheng Lee, Zahid Hussain, Thomas P. Devereaux, Ian R. Fisher, and Zhi-Xun Shen. Symmetry-breaking orbital anisotropy observed for detwinned $Ba(Fe_{1-x}Co_x)_2As_2$ above the spin density wave transition. *Proceedings of the National Academy of Sciences*, 108(17):6878–6883, April 2011.

[60] Ryan S. Russell, Hari P. Nair, Kyle M. Shen, Darrell G. Schlom, and John W. Harter. Electronic nematic order in the normal state of strontium ruthenate. *Physical Review B*, 108(8):L081105, August 2023.

[61] D. Savytskii, L. Vasylechko, A. Senyshyn, A. Matkovskii, C. Bähtz, M. L. Sanjuán, U. Bismayer, and M. Berkowski. Low-temperature structural and Raman studies on rare-earth gallates. *Physical Review B*, 68(2):024101, July 2003.

[62] Mark E. Barber, Frank Lechermann, Sergey V. Streltsov, Sergey L. Skornyakov, Sayak Ghosh, B. J. Ramshaw, Naoki Kikugawa, Dmitry A. Sokolov, Andrew P. Mackenzie, Clifford W. Hicks, and I. I. Mazin. Role of correlations in determining the Van Hove strain in Sr_2RuO_4. *Physical Review B*, 100(24):245139, December 2019.

[63] Clifford W. Hicks, Daniel O. Brodsky, Edward A. Yelland, Alexandra S. Gibbs, Jan A. N. Bruin, Mark E. Barber, Stephen D. Edkins, Keigo Nishimura, Shingo Yonezawa, Yoshiteru Maeno, and Andrew P. Mackenzie. Strong Increase of T_c of Sr_2RuO_4 Under Both Tensile and Compressive Strain. *Science*, 344(6181):283–285, April 2014.

[64] O. Chmaissem, J. D. Jorgensen, H. Shaked, S. Ikeda, and Y. Maeno. Thermal expansion and compressibility of Sr_2RuO_4. *Physical Review B*, 57(9):5067–5070, March 1998.

[65] T. Vogt and D. J. Buttrey. Low-temperature structural behavior of Sr_2RuO_4. *Physical Review B*, 52(14):R9843–R9846, October 1995.

[66] M. Steins, J. Doerschel, and P. Reiche. Crystal structure of aluminium lanthanum strontium tantalum oxide, $(La_{0.272}Sr_{0.728})(Al_{0.648}Ta_{0.352})O_3$. *Zeitschrift für Kristallographie - New Crystal Structures*, 212(1):77–77, December 1997.

[67] Min-Cheol Lee, Inho Kwak, Yeongseon Lee, Bumjoo Lee, Byung Cheol Park, Thomas Wolf, Tae Won Noh, and Kyungwan Kim. Nematic response revealed by coherent phonon oscillations in $BaFe_2As_2$. *Physical Review B*, 105(2):024501, January 2022.

[68] Shenghua Liu, Chunfeng Zhang, Qiang Deng, Hai-hu Wen, Jian-xin Li, Elbert E. M. Chia, Xiaoyong Wang, and Min Xiao. Transient electronic anisotropy in overdoped $NaFe_{1-x}Co_xAs$. *Physical Review B*, 97(2):020505, January 2018.

[69] Chih-Wei Luo, Po Chung Cheng, Shun-Hung Wang, Jen-Che Chiang, Jiunn-Yuan Lin, Kaung-Hsiung Wu, Jenh-Yih Juang, Dmitry A. Chareev, Olga S. Volkova, and Alexander N. Vasiliev. Unveiling the hidden nematicity and spin subsystem in FeSe. *npj Quantum Materials*, 2(1):1–6, June 2017.

[70] L. Stojchevska, T. Mertelj, Jiun-Haw Chu, Ian R. Fisher, and D. Mihailovic. Doping dependence of femtosecond quasiparticle relaxation dynamics in $Ba(Fe,Co)_2As_2$ single crystals: Evidence for normal-state nematic fluctuations. *Physical Review B*, 86(2):024519, July 2012.

[71] Eric Thewalt, Ian M. Hayes, James P. Hinton, Arielle Little, Shreyas Patankar, Liang Wu, Toni Helm, Camelia V. Stan, Nobumichi Tamura, James G. Analytis, and Joseph Orenstein. Imaging Anomalous Nematic Order and Strain in Optimally Doped $BaFe_2(As,P)_2$. *Physical Review Letters*, 121(2):027001, July 2018.

[72] Andrew P. Mackenzie, Shin-ichi Ikeda, Yoshiteru Maeno, Toshizo Fujita, Stephen R. Julian, and Gilbert G. Lonzarich. The Fermi Surface Topography of Sr_2RuO_4. *Journal of the Physical Society of Japan*, 67(2):385–388, February 1998.

[73] V. J. Emery. Theory of high-T_c superconductivity in oxides. *Physical Review Letters*, 58(26):2794–2797, June 1987.

[74] K. M. Shen, N. Kikugawa, C. Bergemann, L. Balicas, F. Baumberger, W. Meevasana, N. J. C. Ingle, Y. Maeno, Z.-X. Shen, and A. P. Mackenzie. Evolution of the Fermi Surface and Quasiparticle Renormalization through a van Hove Singularity in $Sr_{2-y}La_yRuO_4$. *Physical Review Letters*, 99(18):187001, October 2007.

[75] Mark H. Fischer and Eun-Ah Kim. Mean-field analysis of intra-unit-cell order in the Emery model of the CuO_2 plane. *Physical Review B*, 84(14):144502, October 2011.

[76] Krzysztof Rościszewski and Andrzej M. Oleś. Charge-transfer model for the electronic structure of layered ruthenates. *Physical Review B*, 91(15):155137, April 2015.

[77] David J. Singh. Relationship of Sr_2RuO_4 to the superconducting layered cuprates. *Physical Review B*, 52(2):1358–1361, July 1995.

[78] V. S. de Carvalho and R. M. Fernandes. Resistivity near a nematic quantum critical point: Impact of acoustic phonons. *Physical Review B*, 100(11):115103, September 2019.

[79] Lucas E. Vieira, Vanuildo S. de Carvalho, and Hermann Freire. DC resistivity near a nematic quantum critical point: Effects of weak disorder and acoustic phonons. *Annals of Physics*, 419:168230, August 2020.

[80] Xiaoyu Wang and Erez Berg. Scattering mechanisms and electrical transport near an Ising nematic quantum critical point. *Physical Review B*, 99(23):235136, June 2019.

[81] Clément Collignon, Xiao Lin, Carl Willem Rischau, Benoît Fauqué, and Kamran Behnia. Metallicity and Superconductivity in Doped Strontium Titanate. *Annual Review of Condensed Matter Physics*, 10(1):25–44, 2019.

[82] Yasutami Takada. Theory of Superconductivity in Polar Semiconductors and Its Application to N-Type Semiconducting $SrTiO_3$. *Journal of the Physical Society of Japan*, 49(4):1267–1275, October 1980.

[83] K. Dunnett, Awadhesh Narayan, N. A. Spaldin, and A. V. Balatsky. Strain and ferroelectric soft-mode induced superconductivity in strontium titanate. *Physical Review B*, 97(14):144506, April 2018.

[84] Jonathan M. Edge, Yaron Kedem, Ulrich Aschauer, Nicola A. Spaldin, and Alexander V. Balatsky. Quantum Critical Origin of the Superconducting Dome in $SrTiO_3$. *Physical Review Letters*, 115(24):247002, December 2015.

[85] S. E. Rowley, C. Enderlein, J. Ferreira de Oliveira, D. A. Tompsett, E. Baggio Saitovitch, S. S. Saxena, and G. G. Lonzarich. Superconductivity in the vicinity of a ferroelectric quantum phase transition, February 2018.

[86] P. W. Anderson and E. I. Blount. Symmetry Considerations on Martensitic Transformations: "Ferroelectric" Metals? *Physical Review Letters*, 14(7):217–219, February 1965.

[87] Shiming Lei, Mingqiang Gu, Danilo Puggioni, Greg Stone, Jin Peng, Jianjian Ge, Yu Wang, Baoming Wang, Yakun Yuan, Ke Wang, Zhiqiang Mao, James M. Rondinelli, and Venkatraman Gopalan. Observation of Quasi-Two-Dimensional Polar Domains and Ferroelastic Switching in a Metal, $Ca_3Ru_2O_7$. *Nano Letters*, 18(5):3088–3095, May 2018.

[88] Youguo Shi, Yanfeng Guo, Xia Wang, Andrew J. Princep, Dmitry Khalyavin, Pascal Manuel, Yuichi Michiue, Akira Sato, Kenji Tsuda, Shan Yu, Masao Arai, Yuichi Shirako, Masaki Akaogi, Nanlin Wang, Kazunari Yamaura, and Andrew T. Boothroyd. A ferroelectric-like structural transition in a metal. *Nature Materials*, 12(11):1024–1027, November 2013.

[89] A. Stucky, G. W. Scheerer, Z. Ren, D. Jaccard, J.-M. Poumirol, C. Barreteau, E. Giannini, and D. van der Marel. Isotope effect in superconducting n-doped $SrTiO_3$. *Scientific Reports*, 6(1):37582, November 2016.

[90] Carl Willem Rischau, Xiao Lin, Christoph P. Grams, Dennis Finck, Steffen Harms, Johannes Engelmayer, Thomas Lorenz, Yann Gallais, Benoît Fauqué, Joachim

Hemberger, and Kamran Behnia. A ferroelectric quantum phase transition inside the superconducting dome of $Sr_{1-x}Ca_xTiO_{3-\delta}$. *Nature Physics*, 13(7):643–648, July 2017.

[91] J. H. Haeni, P. Irvin, W. Chang, R. Uecker, P. Reiche, Y. L. Li, S. Choudhury, W. Tian, M. E. Hawley, B. Craigo, A. K. Tagantsev, X. Q. Pan, S. K. Streiffer, L. Q. Chen, S. W. Kirchoefer, J. Levy, and D. G. Schlom. Room-temperature ferroelectricity in strained $SrTiO_3$. *Nature*, 430(7001):758–761, August 2004.

[92] R. C. Haislmaier, R. Engel-Herbert, and V. Gopalan. Stoichiometry as key to ferroelectricity in compressively strained $SrTiO_3$ films. *Applied Physics Letters*, 109(3):032901, July 2016.

[93] N. A. Pertsev, A. K. Tagantsev, and N. Setter. Phase transitions and strain-induced ferroelectricity in $SrTiO_3$ epitaxial thin films. *Physical Review B*, 61(2):R825–R829, January 2000.

[94] Amit Verma, Santosh Raghavan, Susanne Stemmer, and Debdeep Jena. Ferroelectric transition in compressively strained $SrTiO_3$ thin films. *Applied Physics Letters*, 107(19):192908, November 2015.

[95] Kaveh Ahadi, Luca Galletti, Yuntian Li, Salva Salmani-Rezaie, Wangzhou Wu, and Susanne Stemmer. Enhancing superconductivity in $SrTiO_3$ films with strain. *Science Advances*, 5(4):eaaw0120, April 2019.

[96] Ryan Russell, Noah Ratcliff, Kaveh Ahadi, Lianyang Dong, Susanne Stemmer, and John W. Harter. Ferroelectric enhancement of superconductivity in compressively strained $SrTiO_3$ films. *Physical Review Materials*, 3(9), September 2019.

[97] J. W. Harter, L. Niu, A. J. Woss, and D. Hsieh. High-speed measurement of rotational anisotropy nonlinear optical harmonic generation using position-sensitive detection. *Optics Letters*, 40(20):4671–4674, October 2015.

[98] J. W. Harter, Z. Y. Zhao, J.-Q. Yan, D. G. Mandrus, and D. Hsieh. A parity-breaking electronic nematic phase transition in the spin-orbit coupled metal $Cd_2Re_2O_7$. *Science*, 356(6335):295–299, April 2017.

[99] Salva Salmani-Rezaie, Luca Galletti, Timo Schumann, Ryan Russell, Hanbyeol Jeong, Yuntian Li, John W. Harter, and Susanne Stemmer. Superconductivity in magnetically doped $SrTiO_3$. *Applied Physics Letters*, 118(20):202602, May 2021.

[100] Salva Salmani-Rezaie, Kaveh Ahadi, William M. Strickland, and Susanne Stemmer. Order-Disorder Ferroelectric Transition of Strained $SrTiO_3$. *Physical Review Letters*, 125(8):087601, August 2020.

[101] Salva Salmani-Rezaie, Kaveh Ahadi, and Susanne Stemmer. Polar Nanodomains in a Ferroelectric Superconductor. *Nano Letters*, 20(9):6542–6547, September 2020.

[102] Salva Salmani-Rezaie, Hanbyeol Jeong, Ryan Russell, John W. Harter, and Susanne Stemmer. Role of locally polar regions in the superconductivity of $SrTiO_3$. *Physical Review Materials*, 5(10):104801, October 2021.

[103] Tianqi Wang, Koustav Ganguly, Patrick Marshall, Peng Xu, and Bharat Jalan. Critical thickness and strain relaxation in molecular beam epitaxy-grown $SrTiO_3$ films. *Applied Physics Letters*, 103(21):212904, November 2013.

[104] Dillon D. Fong, G. Brian Stephenson, Stephen K. Streiffer, Jeffrey A. Eastman, Orlando Auciello, Paul H. Fuoss, and Carol Thompson. Ferroelectricity in Ultrathin Perovskite Films. *Science*, 304(5677):1650–1653, June 2004.

[105] Javier Junquera and Philippe Ghosez. Critical thickness for ferroelectricity in perovskite ultrathin films. *Nature*, 422(6931):506–509, April 2003.

[106] D. B. Haviland, Y. Liu, and A. M. Goldman. Onset of superconductivity in the two-dimensional limit. *Physical Review Letters*, 62(18):2180–2183, May 1989.

[107] Hanbyeol Jeong, Ryan Russell, Nicholas G. Combs, Tyler N. Pardue, John W. Harter, and Susanne Stemmer. Similarity in the critical thicknesses for superconductivity and ferroelectricity in strained $SrTiO_3$ films. *Applied Physics Letters*, 121(1):012601, July 2022.

[108] R. C. Haislmaier, R. Engel-Herbert, and V. Gopalan. Stoichiometry as key to ferroelectricity in compressively strained $SrTiO_3$ films. *Applied Physics Letters*, 109(3):032901, July 2016.

[109] N. Reyren, S. Thiel, A. D. Caviglia, L. Fitting Kourkoutis, G. Hammerl, C. Richter, C. W. Schneider, T. Kopp, A.-S. Rüetschi, D. Jaccard, M. Gabay, D. A. Muller, J.-M. Triscone, and J. Mannhart. Superconducting Interfaces Between Insulating Oxides. *Science*, 317(5842):1196–1199, August 2007.

[110] Nicholas G. Combs, Hanbyeol Jeong, Ryan Russell, Linus Kautzsch, Tyler N. Pardue, Thomas E. Mates, Stephen D. Wilson, John W. Harter, and Susanne Stemmer. Ferroelectricity and superconductivity in strained Eu_xSr_{1-x} TiO_3 films. *Physical Review B*, 107(9):094504, March 2023.

[111] Anita Verma, Denis Golež, Oleg Yu Gorobtsov, Kelson Kaj, Ryan Russell, Jeffrey Z. Kaaret, Erik Lamb, Guru Khalsa, Hari P. Nair, Yifei Sun, Ryan Bouck, Nathaniel Schreiber, Jacob P. Ruf, Varun Ramaprasad, Yuya Kubota, Tadashi Togashi, Vladimir A. Stoica, Hari Padmanabhan, John W. Freeland, Nicole A. Benedek, Oleg Shpyrko, John W. Harter, Richard D. Averitt, Darrell G. Schlom, Kyle M. Shen, Andrew J. Millis, and Andrej Singer. Picosecond volume expansion drives a later-time insulator-metal transition in a nano-textured Mott Insulator, April 2023.

[112] Min-Cheol Lee, Choong H. Kim, Inho Kwak, J. Kim, S. Yoon, Byung Cheol Park, Bumjoo Lee, F. Nakamura, C. Sow, Y. Maeno, T. W. Noh, and K. W. Kim. Abnormal phase flip in the coherent phonon oscillations of Ca_2RuO_4. *Physical Review B*, 98(16):161115, October 2018.

[113] Hao Chu. Nonlinear and Ultrafast Optical Investigations of Correlated Materials. *Doctoral Thesis*, 2017.

[114] Hyeok Yoon, Adrian G. Swartz, Shannon P. Harvey, Hisashi Inoue, Yasuyuki Hikita, Yue Yu, Suk Bum Chung, Srinivas Raghu, and Harold Y. Hwang. Low-density superconductivity in $SrTiO_3$ bounded by the adiabatic criterion, June 2021.

[115] Yue Yu, Harold Y. Hwang, S. Raghu, and Suk Bum Chung. Theory of superconductivity in doped quantum paraelectrics. *npj Quantum Materials*, 7(1):1–6, June 2022.

[116] Xian Li, Tian Qiu, Jiahao Zhang, Edoardo Baldini, Jian Lu, Andrew M. Rappe, and Keith A. Nelson. Terahertz field–induced ferroelectricity in quantum paraelectric $SrTiO_3$. *Science*, 364(6445):1079–1082, June 2019.

[117] T. F. Nova, A. S. Disa, M. Fechner, and A. Cavalleri. Metastable ferroelectricity in optically strained $SrTiO_3$. *Science*, 364(6445):1075–1079, June 2019.

[118] Thomas P. Devereaux and Rudi Hackl. Inelastic light scattering from correlated electrons. *Reviews of Modern Physics*, 79(1):175–233, January 2007.

[119] Yann Gallais and Indranil Paul. Charge nematicity and electronic Raman scattering in iron-based superconductors. *Comptes Rendus Physique*, 17(1):113–139, January 2016.

[120] Y. Gallais, R. M. Fernandes, I. Paul, L. Chauvière, Y.-X. Yang, M.-A. Méasson, M. Cazayous, A. Sacuto, D. Colson, and A. Forget. Observation of Incipient Charge Nematicity in $Ba(Fe_{1-x}Co_x)_2As_2$. *Physical Review Letters*, 111(26):267001, December 2013.

[121] Jean-Côme Philippe, Benoît Baptiste, Chanchal Sow, Yoshiteru Maeno, Anne Forget, Dorothée Colson, Maximilien Cazayous, Alain Sacuto, and Yann Gallais. Orbital dichotomy of Fermi liquid properties in Sr_2RuO_4 revealed by Raman spectroscopy. *Physical Review B*, 103(23):235147, June 2021.